



**Spatially Resolved Temperature Determination
in I₂ Gas Using Doppler-Limited Saturation
Spectroscopy**

THESIS

James W. Myers, Jr., Captain, USAF

AFIT/GAP/ENP/00M-03

**DEPARTMENT OF THE AIR FORCE
AIR UNIVERSITY
*AIR FORCE INSTITUTE OF
TECHNOLOGY***

Wright-Patterson Air Force Base, Ohio

20001113 018

APPROVED FOR PUBLIC RELEASE; DISTRIBUTION UNLIMITED.

BTIO QUALITY INSPECTED 4

AFIT/GAP/ENP/00M-03

SPATIALLY RESOLVED TEMPERATURE DETERMINATION IN I_2 GAS USING DOPPLER-
LIMITED SATURATION SPECTROSCOPY

THESIS

Presented to the Faculty

Department of Systems and Engineering Management

Graduate School of Engineering and Management

Air Force Institute of Technology

Air University

Air Education and Training Command

In Partial Fulfillment of the Requirements for the
Degree of Master of Science in Engineering and Environmental Management

James W. Myers, Jr., B.S.

Captain, USAF

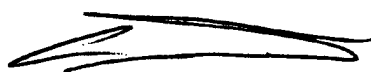
March 2000

APPROVED FOR PUBLIC RELEASE; DISTRIBUTION UNLIMITED.

SPATIALLY RESOLVED TEMPERATURE DETERMINATION IN I₂
GAS USING DOPPLER-LIMITED SATURATION SPECTROSCOPY

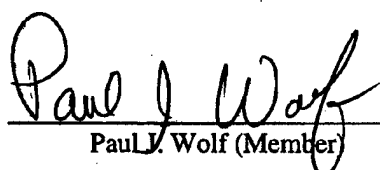
James W. Myers, Jr., B.S.
Captain USAF

Approved:



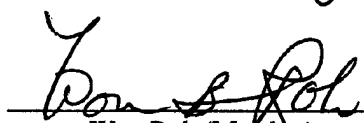
Glen P. Perram (Chairman)

3 MAR 00
date



Paul J. Wolf (Member)

3 MAR 00
date



Won Roh (Member)

3 MAR 00
date

Acknowledgements

Assuming that this thesis is complete before the given deadline, I find it necessary to thank the individuals who have been so instrumental in guaranteeing my success. At times I have asked them to carry heavy burdens, which they--for the most part--accepted graciously. First and foremost, I greatly appreciate the calm guidance of my advisor, Lt. Col. Glen Perram, who gave me the freedom to conduct the project according to my design and at my own pace. His patience, his instruction, and his understanding have been instrumental in pushing me in the right direction.

My thanks also go to Doctor Won Roh, who originated the idea of modifying saturation spectroscopy technique to measure the localized temperature in a gas. His patience in listening to the same questions four or five times, and his willingness to start our mini-lectures from basic principles helped me to obtain the technical confidence to press on. This is quite a feat, all things considered. I would not admit it to my peers, but there is a special place in my heart for Lt. Col. Paul Wolf. He taught me the basics of molecular spectroscopy and was available for many silly questions, most of which were used to develop a good attack strategy for him to use at my thesis defense.

Jeremy Holtgrave, I could not have done this without you. You taught me your hard-won knowledge about how to operate the Ring Dye Laser, and how to curse properly at it when it chose to defy all the known laws of physics. Thanks to Mr. Greg Smith, who is a good electrician, a decent plumber, a talented O-scope negotiator, a fantastic environmental engineer, and an okay conversationalist. Also, I appreciate the efforts of Ms. Belinda Johnson, who did not panic when I spilled laser dye on the wall.

Special thanks are reserved for the guys who got me through my first few quarters: Dean Cherer, Mike Scott, Ariel Acebal, Kelly Doser. I never really learned anything at our study sessions, but I had a great time questioning everything you said and beating the pants off of you in Walleyball.

Mom and Dad, thank you for always pushing me, and especially for the love and support I can always count on. To God, I thank you for not deserting me when I fell, and for leaving me with nothing more to wish for in this life. And the best is reserved for my wife and child, who are my life. Tanya, you have endured many lonely nights and books hurled at walls at two in the morning. Thank you for laughing at me instead of yelling. I am amazed every day at the providence of God, since he let an odd, insane Texan meet a balanced, refined Connecticut Yankee. And now we are three. To you, Thomas, thank you for letting me be your dad, thank you for changing my life, and thank you for stopping my heart when I first saw you.

-“Buster” Myers

Table of Contents

	Page
Acknowledgements _____	iv
Table of Contents _____	vi
List of Figures _____	vii
List of Tables _____	x
Abstract _____	xi
I. Introduction _____	1
A. Background/History _____	1
B. Objective _____	8
C. Presentation _____	9
II. Theory _____	10
A. Electronic Transitions in I_2 _____	10
B. Hyperfine Structure in I_2 _____	18
C. Doppler Broadened Transitions _____	24
D. Doppler-Free Saturation Spectroscopy _____	32
E. Doppler-Limited Saturation Spectroscopy _____	35
III. Experimental _____	37
A. General Setup _____	37
B. Phase I _____	38
C. Phase II _____	44
D. Data Analysis Procedure _____	50
IV. Results _____	54
A. Phase I _____	54
B. Phase II _____	72
V. Discussion and Recommendations _____	81
VI. References _____	85
APPENDIX A _____	88
APPENDIX B _____	92
APPENDIX C _____	96
VITA _____	106

List of Figures

Figure 1. Energy level comparison for I, O ₂ , and I ₂	4
Figure 2. COIL nozzles and optical cavity	5
Figure 3. P(70) 17-1 absorption line with component hyperfine structure	7
Figure 4. Iodine absorption spectrum	10
Figure 5. Typical diatomic energy level structure	12
Figure 6. Branch structure in electronic transitions.	14
Figure 7. Energy level structure for the first few electronic levels in I ₂	17
Figure 8. Hyperfine transitions in I ₂	21
Figure 9. Hyperfine splittings from the electric quadrupole interaction in I ₂	23
Figure 10. Single transition profiles vs. temperature	24
Figure 11. Velocity distributions for N1(v), N2(v)	27
Figure 12. Doppler profile as a superposition	27
Figure 13. Interactions for three incident frequency cases	29
Figure 14 a. The Bennett hole caused by counterpropagation	30
Figure 14b. The Lamb dip in the intensity profile	31
Figure 15. Typical 0-Doppler hole burning spectroscopy setup	32
Figure 16. Absorption holes for 0 Doppler saturation spectroscopy	33
Figure 17. Probe and pump beam modulations	34
Figure 18. Setup diagram for Doppler-limited hole burning spectroscopy	36
Figure 19. Experimental setup for Doppler-free measurements using the enclosed cell	39
Figure 20. Broadened lineshapes for chosen line sets	41
Figure 21. Experimental setup for Doppler-limited measurements using the enclosed cell	43
Figure 22. Cell crossing lengths (shaded region is heater tape)	44
Figure 23. The open cell design	45
Figure 24. Reference temperature measurement setup	46
Figure 25. Doppler-free configuration for open cell	48
Figure 26. Doppler-limited configuration for open cell	49
Figure 27. Hyperfine spectrum for P(70) 17-1	55

Figure 28. Hyperfine spectrum for P(53) 19-2	56
Figure 29. Hyperfine spectrum for P(122) 16-0, R(74) 17-1, R(57) 19-2	57
Figure 30. Hyperfine spectrum for P(66) 16-1, P(51) 18-2	58
Figure 31. Absorption profile for P(70)17-1 for I ₂ at 3 temperatures	60
Figure 32. Absorption profile for P(53)19-2 for I ₂ at 3 temperatures	61
Figure 33. Absorption profile for P(122) 16-0, R(74) 17-1, R(57) 19-2 for I ₂ at 3 temperatures	62
Figure 34. Absorption profile for P(66) 16-1, P(51) 18-2 for I ₂ at 3 Separate temperatures	63
Figure 35. Hyperfine fit plot for P(70) 17-1	65
Figure 36. P(70) 17-1 Doppler-broadened transition at the cold end	67
Figure 37. P(70) 17-1 Doppler-broadened transition at the warm center	67
Figure 38. P(70) 17-1 Doppler-broadened transition at the hot end	68
Figure 39. Hyperfine fit plot for P(70) 17-1	69
Figure 40. Spatial temperature profile for the cell	72
Figure 41. P(70) 17-1 hyperfine structure	73
Figure 42. P(53) 19-2 hyperfine structure	74
Figure 43. Phase II hyperfine fit plot for P(70) 17-1	75
Figure 44. Temperature comparison for P(70)17-1 transition	76
Figure 45. Phase II hyperfine fit plot for P(53) 19-2	78
Figure 44. Temperature comparison for P(53)19-2 transition	79
Figure A-1. Table setup for ring dye laser wavemeter calibration	88
Figure A-2. Definition of the "t" hyperfine component	91
Figure B-1. Approximating the volume of a cylindrical beam	92
Figure B-2. Polygon created by the intersection of two rectangles	93
Figure C-1. P(53) 19-2 Doppler-broadened Transition at the cold end	96
Figure C-2. P(53) 19-2 Doppler-broadened Transition at the warm center	96
Figure C-3. P(53) 19-2 Doppler-broadened transition at the hot end	97
Figure C-4. P(70) 17-1 Doppler-broadened transition at the 4" position	98
Figure C-5. P(70)17-1 residual trend for the 4" Doppler-limited fit	98
Figure C-6. P(70) 17-1 Doppler-broadened transition at the 3" position	99
Figure C-7. P(70)17-1 residual trend for the 3" Doppler-limited fit	99

Figure C-8. P(70) 17-1 Doppler-broadened transition at the 2" position	100
Figure C-9. P(70)17-1 residual trend for the 2" Doppler-limited fit	100
Figure C-10. P(70) 17-1 Doppler-broadened transition at the 1" position	101
Figure C-11. P(70)17-1 residual trend for the 1" Doppler-limited fit	101
Figure C-12. P(53) 19-2 Doppler-broadened transition at the 4" position	102
Figure C-13. P(53) 19-2 residual trend for the 4" Doppler-limited fit	102
Figure C-14. P(53) 19-2 Doppler-broadened transition at the 3" position	103
Figure C-15. P(53) 19-2 residual trend for the 3" Doppler-limited fit	103
Figure C-16. P(53) 19-2 Doppler-broadened transition at the 2" position	104
Figure C-17. P(53) 19-2 residual trend for the 2" Doppler-limited fit	104
Figure C-18. P(53) 19-2 Doppler-broadened transition at the 1" position	105
Figure C-19. P(53) 19-2 residual trend for the 1" Doppler-limited fit	105

List of Tables

	Page
Table 1a. Expansion parameters for the $X^1 \Sigma(0^+_g)$ state of I_2 . Valid for $v''=0-9$ ¹⁴	16
Table 1b. Expansion parameters for the $B^3 \Pi(0^+_u)$ state of I_2 ¹⁴	16
Table 2. Experimental line assignments	41
Table 3 Scan parameters and cell settings for Phase II	47
Table 4. P(70) 17-1 hyperfine fit parameters	66
Table 5. P(70) 17-1 data summary table	68
Table 6. P(53) 19-2 Hyperfine Fit Parameters	70
Table 7. P(53) 19-2 data summary table	70
Table 8. Reference temperature values at each measurement point	72
Table 9. Phase II hyperfine fit parameters for P(70)17-1	75
Table 10. Data summary for P(70)17-1 Phase II temperature measurements.	76
Table 11. Phase II hyperfine fit Parameters for P(53)19-2	78
Table 12. Data summary for P(53)19-2 Phase II temperature measurements.	79
Table 13. Future Experimentation.	83
Table A-1. Reference positions for "t" hyperfine components ²⁵	90

Abstract

Saturation spectroscopy techniques were used to demonstrate the ability to make spatially resolved temperature measurements by exploiting the $B^3 \Pi(0^+_u) - X^1 \Sigma(0^+_g)$ electronic transition in molecular iodine (I_2). Doppler-free saturation spectroscopy measurements resulted in hyperfine spectral profiles for the P(70) 17-1 and P(53) 19-2 ro-vibrational transitions between the electronic levels. Doppler-limited saturation spectroscopy, an adaptation of the Doppler-free technique in which beams propagate in the same direction and cross within the gas sample, allowed for the measurement of spatially resolved Doppler profiles for the same transitions.

The profiles were measured at several spatial positions in I_2 cells with measured temperature gradients. The technique did not produce accurate temperature readings; however, the saturation spectroscopy variant did produce profiles that were spatially resolved, with an interaction volume of approximately $12 \times 1 \times 1$ (mm units).

This thesis was motivated by the Air Force's Airborne Laser Laboratory (ABL), which has a need to discriminate a spatially distributed temperature distribution. The Chemical Oxygen Iodine Laser (COIL), which is the high power directed energy source for ABL, has a low concentration of I_2 as a reaction byproduct. Line-integrated optical temperature measurements inside the COIL reaction chamber have been higher than predicted, which can have a dramatic effect on the threshold condition for the laser. Spatially resolved temperature measurements would provide a diagnostic tool to identify hot spots and heat gradients in the supersonic flow region of the laser.

SPATIALLY RESOLVED TEMPERATURE DETERMINATION IN I₂ GAS USING DOPPLER-
LIMITED SATURATION SPECTROSCOPY

I. Introduction

A. Background/History

Using absorption spectroscopy to measure the temperature in a Doppler-broadened gas sample is hardly a revolutionary idea. In fact, the average temperature in such a medium can be easily obtained by projecting a tunable laser source through the gas and onto a photo-detector. The photo-detector measures changes in absorption levels as the source scans across the entire base width of a spectral line. The profile, assuming the medium is primarily Doppler-broadened, will have a width that is determined by the thermal velocities of the gas particles that interact with the laser beam.¹

Using this method, the laser beam will interact with all the gas particles in the beam path, and the temperature information can be extracted from the Doppler width (Full Width at Half Maximum, FWHM) using the formula:²

$$\Delta w_d = \frac{\omega_o}{c} \cdot \left(8 \cdot \kappa \cdot T \cdot \frac{\ln(2)}{m} \right)^{\frac{1}{2}} \quad (1)$$

where

Δw_d = Doppler width (FWHM)	ω_o = center frequency (rad/s)
c = speed of light	κ = Boltzmann's constant
T = temperature	m = molecular mass

Equation (1) assumes a Gaussian lineshape, which is a good assumption as long as Doppler broadening is the primary broadening mechanism in the sample.¹

The major problem with this approach for measuring the temperature is that the resultant value is the line-integrated temperature over the entire path of the laser beam through the sample. The measurement as such gives no information about the local temperature distribution in the gas (e.g. the measurement is not spatially resolved), but rather gives the average temperature of the gas over the laser beam path length.

In highly dynamic or turbulent gases spatially resolved temperature measurements would provide useful information about the media or the flow dynamics. Point-to-point measurements of temperature in such systems may differ significantly from the line-integrated average, especially in situations where sharp temperature gradients are expected. Using a spatially resolved measurement technique, a detailed mapping of temperature profiles in space could provide diagnosis of the thermal distribution of the sample gas.

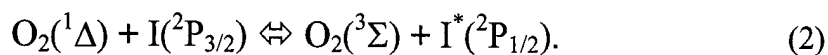
It is necessary that such a temperature measurement technique be non-intrusive to the experimental system. Of course, the easiest way to achieve spatially resolved temperature measurements is to introduce a thermocouple probe into the system. The probe, if moved from point to point, would measure the resolved temperatures; however, the presence of the thermocouple will influence dynamics and equilibrium temperatures in the gas species being measured. Optical measurements thus present an ideal means to avoid significantly disturbing the gas, while retaining the spatial resolution.

The need for the development of a simple optical technique to provide spatially resolved temperature information was inspired by the Airborne Laser Laboratory (ABL)

technical development team, located at Kirtland Air Force Base in Albuquerque, New Mexico. The ABL is using a Chemical Oxygen-Iodine Laser (COIL) for their primary high power laser source, and sees some utility in being able to measure a detailed spatial temperature map of the gas inside the reaction chamber of the laser.

COIL, being a chemical laser, relies on a chemical reaction to produce the pumping energy required to build a population inversion in atomic iodine. The primary reaction produces a singlet oxygen state (O_2 a $^1\Delta$) with a radiative lifetime of about 64 minutes. This state lifetime is not significantly diminished by collisional relaxation, and therefore acts as a metastable energy reservoir. Atomic iodine, which dissociates from I_2 downstream from this reaction, has an I $^2P_{1/2}$ energy state that is close in energy to the singlet, excited oxygen state. The energy from the metastable reservoir state of the oxygen can couple to excite the two-level inversion in the atomic iodine.³ Figure 1 shows a conceptual comparison of energy levels for the primary components in the COIL reaction chamber.

The resonant energy transfer reaction is given by:⁴



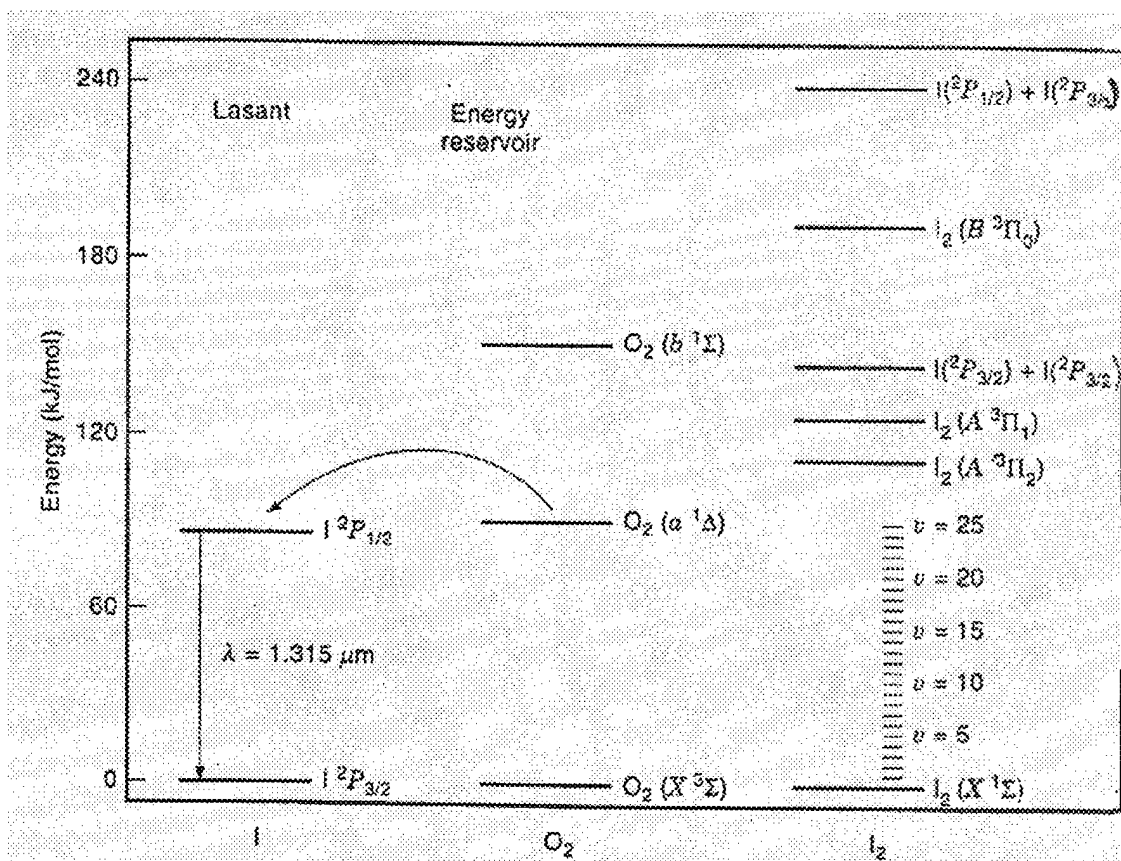


Figure 1. Energy level comparison for I, O₂, and I₂. The curved arrow shows the coupling between the excited oxygen state and the atomic iodine upper lasing state. The primary lasing transition in I is also designated, with a wavelength of 1.315 μm. Energy levels of I₂ are included to show the B-X transitions investigated in this thesis.³

The reaction cell for the COIL employs a vacuum to force the oxygen through supersonic nozzles. Molecular iodine (I₂) is injected at the entrance plane of the supersonic nozzles, as shown in Figure 2. The nozzles are present to cool the gases as they travel through the laser cavity, in order to control temperature-dependent losses and to increase the power flux. The I₂ dissociates in a complex series of kinetic interactions with the singlet oxygen state; however, trace concentrations of I₂ still remain past the exit plane of the nozzles.³ The I₂ will likely have the same temperature as the surrounding

gas components as the flow reaches the resonant cavity; it is this downstream temperature which is of interest.

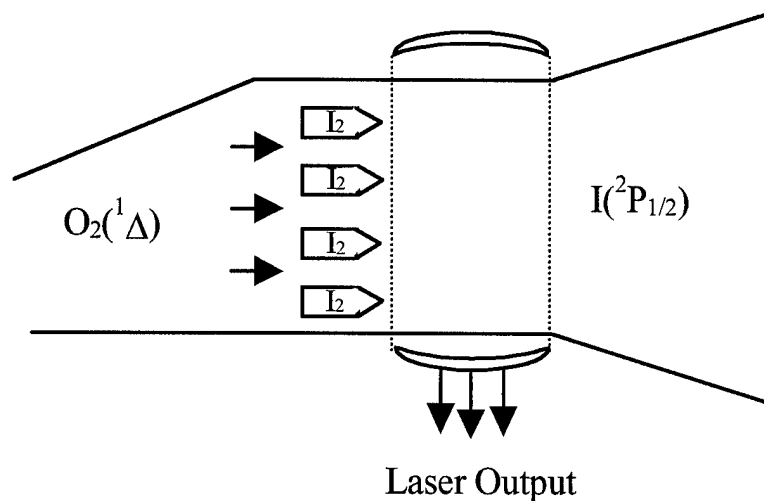


Figure 2. COIL nozzles and optical cavity. The I_2 is injected through the supersonic nozzles and dissociates, allowing for the resonant energy transfer from the excited oxygen to the atomic iodine. The lasing transition occurs aft of the nozzles in the resonant laser cavity.³

The temperature of the gas at the exit plane of the nozzles determines the threshold condition for lasing; a temperature change from room temperature to 160 K reduces the ratio of singlet oxygen to total oxygen concentration required for lasing from 15% to 5%.³ The efficiency is therefore greatly reduced by higher temperatures; since the COIL is to be the primary laser for development in ABL, efficiency is paramount in system design priority for the development of a practical platform. Weight of fuel gases, heat production, and laser output power are all contingent upon the efficiency of the system.

Informal communications between the Air Force Institute of Technology (AFIT) and the Air Force Research Laboratory's ABL branch (AFRL/DEL) have indicated that line-integrated temperature measurements made of the I_2 trace gas at the nozzle exit point

have yielded unexpected results. The measured temperature within the reaction chamber of the laser was measured 50 degrees (Kelvin) higher than predicted.

The ability to resolve and map the spatial temperature variation in the COIL will assist the ABL in determining the source of the high line-integrated temperature measurement. It is even possible that there is not a problem with the temperature distribution at the nozzle exit point, but that the higher measurement is a result of the line integration in the interaction volume. In any case, it is necessary to develop a technique that will assist in the diagnosis of the problem, or to determine if a problem even exists.

After several discussions with AFRL/DEL, AFIT personnel suggested that a variant of a well-known nonlinear laser spectroscopy technique could provide spatially resolved temperature information. This technique, known as saturation spectroscopy, is generally applied when one wishes to measure the hyperfine spectrum that comprises a Doppler-broadened transition. Counterpropagation of two split beams from a tunable source within the gas sample allows the elimination of the Doppler broadening altogether via Doppler-free saturation spectroscopy.

The elimination of the primary broadening mechanism allows the component hyperfine line positions and widths to be measured. Figure 3 shows the comparison of the absorption line to its component hyperfine line structure for the P(70) 17-1 transition in I_2 . The broadened profile is in actuality several orders of magnitude greater in amplitude than the hyperfine lines. The hyperfine line intensities have been exaggerated for the sake of comparison. The additions of these 15 hyperfine lines, when Doppler broadened, make the smooth profile.

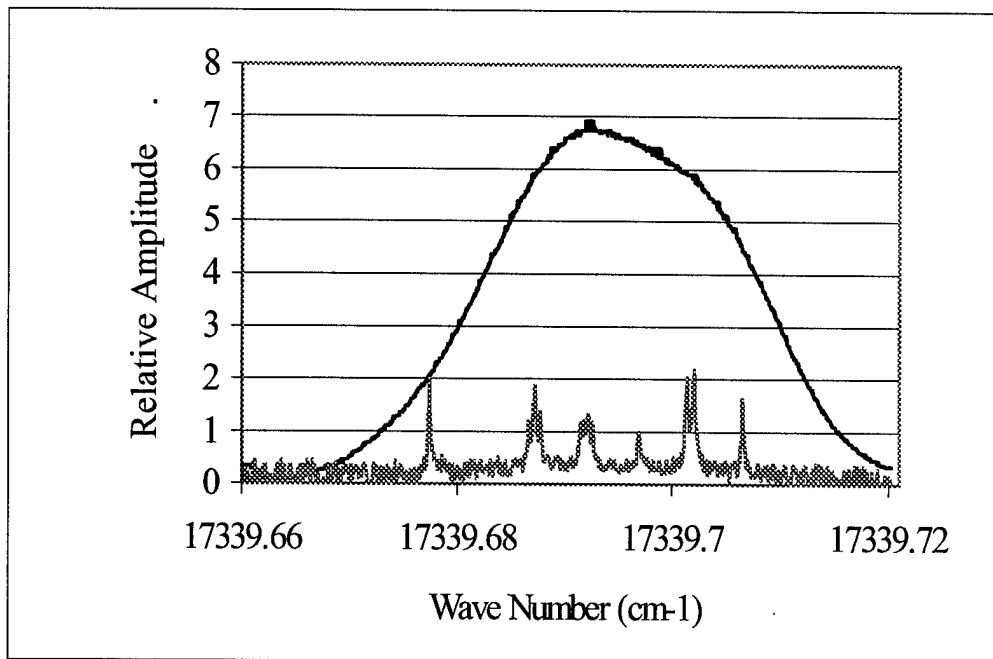


Figure 3. P(70) 17-1 Absorption line with component hyperfine structure. There are 15 hyperfine lines for this transition that, when Doppler broadened, sum together to form the broadened transition. This diagram is a relative illustration, since the broadened transition is in actuality several orders of magnitude greater in magnitude than the hyperfine lines.

In the Doppler-limited modification to the Doppler-free technique, the two laser beams instead copropagate and cross within the sample to yield the Doppler broadened profile only at the point where the two beams cross. If the beams cross at a small angle, there is again interaction with the same velocity group and the temperature information that is extracted from the Doppler width of the resulting line is spatially resolved. The position at which the beams cross can also be altered to obtain the temperature dependent, spatially resolved profiles at different spatial locations in the sample.

B. Objective

The primary objective of this work was to demonstrate the capability of Doppler-limited saturation spectroscopy for making spatially resolved temperature measurements in a molecular iodine gas. This included obtaining an understanding of the hyperfine interactions that compose I_2 absorption lines, and applying principles of Doppler broadening to retrieve temperature information from the profiles of the measured lines. The Doppler-free saturation spectroscopy experiment was slightly modified to not exclude, but to exploit the spatially resolved Doppler information to extract temperatures.

The laser source for the experiment was the Coherent 899 Ring Dye Laser, with a Rhodamine 590 dye to allow for tuneability from the 570 to 610 nm range. The overall approach was to measure the hyperfine structure for several broadened transitions, which were chosen because of their isolation in frequency space from other absorption lines, and for characteristics that may potentially increase sensitivity to temperature variations. Hyperfine measurements were made using standard Doppler-free saturation spectroscopy techniques. The experimental setup was then modified for Doppler-limited spatially resolved measurements by changing the direction of propagation for the stronger of two laser beams (the pump beam).

The resulting Doppler-limited profiles were then fit starting with the component hyperfine positions and natural linewidths as measured. A Doppler width was then assigned to these lines and was allowed to change as one of the fit parameters; therefore the broadened profile could be recreated by the addition of the hyperfine lines with a shared Doppler width. The profiles were measured at different points along the length of

a cell, heated at one end in order to create a measurable temperature gradient in the gas within the cell. These measurements were compared to those made by introducing a thermocouple probe into the cell under identical pressure conditions.

C. Presentation

The relevant theoretical background information is presented in Chapter II. The development covers the electronic transitions in molecular iodine, hyperfine splitting, Doppler-broadened transitions, Doppler-free, and Doppler-limited saturation spectroscopy. Chapter III describes experimental assemblies and includes the procedures for hyperfine measurements and for Doppler-limited measurements using two Iodine cell designs. Chapter IV presents the experimental results, including hyperfine structure profiles and corresponding Doppler broadened profiles, which are presented with detailed fit parameters and fit residual analysis. Chapter V gives the discussion of the results and recommendations, which include an outline of possible future work in this area of interest.

II. Theory

A. Electronic Transitions in I_2

The absorption spectrum of molecular iodine has been well investigated and catalogued since the birth of molecular spectroscopy. Specifically, the ro-vibronic transitions between the $X^1\Sigma_g^+ \rightarrow B^3\Pi_u^+$ electronic states have been extensively catalogued by using high resolution Fourier transform spectroscopy, and are presented in an atlas by Gerstenkorn and Luc to an accuracy of $\sim 0.002 \text{ cm}^{-1}$.⁴ A portion of the I_2 spectrum is shown in Figure 4; the primary lines chosen for the experiment lie within this range. The wealth of empirical information concerning absorption transitions in I_2 have led to a fair understanding of the physical structure of the molecule, and of its energy level structure.

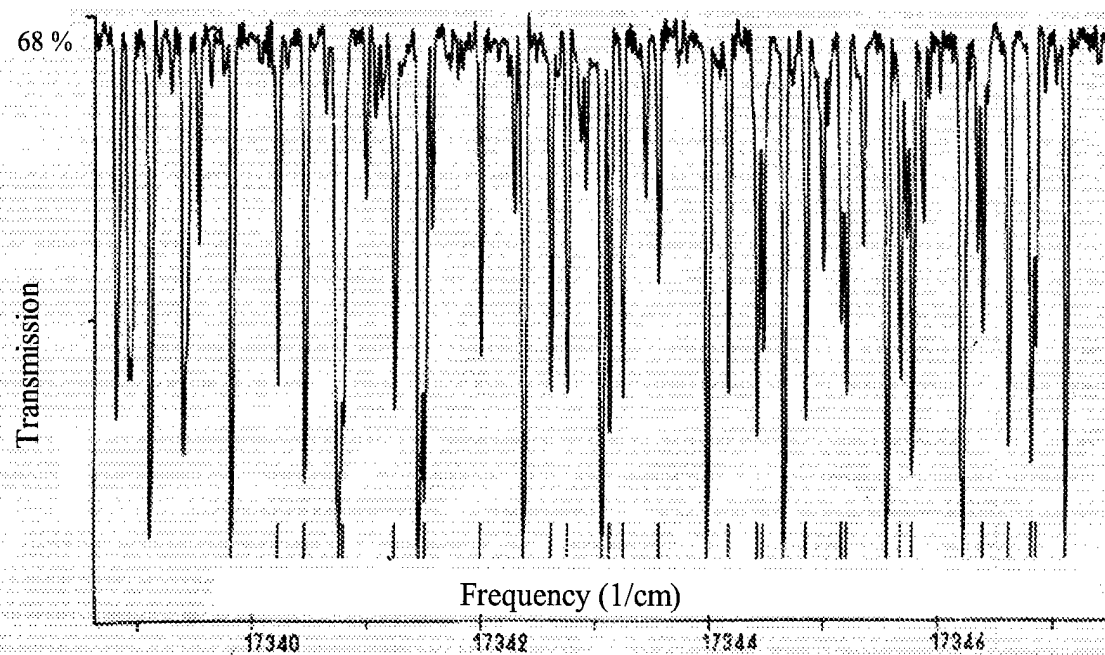


Figure 4. Iodine absorption spectrum. This spectrum shows the relative transmission through I_2 as a monochromatic laser source is scanned across frequency space.⁵

As with any diatomic molecule, molecular iodine has rotational and vibrational degrees of freedom. Rotational and vibrational states are created by the quantized nature of these motions, essentially splitting the electronic state as the physical configuration of the molecule changes.⁸ An illustrative potential diagram, Figure 5, shows the typical energy state hierarchy for a diatomic molecule. Within each electronic state there are vibrational states, in which there are rotational states. Simple transitions from one rotational state to another within the same vibrational level are possible; furthermore, vibrational transitions are possible within the same electronic state. Electronic transitions, however, are generally accompanied by ro-vibrational transitions.⁷

Vibration in the molecule causes the internuclear separation to change anharmonically. The motion is not perfectly harmonic because the Coulomb interaction between nuclei is stronger as the internuclear separation decreases, and is weaker as the separation increases. This causes the electronic potential curves to be asymmetric when compared to the theoretical parabolic potential of the harmonic oscillator.¹¹ Vibrational states are determined by the shape of the anharmonic potential, commonly referred to as the Morse potential.¹²

The term value for the vibrational energy levels is given by the Dunham Expansion, which is:¹¹

$$G_v = \sum_{j=0}^{j_{\max}} Y_{0j} \left(v + \frac{1}{2} \right)^j \quad (3)$$

where v is the vibrational quantum number and the expansion coefficients ($Y_{01}, Y_{02}, \text{etc.}$) are empirically determined by robust fitting routines that examine numerous vibrational

transitions in the molecule. Y_{00} is the electronic energy level, determined at the equilibrium point on the Morse potential curve; this expansion coefficient is often denoted as T_e . In iodine, these coefficients are very well determined and are used to predict and classify transitions. Table 1a shows the expansion coefficients for the ground state ($X^1 \Sigma(0^+_g)$), while those for the $B^3 \Pi(0^+_u)$ state are shown in Table 1b.

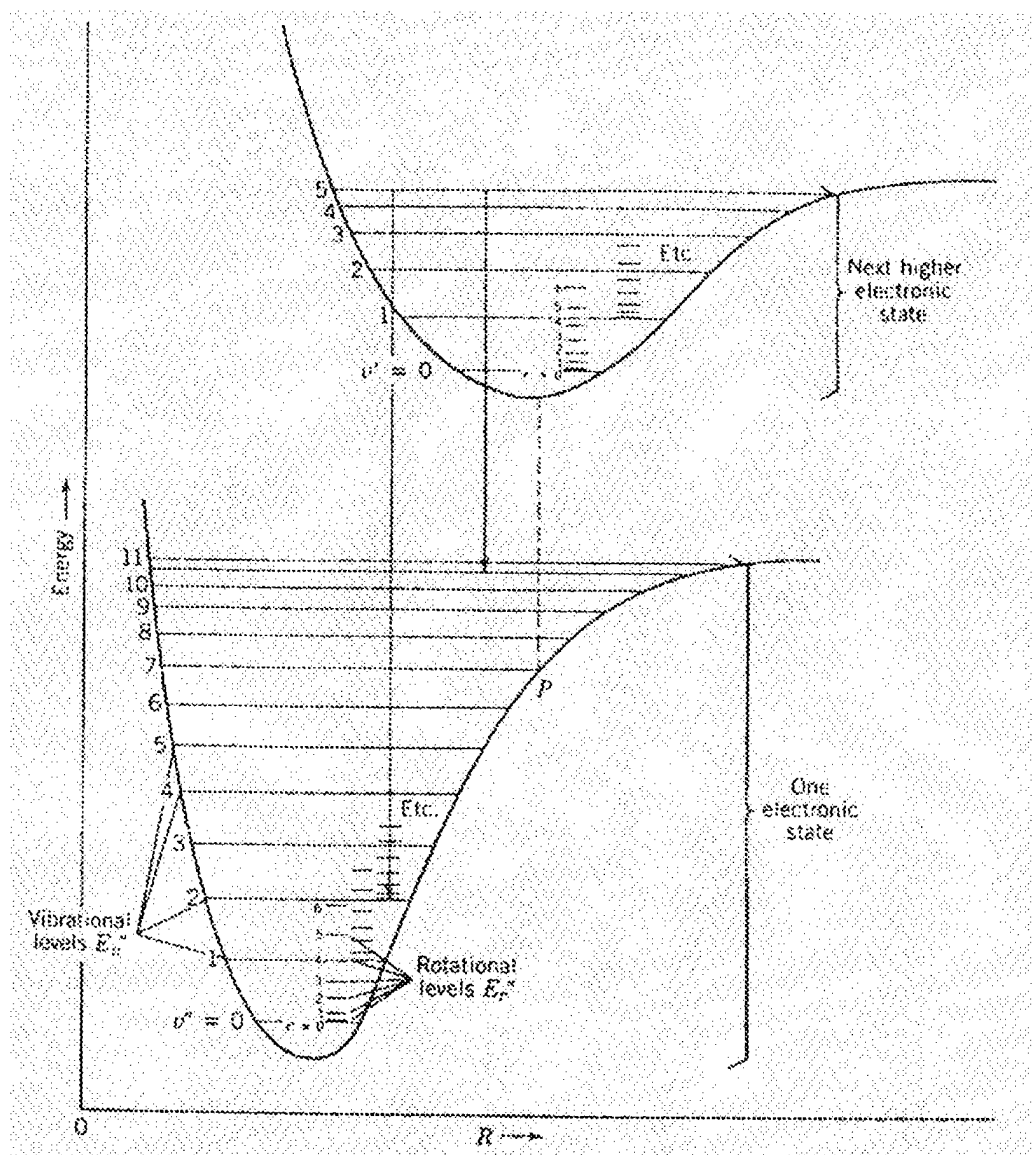


Figure 5. Typical diatomic energy level structure. Each electronic level has vibrational levels, and each vibrational level has rotational levels.⁹

For simple rotation, considering the molecule to be a rigid rotator, one finds that the resulting energy levels are evenly spaced as defined by the term symbol:

$$F(J)=B J(J+1) \quad (4)$$

where B is the rotational constant and J is the rotational quantum number. In actuality, since the molecule is not completely rigid, there is a centrifugal distortion that must be taken into account. The term value is then:

$$F(J)=B J(J+1)+D J^2(J+1)^2+H J^3(J+1)^3+\dots \quad (5).$$

Rotational branch structure is formed as a consequence of the selection rules for transitions in diatomic molecules. Transitions from state to state can occur in a diatomic molecule if $\Delta J = -1, 0$, or $+1$; the branches are defined as follows:

$$J' - J'' = 0 \text{ Q-Branch}$$

$$J' - J'' = +1 \text{ R-Branch}$$

$$J' - J'' = -1 \text{ P-Branch}$$

Figure 6 illustrates branch structure in typical diatomics by identifying the specific transitions and frequency distribution for a simple case.

The identification of the rotational transitions is very important for this work, since the number of hyperfine lines in a transition are determined by the rotational quantum number in the ground state, J'' . In I_2 there is no Q branch formation because the resultant angular momentum (Ω) for each state is zero. This is according to the selection rule¹³

$$\Delta J \neq 0 \text{ when } \Omega' = \Omega'' = 0 \quad (6)$$

As one can expect, vibration and rotation occur simultaneously in a molecule. If the molecule vibrates, the internuclear distance is changing; therefore, the angular momentum of the molecule is changing. The reverse is true as well.⁷ In order to compensate for this mutual interaction, the rotational constants are themselves expansions that depend on powers of $(v+1/2)$.¹⁴

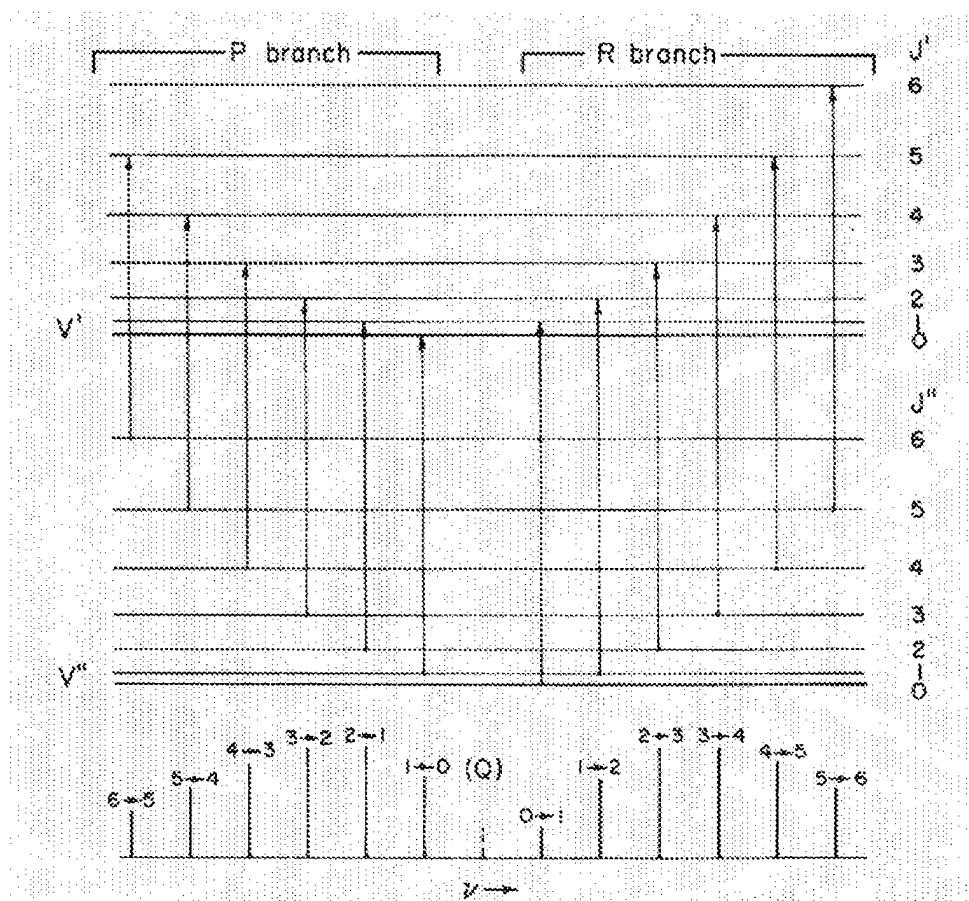


Figure 6. Branch structure in electronic transitions. The P- and R-branch transitions are conceptually illustrated for rotational transitions from the excited (Single – primed) electronic state to the lower (Double – primed) state.¹¹

The possible energy levels (in cm^{-1}) can then be approximated by the set of equations labeled (7) below:¹⁵

$$E(v, J) = \sum_{i=0}^{i_{\max}} \sum_{j=0}^{j_{\max}} Y_{ij} \left(v + \frac{1}{2}\right)^j \cdot J^i \cdot (J+1)^i \quad (7)$$

or

$$E(v, J) = Gv + Bv \cdot J \cdot (J+1) + Dv \cdot J^2 \cdot (J+1)^2 + Hv \cdot J^3 \cdot (J+1)^3 + \dots \quad (8)$$

where

$$\begin{aligned} Gv &= \sum_{j=0}^{j_{\max}} Y_{0j} \left(v + \frac{1}{2}\right)^j & Bv &= \sum_{j=0}^{j_{\max}} Y_{1j} \left(v + \frac{1}{2}\right)^j \\ Dv &= \sum_{j=0}^{j_{\max}} Y_{2j} \left(v + \frac{1}{2}\right)^j & Hv &= \sum_{j=0}^{j_{\max}} Y_{3j} \left(v + \frac{1}{2}\right)^j \end{aligned}$$

A sufficient set of expansion coefficients have been determined for the B-X transition in molecular iodine and are presented in Table 1, and are identified by the i and j subscripts corresponding to Equation (7). Since the lower vibrational levels of the ground state are more densely populated states at room temperature, the ground state parameters are only accurate (within 0.01 cm^{-1}) for the first 10 vibrational levels.¹⁴

Table 1a. Expansion parameters for the $X^1 \Sigma(0^+_{\text{g}})$ state of I_2 . Valid for $v''=0-9$ ¹⁴

ID	$Gv'' \text{ (cm}^{-1}\text{)} \{i=0\}$	$Bv'' \text{ (cm}^{-1}\text{)} \{i=1\}$	$Dv'' \text{ (cm}^{-1}\text{)} \{i=2\}$	$Hv'' \text{ (cm}^{-1}\text{)} \{i=3\}$
$\{j=0\}$	0	3.4368670E-02	4.5681230E-09	
$\{j=1\}$	2.1451860E+02	-1.1398970E-04	2.1204390E-11	
$\{j=2\}$	-6.0722840E-01	-2.7202910E-07	6.7374060E-13	
$\{j=3\}$	-1.3861100E+01	-5.4477080E-09		

Table 1b. Expansion parameters for the $B^3 \Pi(0^+_{\text{u}})$ state of I_2 ¹⁴

ID	$Gv' \text{ (cm}^{-1}\text{)} \{i=0\}$	$Bv' \text{ (cm}^{-1}\text{)} \{i=1\}$	$Dv' \text{ (cm}^{-1}\text{)} \{i=2\}$	$Hv' \text{ (cm}^{-1}\text{)} \{i=3\}$
$\{j=0\}$	15769.0485 (Te)	2.8993694599E-02	6.125767E-09	-2.150047340E-15
$\{j=1\}$	125.6724	-1.406799398E-04	1.418420E-10	7.915679522E-15
$\{j=2\}$	-7.5267700E-01	-5.088972976E-06	-2.825041E-12	-1.023966180E-14
$\{j=3\}$	-3.2462820E-03	8.751145403E-07	5.544495E-13	4.852619270E-15
$\{j=4\}$	1.8757360E-05	-1.171736403E-07	-2.644252E-14	1.199751560E-15
$\{j=5\}$	-3.4141240E-06	9.702596783E-09	9.539521E-16	1.792143124E-16
$\{j=6\}$	2.0049980E-07	-5.304859892E-10	-1.864100E-17	-1.755753490E-17
$\{j=7\}$	-6.9504140E-09	1.957112328E-11	1.813907E-19	1.185081818E-18
$\{j=8\}$	1.5178990E-10	-4.894864050E-13	-6.053203E-22	-5.675954430E-20
$\{j=9\}$	-1.8997900E-12	8.1736417235E-15		1.958960707E-21
$\{j=10\}$	1.2269410E-14	-8.715621632E-17		-4.888492740E-23
$\{j=11\}$	-3.1373120E-17	5.360997383E-19		8.739722535E-25
$\{j=12\}$		-1.445945450E-21		-1.091263060E-26
$\{j=13\}$				9.034911061E-29
$\{j=14\}$				-4.455602540E-31
$\{j=15\}$				9.904029815E-34

Once the parameters are used in their corresponding expansion terms, the energy level structure can be approximated. The first few energy levels in I_2 are shown in Figure

7. There is a dissociative (repulsive) energy level which intersects the $B^3 \Pi(0^+_{\text{u}})$ state which causes significant predissociation. There are many strong transitions in molecular

iodine in the visible spectrum, caused by the strong absorption character created by the difference of the equilibrium separation in the X and B bound states.¹⁶

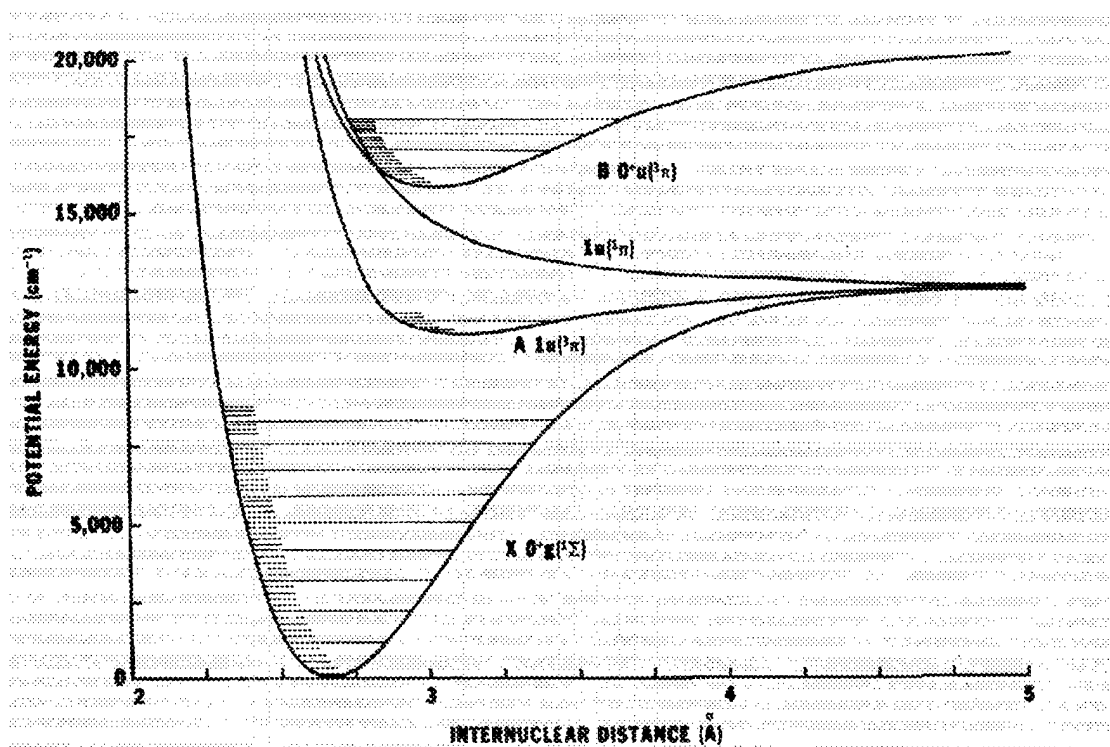


Figure 7. Energy level structure for the first few electronic levels in I_2 . Note that the B state has significant predissociation caused by the crossing of a repulsive potential level.¹⁶

The importance of identifying specific transitions is made clear in the next section.

The transitions for this experiment were largely chosen because the absorption lines were well isolated in frequency space. Once chosen, line assignments had to be made using the expansion parameters and the preceding development in order to determine the primary characteristics of the hyperfine structure for each absorption line.

B. Hyperfine Structure in I₂

Prominent absorption lines in a low pressure molecular iodine gas sometimes have FWHM's that are as much as twice as large as that calculated for a simple Gaussian line shape determined by the Doppler effect.¹⁷ The discrepancy had, prior to 1970, been attributed to unresolved hyperfine splittings. The advent of Doppler-free saturation spectroscopy allowed for the resolution of hyperfine interactions, which previously had been measured and characterized only for transitions in the microwave regions of the spectrum.^{17,18}

Hyperfine splittings are attributed to the interaction between the electronic and nuclear spin angular momentum, which splits the fine spectrum created by spin-orbit coupling. The nucleus of I¹²⁷ has a large magnetic dipole moment, caused by the spin of the nuclear particles; in addition, there is a large electric quadrupole moment created by the nonuniform charge distribution in the nucleus. Like all spectroscopic transitions, hyperfine splittings are caused by electric and magnetic fields that interact with these moments.¹⁰

The quantum number J is typically defined by the addition of the spin and orbital angular momentum. If we denote the resultant spin due to the charged particles within the nuclei in a diatomic particle as T, then we can define a new quantum number for the total angular momentum, inclusive of nuclear spin:¹³

$$F = J + T, J + T - 1, J + T - 2, \dots | J - T | \quad (9)$$

$T = 2I$, where I is the spin vector of each nucleus

I^{127} has a nuclear spin of $5/2$, such that the possible values for T are 5, 4, 3, 2, 1, 0.¹⁷

The number of hyperfine states corresponding to each rotational state is determined by the sum of possible T degeneracies, and is mathematically given by:

$$N_s = \sum_n 2 \cdot T_n + 1 \quad (10)$$

There is a restriction, however, on the possibilities for T -values, depending on whether the states have an even or an odd J .¹⁹ The total wavefunction of a homonuclear diatomic molecule with any half-integer nuclear spin must be antisymmetric under exchange of the nuclei, in agreement with the Pauli exclusion principle. The B state in molecular iodine is ungerade, meaning that it has odd electronic symmetry, while the X state is gerade.²⁰

In an ungerade state, such as the B state in I_2 , only states of odd T values can combine with odd J states; therefore, odd J -states have $N_s=21$ by

$$[2(5) + 1] + [2(3) + 1] + [2(1) + 1] = 11 + 7 + 3 = 21$$

Likewise, in an ungerade state, the even levels can only combine with even T values, such that $N_s=15$. Because of the change in electronic symmetry for gerade states, such as the X state, the rules are reversed. For odd J levels in gerade states there are 21 substates and for even levels there are 15.¹⁰

Therefore, for P- or R-branch transitions, there are the same numbers of splitting states in both of the energy levels, such that there are either 21 or 15 hyperfine lines in

one broadened absorption line. For even J'' , there are 15 hyperfine lines, while for odd J'' , there are 21 hyperfine lines for I_2 . The selection rule for hyperfine transitions is that $\Delta F=0$, meaning that there will be as many transitions as there are splittings for a given $J'-J''$ transition for I_2 .¹¹ A conceptual level diagram is shown in Figure 8; the dotted transitions are those excluded when there are only 15 hyperfine lines splittings in the states.

There is no electronic magnetic field along the J direction in either of the two states being investigated. The B state may have a magnetic moment which is along the internuclear axis; however, since $\Omega = 0$, the direction of this field must be orthogonal to J .¹⁸ Therefore the hyperfine splitting caused by the magnetic dipole moment interaction is a minor effect, caused by the interaction of the nuclear spin with a component of angular momentum induced by the end over end rotation of the molecule as a whole.²¹ The electric quadrupole term is the dominant mechanism behind the hyperfine splitting in I_2 . The total Hamiltonian for the splitting terms is $H_{NEQ} + H_m$, where the terms are of the form:¹⁰

$$H_{NEQ} = eQq_j \left[\frac{3 \cdot (\mathbf{I}_1 \cdot \mathbf{J})^2 + \frac{3}{2} \cdot (\mathbf{I}_1 \cdot \mathbf{J}) - |\mathbf{I}_1| \cdot |\mathbf{J}|}{2 \cdot I_1 \cdot (2 \cdot I_1 - 1) \cdot J \cdot (2 \cdot J - 1)} + \frac{3 \cdot (\mathbf{I}_2 \cdot \mathbf{J})^2 + \frac{3}{2} \cdot (\mathbf{I}_2 \cdot \mathbf{J}) - |\mathbf{I}_2| \cdot |\mathbf{J}|}{2 \cdot I_2 \cdot (2 \cdot I_2 - 1) \cdot J \cdot (2 \cdot J - 1)} \right] \quad (11)$$

where

Q =electric quadrupole moment q_j =average E-field gradient along J direction

e =charge of an electron

and

$$H_m = \frac{\mu G}{I_1} \cdot (\mathbf{I} \cdot \mathbf{J})$$

(12)

where $\mu G/I_1$ = Spin-rotation coupling constant

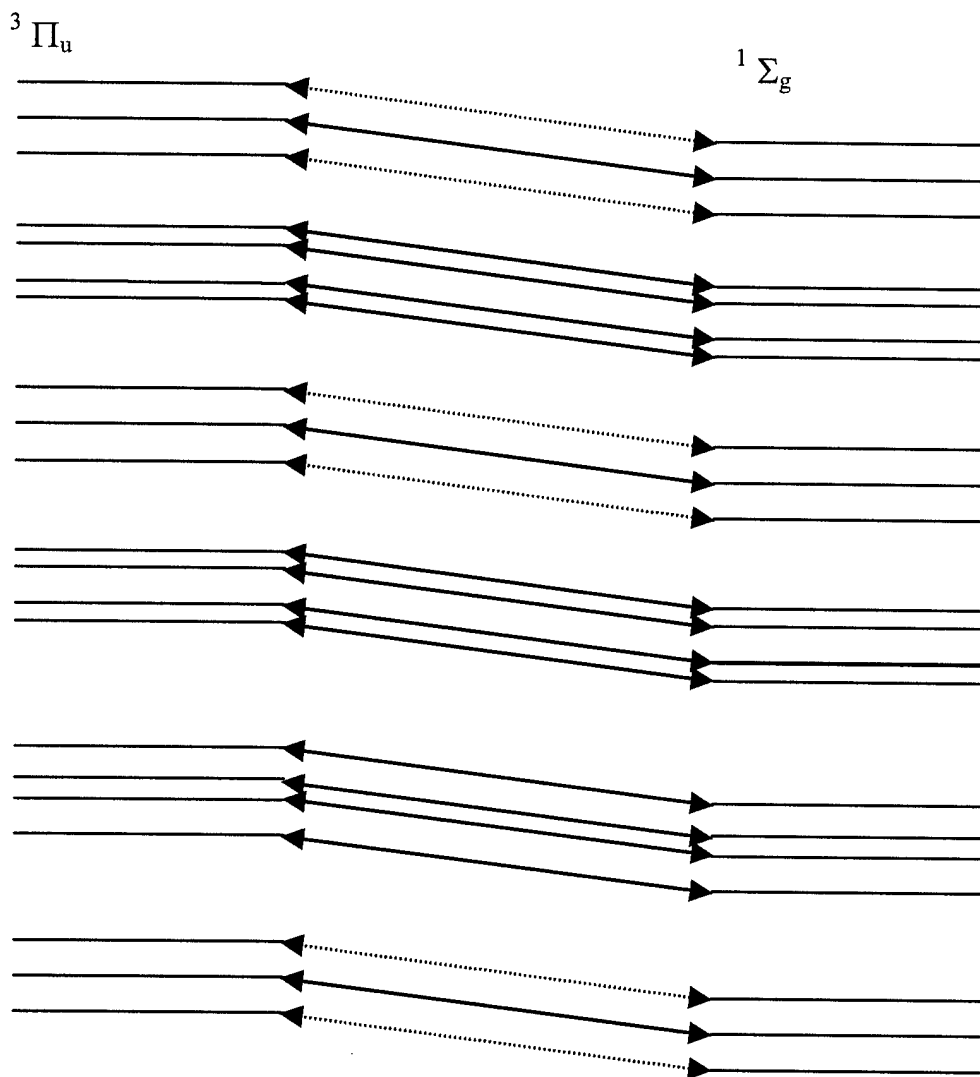


Figure 8. Hyperfine transitions in I_2 . In each electronic state the individual splittings are due to the possible quantized F -values. The dotted lines designate transitions that do not occur for even J'' interactions, such that there are 21 odd J'' hyperfine transitions and 15 even J'' hyperfine transitions.¹⁹

In actuality, finding the energy values using the Hamiltonian equations (11) and (12) requires diagonalization of a nontrivial matrix. However, an approximate solution can be formulated, with the assumption that $J \gg I$; this condition will be met for the transitions in this experiment. Recognizing that M is the projection of I along the axis parallel to F , the total angular momentum vector, the approximate solution of the equations takes the form:¹⁰

$$E_{\text{NEQ}} = \frac{eQq_j}{8 \cdot I_1 \cdot (2 \cdot I_1 - 1)} \cdot \left[3 \cdot (M_1^2 + M_2^2) + \frac{3}{J} \cdot \left[M_1 \cdot \left[M_1 \cdot (M_1 + 1) - I_1 \cdot (I_1 + 1) + \frac{1}{2} \right] + \dots \right. \right. \\ \left. \left. M_2 \cdot \left[M_2 \cdot (M_2 + 1) - I_1 \cdot (I_1 + 1) + \frac{1}{2} \right] \right] \right] \quad (13)$$

$$E_m = \frac{\mu G}{I_1} \cdot (M_1 + M_2) \cdot J \quad (14)$$

These equations provide approximate expressions for relative position of the hyperfine lines. The theoretical intensities of the lines, however, are proportional to $2F+1$.¹⁸ It is important to note that the constant terms at the beginning of each equation are transition dependent. For this work the major requirement is that the hyperfine intensities are matched with the correct relative line positions; absolute line positions are not needed for the analysis. Therefore, in this thesis, I will choose the representative values $eQq_0 = -2900$ MHz, $\mu G/I_1 = 49.0$ kHz, $\Delta eQq = 1936$ MHz. These are the values used by Levenson for the P(117) 21-1 transition; the use of these values will give the relative positions of the hyperfine lines.¹⁰

Figure 9 shows the typical electric quadrupole hyperfine splittings in I_2 versus increasing J . Again, the dotted lines show the transitions which do not occur for even J

transitions, in which there are only 15 hyperfine lines. The magnetic dipole splitting tends to shift these lines, and can cause certain components to cross over one another. For the purpose of this thesis, both coupling terms will be included in the approximate solution to the Hamiltonian.

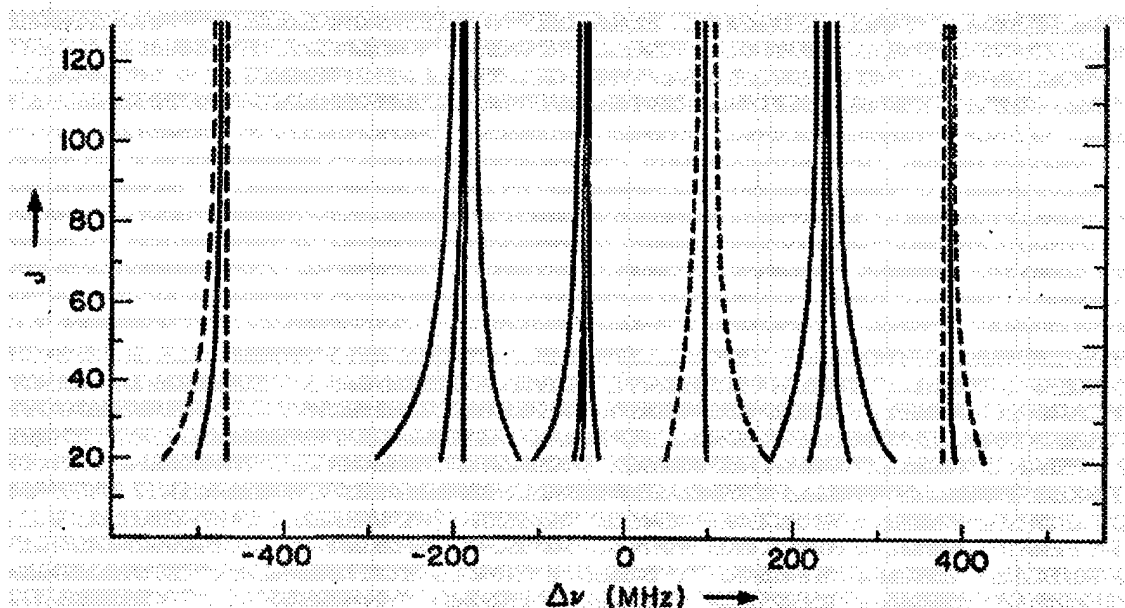


Figure 9. Hyperfine splittings from the electric quadrupole interaction in I_2 . As J increases, the splittings are closer to one another in frequency space. $\Delta\nu$ is the relative frequency, when an arbitrary point in the hyperfine spectrum is chosen as a zero, or center point.¹⁰

The addition of the hyperfine components forms a single broadened absorption line and account for the discrepancy in the FWHM that was mentioned at the beginning of this section. The Doppler broadening of the hyperfine lines for different temperatures make profiles that are unique in the sense that each profile belongs to a separate temperature. Figure 10 illustrates the theoretical superposition of the hyperfine lines at increasing temperatures. The plot starts with very sharp hyperfine lines at the bottom of

the plot. Each subsequent curve in the vertical direction constitutes a 50-degree (Kelvin) increase in temperature; all relative hyperfine intensities are theoretically justified by a calculation of the factor $2F+1$ for each line.

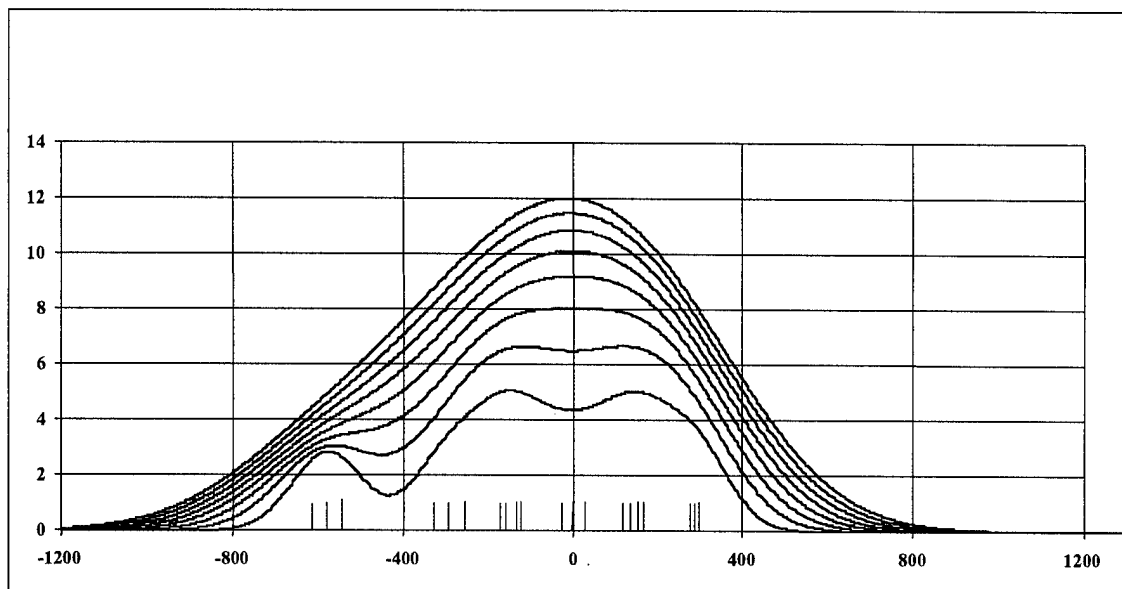


Figure 10. Single transition profiles vs. temperature. The hyperfine intensities are set to be proportional to $2F+1$. At 0 degrees Kelvin, the hyperfine lines form a discrete spectrum, as in the bottom of this plot. As temperature increases, the profile takes a less-defined shape as the broadened hyperfine lines begin to overlap. Each subsequent curve represents a 50 Kelvin increase in temperature.

C. Doppler Broadened Transitions

The frequency ω_0 which interacts with a particle moving at velocity v is Doppler shifted in the particle's frame of reference to a new frequency $\omega_0 + \mathbf{k} \cdot \mathbf{v}$, where \mathbf{k} is the propagation vector of the light. Generally, when dealing with light interacting with a gas of atoms or molecules, any volume will have a Maxwellian distribution of velocities in all directions.

The absorption coefficient for the gas being illuminated is typically of the Voigt integral form:²²

$$\alpha(\omega) = \frac{(N_1 - N_2) \cdot 2 \cdot \sqrt{\pi} \cdot (|\mu_{12}|)^2 \cdot k \cdot \gamma}{\epsilon_0 \cdot h \cdot (2 \cdot \kappa \cdot T)} \int_{-\infty}^{\infty} \frac{e^{-\left(\frac{m \cdot v}{2 \cdot \kappa \cdot T}\right)^2}}{(\omega - \omega_0 - k \cdot v)^2 + \gamma^2 + \gamma \cdot \tau \cdot (|\chi|)^2} dv \quad (15)$$

γ =transverse relaxation rate $\gamma = (\gamma_1 + \gamma_2)/2$

τ =longitudinal relaxation time $\tau = (\gamma_1^{-1} + \gamma_2^{-1})/2$

μ =electric dipole operator ϵ_0 =permittivity of free space

κ =Boltzmann's constant χ =the characteristic Rabi frequency

k =propagation constant T =temperature

The Voigt integral is essentially the convolution of a Gaussian lineshape and a Lorentzian lineshape, in this case the Doppler broadened profile and the homogeneously broadened profile. In the limiting case, when the Doppler broadening is much more prominent than the homogeneous broadening, the absorption coefficient reduces to:²²

$$\alpha(\omega) = \alpha_0 \cdot e^{-\frac{m^2 \cdot (\omega - \omega_0)^2}{(2 \cdot \kappa \cdot T \cdot k)^2}} \quad (16)$$

and the Doppler width (FWHM) is given as:²³

$$\Delta\omega_D = \frac{\omega_0}{c} \cdot \left(8 \cdot \kappa \cdot T \cdot \frac{\ln(2)}{m} \right)^{\frac{1}{2}} \quad (1)$$

From a measurement of the FWHM of a single broadened line, one can extract the temperature information, simply from the shape of the distribution.

In the case where the absorption line is composed of hyperfine lines, as in this experiment, the broadened absorption profile has a FWHM that is much larger than what is predicted by Equation (1). This is because the profile is actually the sum of the hyperfine lines, each of which is broadened according to the temperature of the I₂ gas. When trying to extract temperature information, it is necessary to incorporate the positions of the hyperfine components. Their Doppler widths, barring any nonlinear phenomena in the medium, are shared and reflect the true temperature of the gas.

If one wishes to illuminate the medium with a monochromatic, coherent light source:

$$\mathbf{E}(\mathbf{r}, t) = E_0 \cos(\omega t + \Pi - \mathbf{k} \cdot \mathbf{r}) \quad (17)$$

\mathbf{k} =propagation vector

\mathbf{r} =3-D position vector

ω =frequency of oscillation

t =time

only those molecules, which are Doppler, shifted into resonance with the incident field will interact.²³ The incident radiation can therefore only be absorbed by molecules within a narrow region of velocity space. Molecules that lie outside this region see a frequency shifted so far from resonance that absorption is impossible.¹⁰ The population of the upper state (N₂) will be increased at the resonant velocity component v_{res} .²²

$$v = v_{\text{res}} = \frac{\omega - \omega_0}{k} \quad (18)$$

Likewise, the lower state (N_1) population decreases at the same velocity component. The velocity space profiles for the upper and lower state, then, have distributions that appear similar to Figure 11.

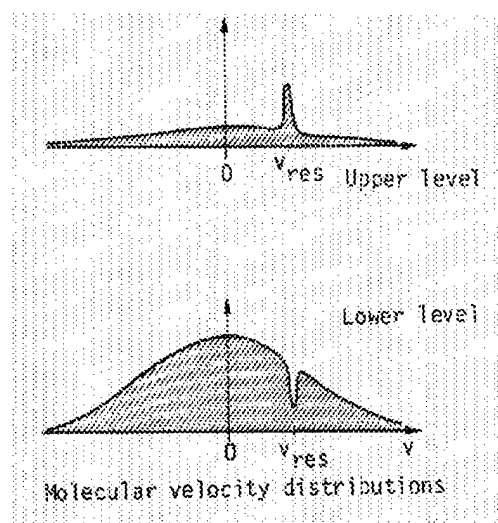


Figure 11. Velocity distributions for $N_1(v)$, $N_2(v)$. The incident radiation interacts with one velocity group, causing absorption to occur only at v_{res} . This causes N_1 to be depleted at this velocity, and N_2 to increase. ²²

This phenomenon, known as hole burning, occurs because a Doppler-broadened profile can be described by an addition of many naturally broadened lines, each with a Doppler-shifted center frequency, as in Figure 12.

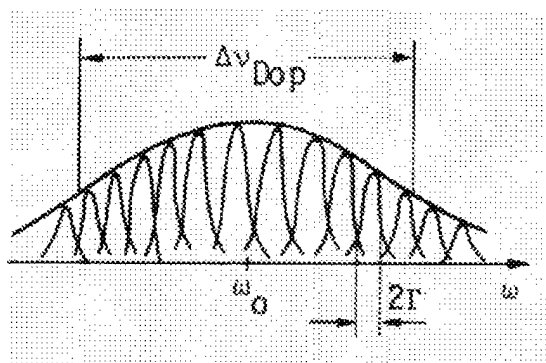


Figure 12. Doppler profile as a superposition. The broadened line is composed of lines that are naturally broadened, each with a center frequency that is Doppler shifted with respect to the incident radiation. ²⁴

The change in the velocity distributions for N1 and N2, illustrated in Figure 11, cause a hole to form in the absorption profile at the source's frequency. At this point, called the Bennett Hole, the absorption in the medium is lower because the upper states become more populated. In fact, if the source power is pushed past the saturation intensity for the medium, the medium becomes transparent to the source frequency. If the source is scanned over the frequency range of the entire broadened transition, the Bennett hole will move through the entire profile in frequency space.

The frequency of the monochromatic source therefore defines what velocity component in the medium will interact with the beam. Figure 13 shows three possibilities for frequency interaction in a Doppler broadened medium. For case a, the light can only interact with the molecules that have no projection of their physical velocities onto the propagation vector; the particles that interact with this incident frequency have velocities which are perpendicular to the incident beam direction. When $v > v_0$ (case b), the wave interacts with molecules that have positive projections of their velocities onto the wave propagation vector, and a hole is burnt into one side of the absorption curve. Likewise, case c involves a negative projection of particle velocity onto the propagation vector, and the hole appears at the opposite side of the profile from case b.

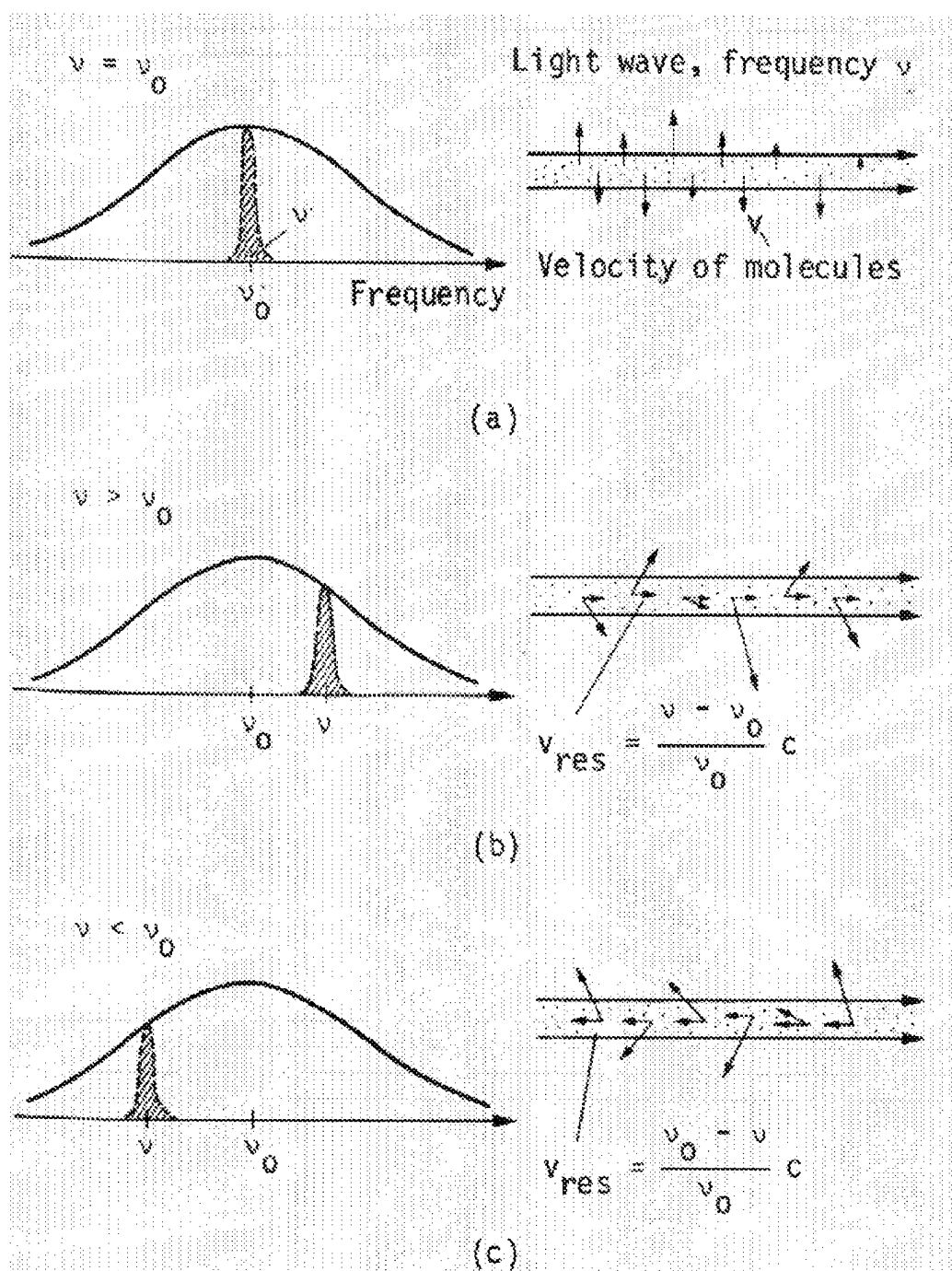


Figure 13. Interactions for three incident frequency cases. The three distinct frequencies interact with molecules that have different axial velocities, causing holes to be burnt at different locations in the Doppler-broadened profile.²⁴

Now it is useful for the purpose of this thesis to consider the case where two monochromatic waves of the same frequency are allowed to counterpropagate through the medium. The beam in one direction burns a hole on one side of the absorption profile, while the beam in the other direction burns a hole on the other side; there will be two holes that are symmetric about the center frequency of the absorption curve. The beams interact with separate (in fact, opposite) axial velocity groups, and so there are two distinct depressions in the absorption profile.²³

If, however, the source is scanned across the profile, the beams will reach a point where they both cross the center frequency. At this point the beams are interacting with the same velocity subgroup, namely $v_z=0$, as Figure 14 a illustrates.

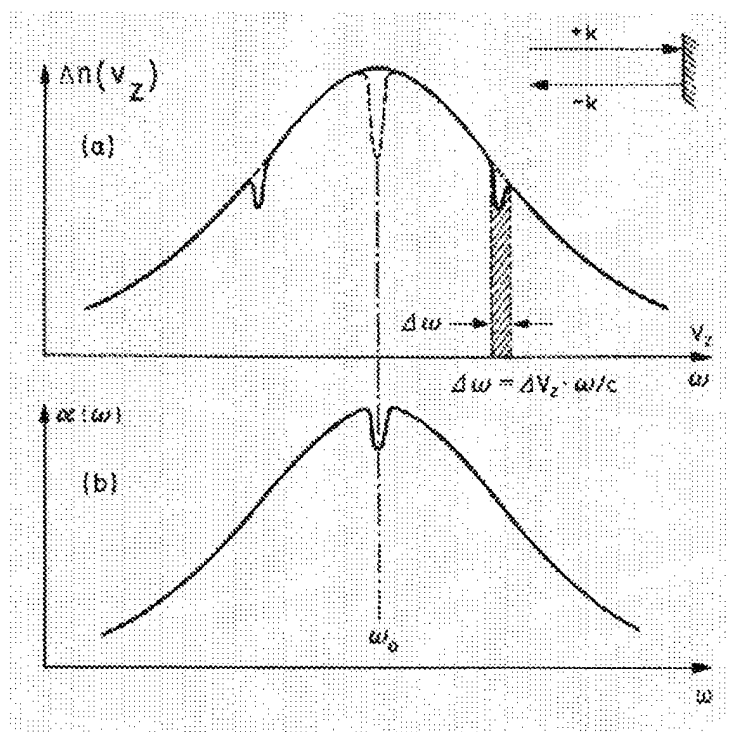


Figure 14 a. The Bennett hole caused by counterpropagation. Two beams of the same frequency are allowed to counterpropagate through a medium, causing two holes to be burnt into the absorption profile due to the interaction with opposite axial velocity components. At the center frequency for the profile, both beams interact with the same velocity subset.²⁴

At all other points there are two separate interaction groups; in the center, the intensities add linearly, and there is only one point of interaction. Because of this single point of interaction, there is a dip in the intensity profile of the beams after passing through the medium. The depression in the intensity curve is the Lamb Dip, illustrated in Figure 14 b.²²

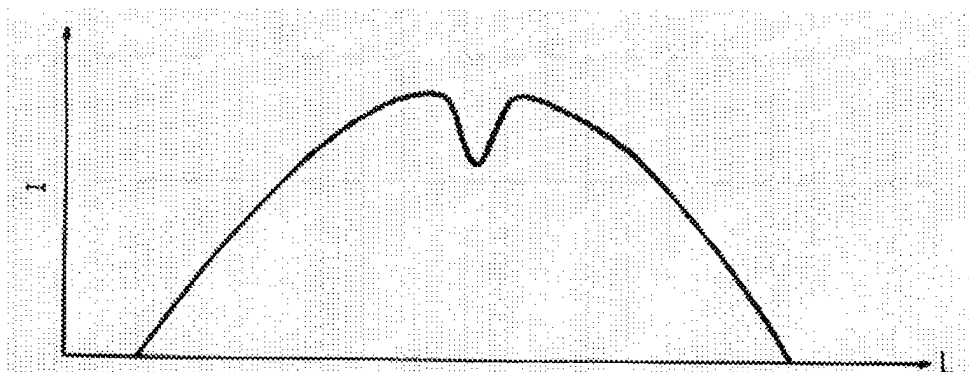


Figure 14b. The Lamb dip in the intensity profile. The dip in intensity at the center is created because the beams, which previously had interacted with two separate velocity groups in the medium, now influence the same velocity group. The absorption profile rises when the beams cross at the center frequency due to the mutual interaction, so transmitted intensity dips.²⁴

The interaction of counterpropagating laser beams with the common Zero axial velocity subgroup is the key to the understanding of Doppler-Free Saturation Spectroscopy. The fact that there is common interaction for both beams with the same molecule velocity component allows for elimination of the Doppler information concerning a transition. Once Doppler broadening has been eliminated, the hyperfine interactions can be easily resolved.

D. Doppler-Free Saturation Spectroscopy

As in the previous section, counterpropagating two beams from a tunable laser source and scanning in frequency through the range of a broadened line ensures that at some point both beams will interact with the same group of molecules in velocity space. The general diagram used to design Doppler-free saturation experiments is shown in Figure 15. Note that there is a finite angle between the beams.

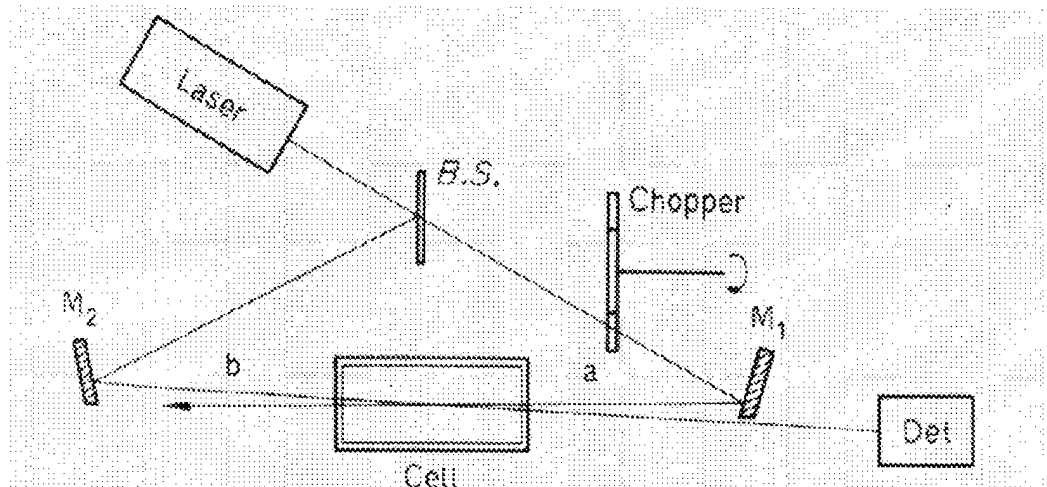


Figure 15. Typical zero-Doppler hole burning spectroscopy setup. The two beams counterpropagate within the gas cell, and cross at a small angle, to ensure mutual interaction with the molecules at the center of the absorption profile. Though both beams traverse the medium, only the unchopped beam is monitored for intensity fluctuation caused by the modulation of the absorption curve by the presence of the modulated beam.²³

There are vector components of the beams that are counterpropagating in the overlap region, ensuring the mutual interaction with the axially stationary molecules. The weaker beam, the probe beam, is the beam whose absorption will be measured by the photo-detector after crossing through the interaction volume in the cell. The stronger pump

beam is modulated at a reference chopping frequency ω_{ch} , while the probe beam is allowed to propagate as a continuous wave (CW).²³

The pump beam intensity oscillates between total illumination and no illumination, causing the absorption profile at the beam's frequency location to be modulated. A hole appears and disappears on one side of the profile, off the center point. At the same time the probe beam burns a smaller hole on the other end of the profile, which does not oscillate. Figure 16 shows an example of what the profile may look like for a given off-center frequency component in the absorption profile for one broadened transition.²⁴

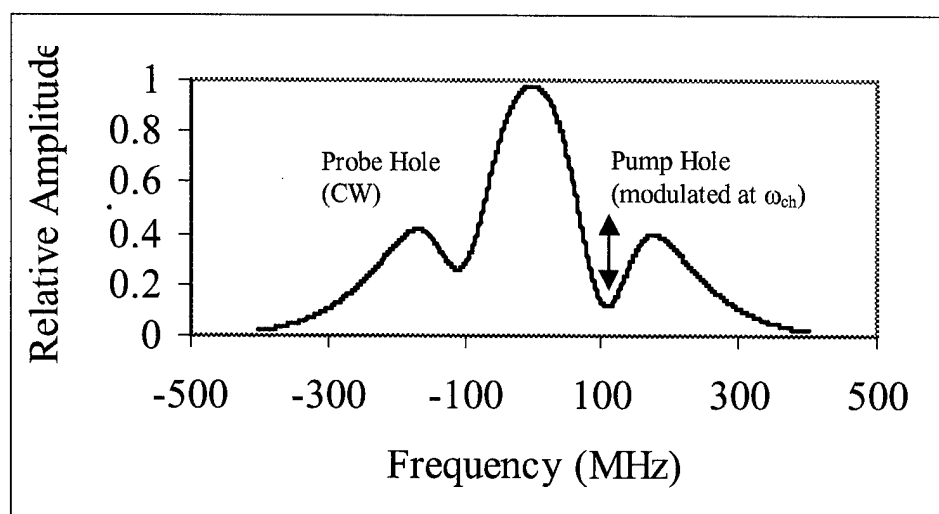


Figure 16. Absorption holes for 0 Doppler saturation spectroscopy. The pump hole oscillates at the chopping frequency, while the probe beam burns a continuous hole at the opposite point in the profile. As the beams scan through the center of the profile, the CW probe beam will "feel" the suppression of the absorption curve caused by the presence of the pump beam and will have a transmitted intensity that is modulated at the chopping frequency.

As the laser scans in frequency space, the beams eventually will interact with the same velocity subgroup at $v_z = 0$. At that point in frequency the modulated pump hole

and the CW probe hole overlap. The power transmitted by the probe beam will be modulated by the presence of the chopped pump beam in the same spatial location, interacting with the same velocity group. As the absorption curve is suppressed by the pump beam, the probe beam will have a higher transmission through the medium. On the other hand, when the pump beam is blocked by the chopper wheel, the probe beam absorption will be greater. Figure 17 shows the modulation of the pump beam by the chopper wheel, with the corresponding effective modulation on the probe beam absorption and intensity.

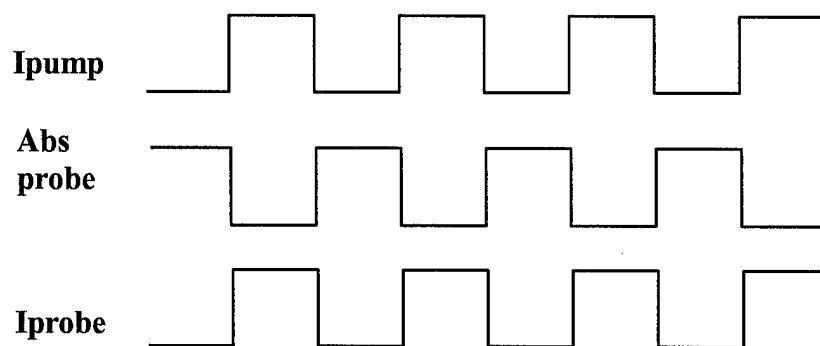


Figure 17. Probe and pump beam modulations

A lock-in amplifier can be used to detect the modulated probe beam signal created by both beams being present in the same spatial region at the same time. The result of the chopping of the pump beam and the subsequent modulation of the probe beam ensure spatial resolution for the Doppler-free measurements. The lock-in amplifier turns the oscillation into a DC signal that reflects the absorption level of the counterpropagating beams. The profile, as the laser frequency is scanned, will cross through the zero Doppler points for each of the hyperfine transitions, creating profiles which do not

contain any of the Doppler-broadening information. The lock-in signal maps out the naturally broadened hyperfine structure as the laser scans through the frequency range of the broadened line.

E. Doppler-Limited Saturation Spectroscopy

There is another way to ensure that the two beams interact with the same velocity subgroup within the velocity distribution. Instead of counterpropagating to cause mutual interaction with the $v_z = 0$ molecules in the overlapping spatial region, the beams can copropagate to overlap not at the Zero Doppler point in the absorption curve, but at some other velocity component. Since the beams copropagate, the holes are burned into the profile at the same frequency location, but away from the Zero Doppler region of the profile. The interaction between the pump and probe beams is the same; the difference is that the lock-in signal now maps a broadened profile as the laser scans in frequency, with all Doppler information intact.

The spatial overlap of the beams also does not change for Doppler-limited saturation spectroscopy. The probe beam will still only show a measurable signal when the two beams are present in the same spatial volume at the same time. The probe beam will be modulated at the pump modulation frequency, as before, but will retain the complete Doppler information for the point at which the beams overlap. Scanning in frequency results in a Doppler profile limited to the volume of mutual interaction between the two copropagating beams. Figure 18 shows the conceptual setup image.

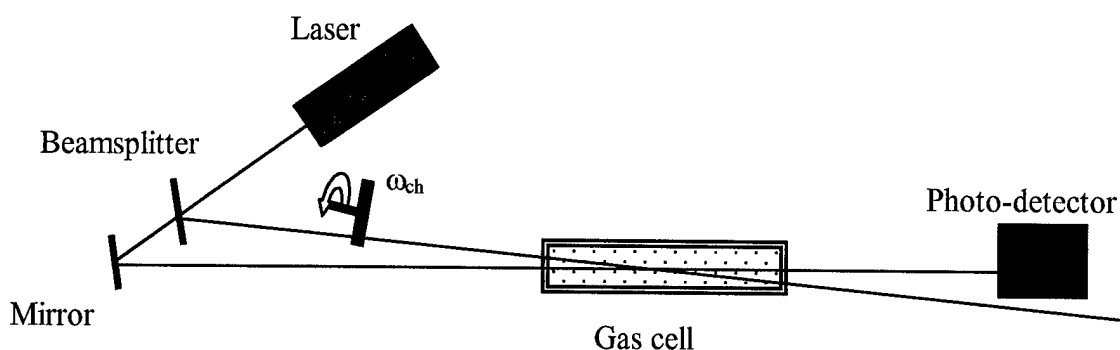


Figure 18. Setup diagram for Doppler-limited hole burning spectroscopy. This variant of the standard technique allows the beams to copropagate rather than counterpropagate, still allowing the pump beam to be modulated by a chopper.

This simple variant of the standard technique results in a broadened profile, caused by the velocity distribution of the sample gas at the precise spatial location where the beams overlap. Therefore, the spatial resolution can be greatly improved over typical cell-length line integrated profiles, where the beam interacts with a line of gas throughout the whole length of the cell. Instead of losing resolution capability because of the Doppler effect, the hole burning technique exploits Doppler information to allow the measurement of either the naturally broadened hyperfine component lines, or the spatially-resolved Doppler-broadened profiles.

III. Experimental

A. General Setup

The primary laser source for the experiment was the Coherent 899 Ring Dye Laser, pumped by a 6 Watt Argon Ion laser at the 514-nm line. The ring laser was setup to operate using Rhodamine 590 dye, with an output beam that radiates in the 570-610 nm range. This range determined the spectral range available for the observation of absorption lines in molecular iodine. The specific transitions chosen were well in the center of this range, to allow for output power of at least 300 mW from the dye laser in single frequency.

The calibration of the wavemeter on the ring dye laser assembly was very important, as at times systematic alignment problems caused offsets of almost 0.2 cm^{-1} , a very significant frequency correction. A complete calibration procedure is offered in Appendix I, by using Doppler-free saturation measurements of hyperfine structure, and comparing measured center frequencies for the naturally-broadened lines to published values.

The ring dye laser was controlled by the manufacturer's autoscan program, which was used to stack scans and collect data. The program had the capability to run scans with various wavelength ranges, resolution, and data averaging algorithms. The lock-in amplifiers used were Stanford Research Systems SR850s. Chopping frequencies were set to 3800 rotations per minute (rpm's) to ensure that the chopping period would be smaller than the set lock-in amplifier time constants.

Two separate cell designs were used to contain the iodine gas: the first was an enclosed glass cell with one inch optical windows on each end, in which the true pressure

was unknown. The second was a stainless steel housing with a one-inch optical window fixed to one end and three ports for pressure control/measurement, and gas temperature determination at the other end. The experiment was actually designed in two phases, related to the cell design. Phase I experiments were conducted using the closed glass iodine cell, which was primarily utilized to obtain a rough understanding of the measurement technique, and to prove that a high enough signal to noise ratio (SNR) could be obtained for both Doppler-free and -limited saturation measurements. Phase II experiments involved the use of the stainless steel cell, in order to better control the pressure inside the cell and to allow for comparison to reference temperature measurements made by a thermocouple within the same cell under identical conditions

B. Phase I

The closed I_2 cell was first used to demonstrate that the technique would show enough merit to justify continued investigation. The optical table was first setup for Doppler-free saturation spectroscopy measurements, in order to find the hyperfine splittings within given transitions. The setup is shown in Figure 19. For this configuration, a pin diode (PD1) measured the laser power to ensure that fluctuations in power did not affect the absorption profile. The photomultiplier tube (PMT) measured the side fluorescence from the iodine cell, so that the broadened line could be superimposed with the hyperfine structure. PD2 was used to measure the intensity of the probe beam after it passed through the sample, essentially mapping out the hyperfine spectrum as the scan progressed.

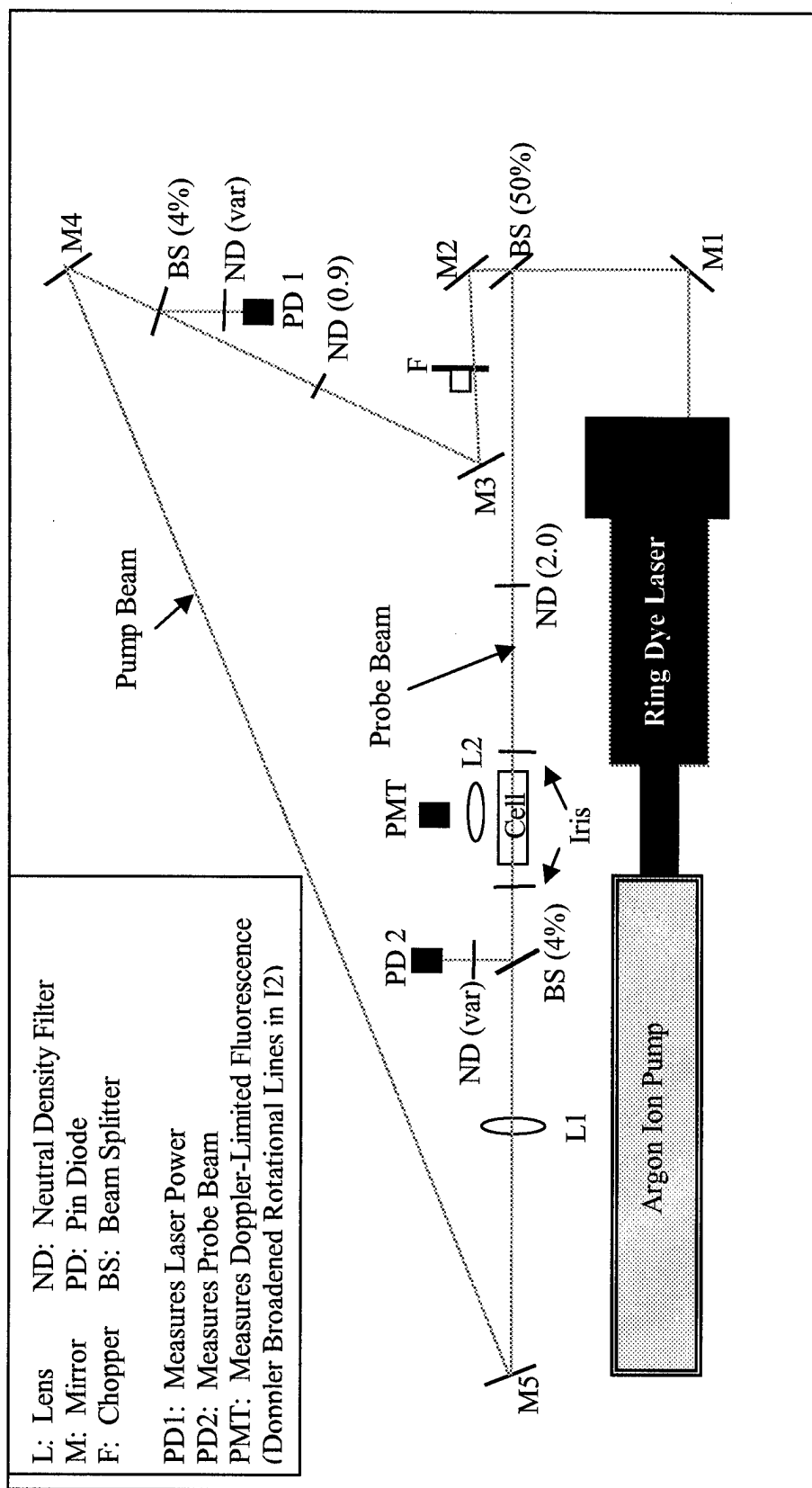


Figure 19. Experimental setup for Doppler-free measurements using the enclosed cell

One important thing to note about this setup is the fact that the beams were aligned to overlap completely throughout the iodine cell. The two adjustable irises ensured near-perfect overlap, since both beams were adjusted to go through both apertures, set at the same height and diameter. This allowed for very strong interaction with the 0 velocity gas molecules because the interaction volume was large.

The PMT measurements allowed for large scans of Doppler broadened lines at low resolution to be made, in order to find transitions that would be adequate to representatively demonstrate the technique. The first two lines were chosen based on their isolation in frequency space, while the other two were chosen because they consisted of overlapping lines. There was some thought at the inception of the experiment that overlapping lines might provide greater temperature sensitivity, which justifies the exploration of transitions that overlap. The line sets chosen were those centered at:

(a) $17249.9623 \text{ cm}^{-1}$

(b) $17339.8187 \text{ cm}^{-1}$

(c) $17340.2214 \text{ cm}^{-1}$

(d) $17340.7535 \text{ cm}^{-1}$

These lines had lineshapes that are shown in Figure 20. They are presented here to illustrate why these particular transitions were chosen. The x-axis on these diagrams is the frequency, in cm^{-1} and the y-axis represents relative intensity.

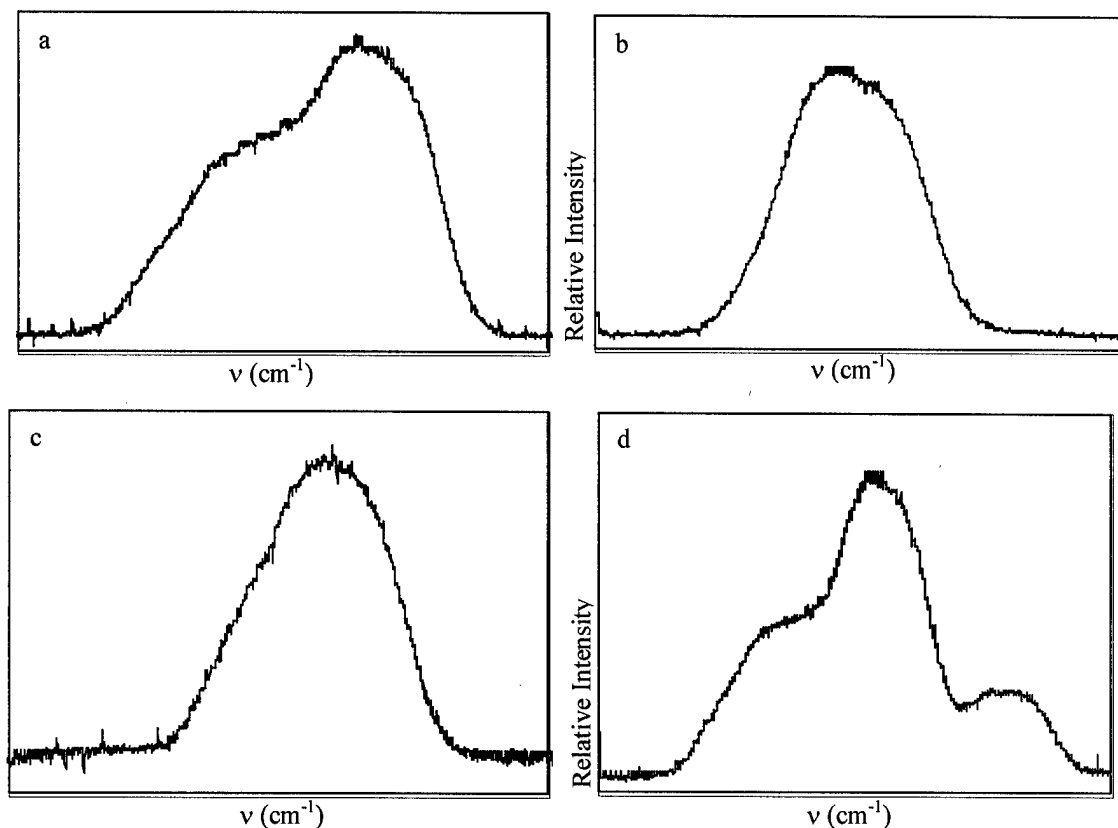


Figure 20. Broadened lineshapes for chosen line sets: a) $17249.9623 \text{ cm}^{-1}$, b) $17339.8187 \text{ cm}^{-1}$, c) $17340.2214 \text{ cm}^{-1}$, and d) $17340.7535 \text{ cm}^{-1}$.

The identification of these lines was determined by creating energy level difference tables, as described in Chapter II. The lines were attributed to the following transitions:

Table 2. Experimental line assignments

<u>$\nu_o (\text{cm}^{-1})$</u>	<u>Transition (s)</u>
17249.9632	P(66) 16-1, P(51) 18-2
17339.8187	P(70) 17-1
17340.2214	P(53) 19-2
17340.7535	P(122) 16-0, R(74) 17-1, R(57) 19-2

The letter designation P or R refers to the rotational branch for the transition in Table

2. The number in parenthesis is the J'' number, and the hyphenated number denotes

which vibrational level change occurred in conjunction with the transition between electronic levels ($v'-v''$). From this point forward in this document, these designations will be used when referring to specific line sets.

Once the lines were chosen, hyperfine measurements were made to uncover the Doppler-free splittings that composed the broadened lines. A scan was made across each of the transitions with the following scan parameters:

Scan width = 3 (GHz)

Scan interval = 1 (MHz)

Scan rate=600 (seconds/10 GHz)

The hyperfine spectra were recorded for the four transitions and the setup was changed to make Doppler-limited measurements of the same transitions. The two beam components were redirected to copropagate through the medium, crossing at a finite angle Θ . Figure 21 shows the Doppler-limited setup. The mirror (M2) which directed the pump beam through the medium was mounted on a translational stage, such that the lateral position at which the beams crossed in the cell could be changed, while leaving the angle the same. There was enough freedom to move the beam cross point from one end of the cell to the other.

To create a heat gradient in the cell, one end of the cell was wrapped with heater tape. The heater tape temperature was measured with a thermocouple, and was kept constant after equilibrium was reached at 250 degrees Celsius (523 K). With this cell, it was not possible to have thermocouple temperature measurements of the gas at various positions along the cell. The system was closed, so there was no reference temperature distribution available with which optical results could have been compared.

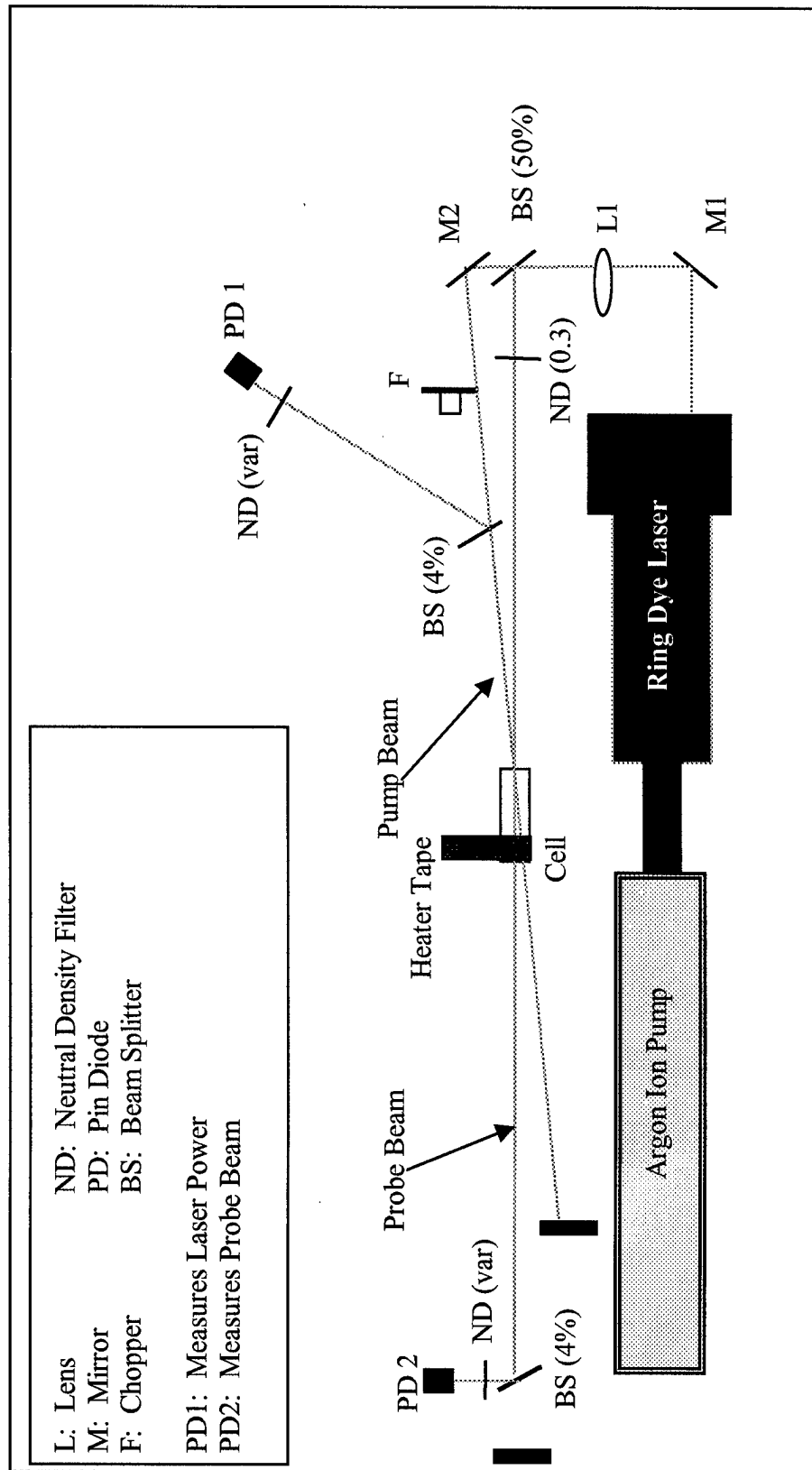


Figure 21. Experimental setup for Doppler-limited measurements using the enclosed cell

Profiles were measured at the 1-inch position, at the 3-inch position, and at the 5-inch position in the 6-inch glass cell. Figure 22 illustrates the cell length and the positions where the beams crossed for the Doppler limited scans.

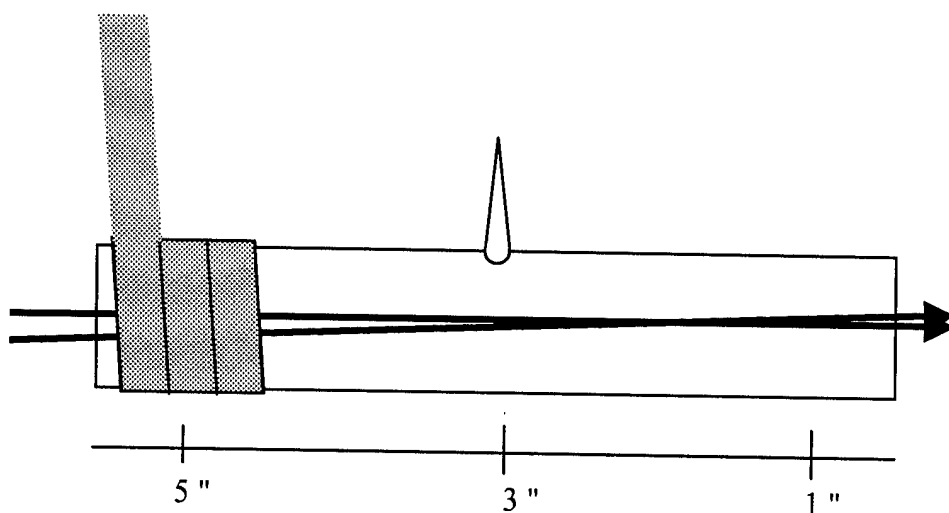


Figure 22. Cell crossing lengths (shaded region is heater tape) The beams as shown are copropagating for Doppler-limited measurements.

C. Phase II

After the data analysis was performed on the data from Phase I, it became clear that a new cell design was needed. It was imperative, first of all, to be able to control and measure the pressure in the cell, to avoid the possibility of pressure broadening, which could have added to the linewidths, creating a systematic error in temperature measurements. The second requirement for a new cell was to have the ability to measure the temperatures at positions along the cell in order to have a comparison standard for the Doppler limited optical scans.

For convenience the cell in Figure 23 was constructed out of a stainless steel housing, and an optical window was affixed with epoxy to one end of the cell. Three ports were

available at the other end of the cell. The two side ports were used for vacuum system hookup, and for the placement of an I_2 gas source cell. The back port was a dual-purpose port that would allow interchange of either a second window or a thermocouple fitting. The ports were all 1/2" in outer diameter, so that they could be fitted with vacuum-sealed Cajon fittings. The thermocouple fitting for the end port allowed a probe to be moved to any position along the center of the cell, while the window fitting allowed for the optical temperature measurements.

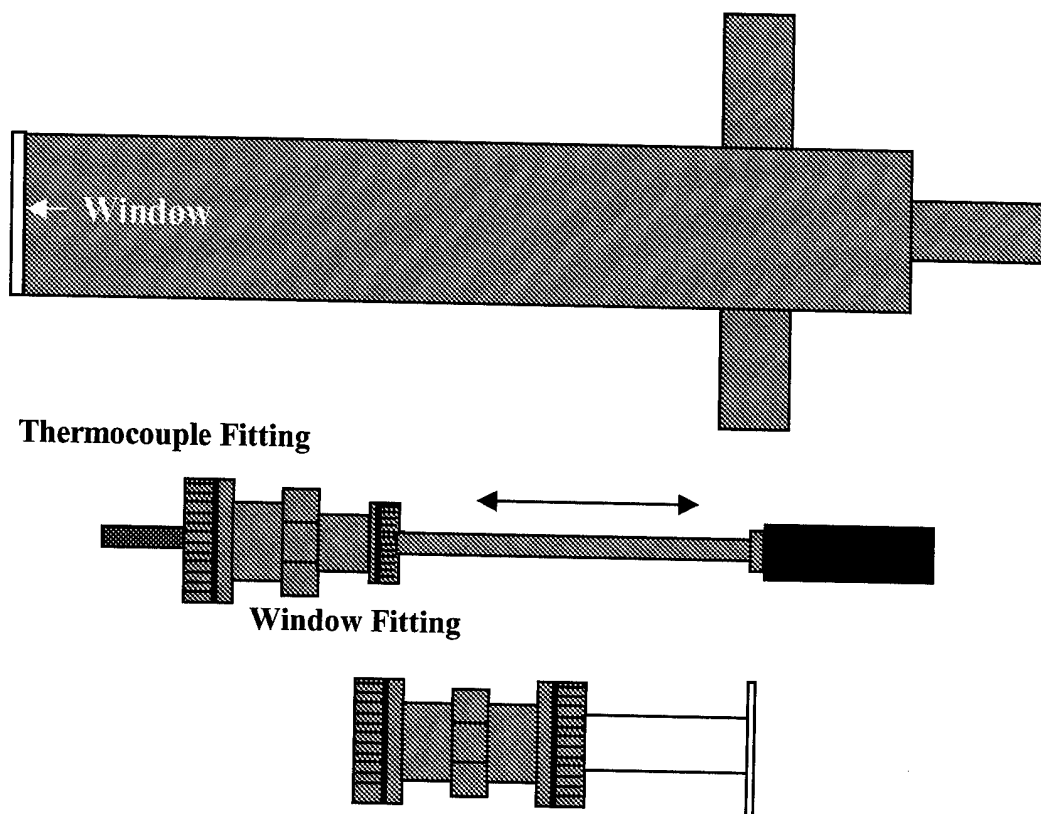


Figure 23. The open cell design. The thermocouple fitting allows a thermocouple to slide through the center of the cell, to measure the temperature at any axial point. The window fitting replaces the thermocouple fitting at the end of the cell, to allow for laser propagation and optical temperature measurements.

Care was taken in this phase of the experiment to make sure that the hyperfine measurements, the Doppler-broadened measurements, and the reference temperature measurements were conducted under as close to the same conditions as was possible. This included crossing angles, laser intensity, pressure, and relative amplitude ratios of pump intensity to probe intensity.

The first procedure was the temperature assessment using the thermocouple. Pressure was kept steady at 0.2 Torr \pm 0.002. This pressure is less than the vapor pressure of I_2 at room temperature by 0.08 Torr, so it is lower than the pressure could have been in the closed cell. The heater tape warmed the outside of the cell at 250 degrees while the cell was kept at vacuum. The gas valve was opened, left at pressure for at least 20 minutes to equilibrate, and measurements were taken at 1, 2, 3, and 4 inches along the cell length. The schematic for the thermocouple measurements is in Figure 24.

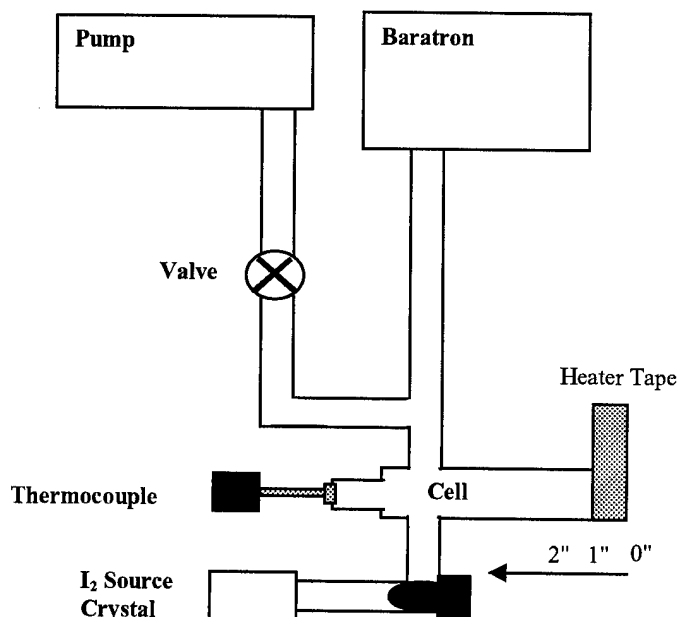


Figure 24. Reference temperature measurement setup. The thermocouple fitting was used, and temperatures were measured at 1, 2, 3, and 4 inch positions.

Instead of the four lines investigated in Phase I, only the two isolated lines, P(70) 17-1 and P(53) 19-2 were observed in Phase II. The P(70) 17-1 transition is composed of 15 hyperfine lines, while the P(53) 19-2 transition is composed of 21. Sampling these two lines accounted for all the possible hyperfine configurations for frequency-isolated lines in I₂. As will be shown in the next chapter, multiple line sets were difficult to use for precise temperature extraction, although there is still evidence that suggests overlapping lines may be more sensitive to small temperature variation.

For these two transitions, hyperfine measurements were made in the same manner as in Phase I. The only difference in the two setups, as is evident in Figure 25, is that with the open cell the beams do not completely overlap at a zero angle, but overlap at an angle $\Theta = 3.6$ degrees. This angle between the beams was necessary to keep conditions the same for Doppler free and Doppler limited measurements; if the beams overlapped through the entire cell length, then the Doppler limited spatially resolved measurements would be line-integrated averages, which is where this project started.

The next two pages show the setup diagrams, Figures 25 and 26, for both the Doppler-free and Doppler-limited experiments. Doppler-limited absorption spectra were obtained by crossing the beams at 1, 2, 3, and 4 inches, in order to compare the results with the thermocouple measurements. The scan parameters and cell settings were the same for both optical procedures, and are given in Table 3 below:

Table 3 Scan parameters and cell settings for Phase II

Laser Power (prior to splitting)	350 mW	Scan width	5 GHz
Heater Tape temperature	250° C	Scan interval	1 MHz
I ₂ pressure	0.2 Torr	Scan rate	600 s/10 GHz
Ratio of Probe/Pump Intensity	50%		

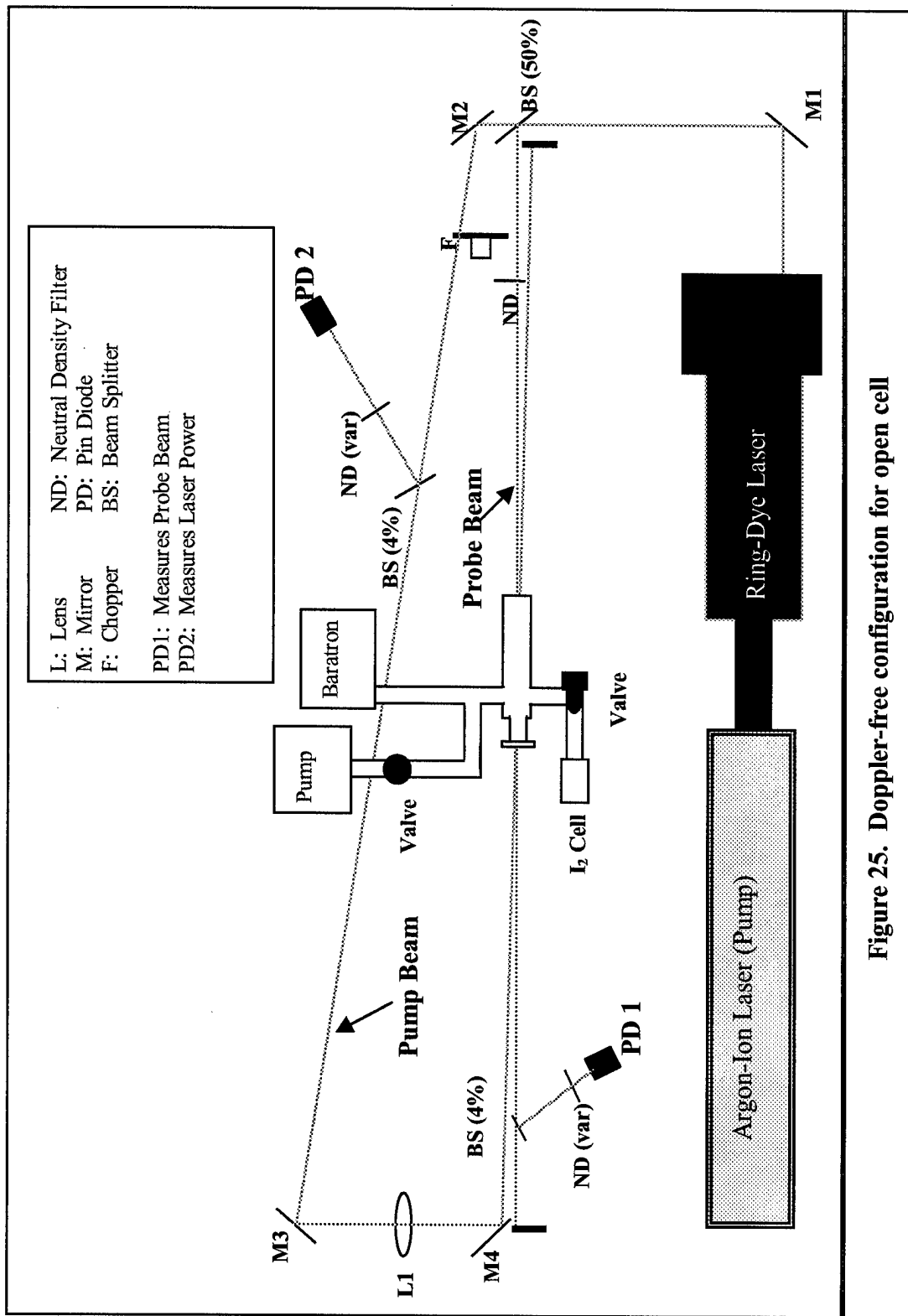


Figure 25. Doppler-free configuration for open cell

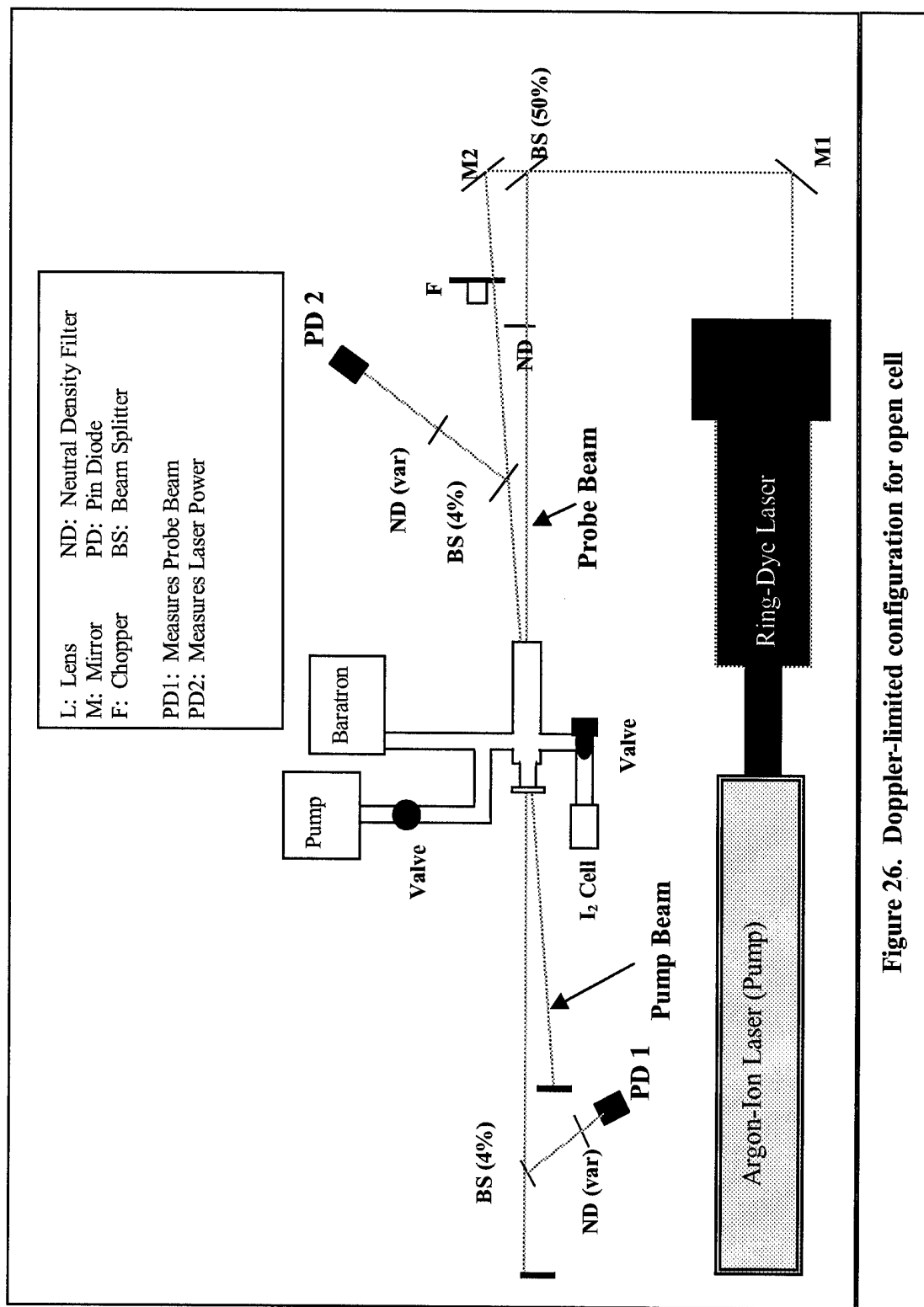


Figure 26. Doppler-limited configuration for open cell

D. Data Analysis Procedure

For each hyperfine spectrum measured, the data was transferred into ASCII format and imported into Peakfit version 4.0. Depending on the J'' value for the transition, as explained previously, 21 or 15 Lorentzian lines were used to fit the data. The user-modified Peakfit functional definition and settings for the Lorentzian hyperfine lines were:

$$y = a_3 \cdot \frac{a_0}{\left[1 + \left[\frac{x - (a_1 + a_4)}{a_2} \right]^2 \right]} \quad (19)$$

where

a_0 = line amplitude	Shared
a_1 = line center frequency	
a_2 = natural line width	Shared
a_3 = relative line amplitude	Locked
a_4 = center offset frequency	Shared

Locked values indicate that the user will define values for each peak; these values do not change during the fitting routine. The relative amplitudes were locked at the theoretical values, proportional to $2F + 1$, as outlined in Chapter II. Shared values indicate that the fit will proceed, ensuring that the values will be common among all the peaks. The center offset shifts all the lines by a shared amount to achieve the best fit, the widths are

necessarily are shared value because the lines are naturally broadened, and the overall amplitude factor simply raises or lowers all the peaks to match the relative amplitude of the data series.

The resulting fit then gave the individual locations and shared FWHM values of the hyperfine lines. The Doppler limited data for the same transition was then imported into Peakfit, and the information from the hyperfine scan was used to define the Doppler-broadened fit routine. For Phase I a simple Gaussian profile was assumed. The user-modified Gaussian functional and parameter settings for the Gaussian profile on Peakfit were:

$$y = a_3 \cdot a_0 \cdot e^{-\frac{1}{2} \left[\frac{x - (a_1 + a_4)}{a_2} \right]^2} \quad (20)$$

where

a0 = line amplitude	Shared	
a1 = line center frequency		Locked
a2 = Doppler width	Shared	
a3 = relative amplitude		Locked
a4 = center offset frequency	Shared	

For Phase II a Voigt Profile was used, so that the Lorentzian and Gaussian lineshapes could be individually locked or shared, as necessary for the fit. The modified Peakfit functional form for the Voigt Profile and its parameter setting were:

$$y = a_4 \cdot a_0 \cdot \int_{-\infty}^{\infty} \frac{e^{-t^2}}{\left(\frac{a_3^2}{2 \cdot a_2^2} \right) + \left[\frac{x - (a_1 + a_5)}{\sqrt{2} \cdot a_2} \right]^2} dt$$

(21)

where

a_0 = line amplitude	Shared	
a_1 = line center frequency		Locked
a_2 = Doppler width	Shared	
a_3 = natural line width	Shared	Locked
a_4 = relative amplitude		Locked
a_5 = center offset frequency	Shared	

The line centers and the Lorentzian widths were locked at the positions resulting from the hyperfine fit. The relative amplitudes remained locked at 2 F+1 proportions. The

remaining values were shared among the peaks for the fitting routine. The amplitudes, again, were shared to account for changes in the data intensity profile and the center offset compensated for uniform shifts in the frequency axis for the same line. The shared Gaussian width and its fit uncertainty were the primary factors for this work, since the Doppler effect defines the width of the Gaussian component. The resulting shared FWHM's for the Gaussian portions of the lineshapes were used to extract the temperature information, as described in the next chapter. For all cases, the fitting routines considered all lines simultaneously, and used a linear baseline subtraction.

Signal to Noise Ratios (SNRs) were determined for both Doppler-limited and Doppler-free data by taking the mean peak signal level divided by the rms deviation of the noise around the mean baseline. For this reason, when SNRs are recorded in this document, they will be accompanied by the mean baseline level, as well.

IV. Results

A. Phase I

The hyperfine spectra for the four transition sets-- P(70) 17-1, P(53) 19-2, the triply overlapped P(122) 16-0, R(74) 17-1, R(57) 19-2 states, and the overlapped P(66) 16-1, P(51) 18-2 states-- are shown in Figures 27-30. The figures show the component hyperfine structures behind the broadened transitions that were shown in Figure 20, measured by Doppler-free saturation spectroscopy for the closed glass cell. These spectra are representative of the Phase I hyperfine measurements, which were repeated several times for each transition under varying setup conditions to try to obtain a good peak SNR for each transition. With the almost total beam overlap in this configuration, the interaction volume was very large within the cell, about 120 mm^3 ($120 \times 1 \times 1 \text{ mm}$). Therefore decent signal/noise levels were not difficult to achieve, and are recorded in the figure captions.

The hyperfine patterns for the isolated transitions, P(70) 17-1 and P(53) 19-2, have patterns of 15 and 21 hyperfine lines, respectively, that match those of Figures 8 and 9. Since these are the only two possibilities for I_2 transitions, these lines are representative transitions for the purpose of this experiment and will provide a complete data set. The transitions that overlap with each other may in the end provide greater sensitivity to temperature changes, but complications to be discussed later arise when trying to fit the relative intensities of the overlapped lines.

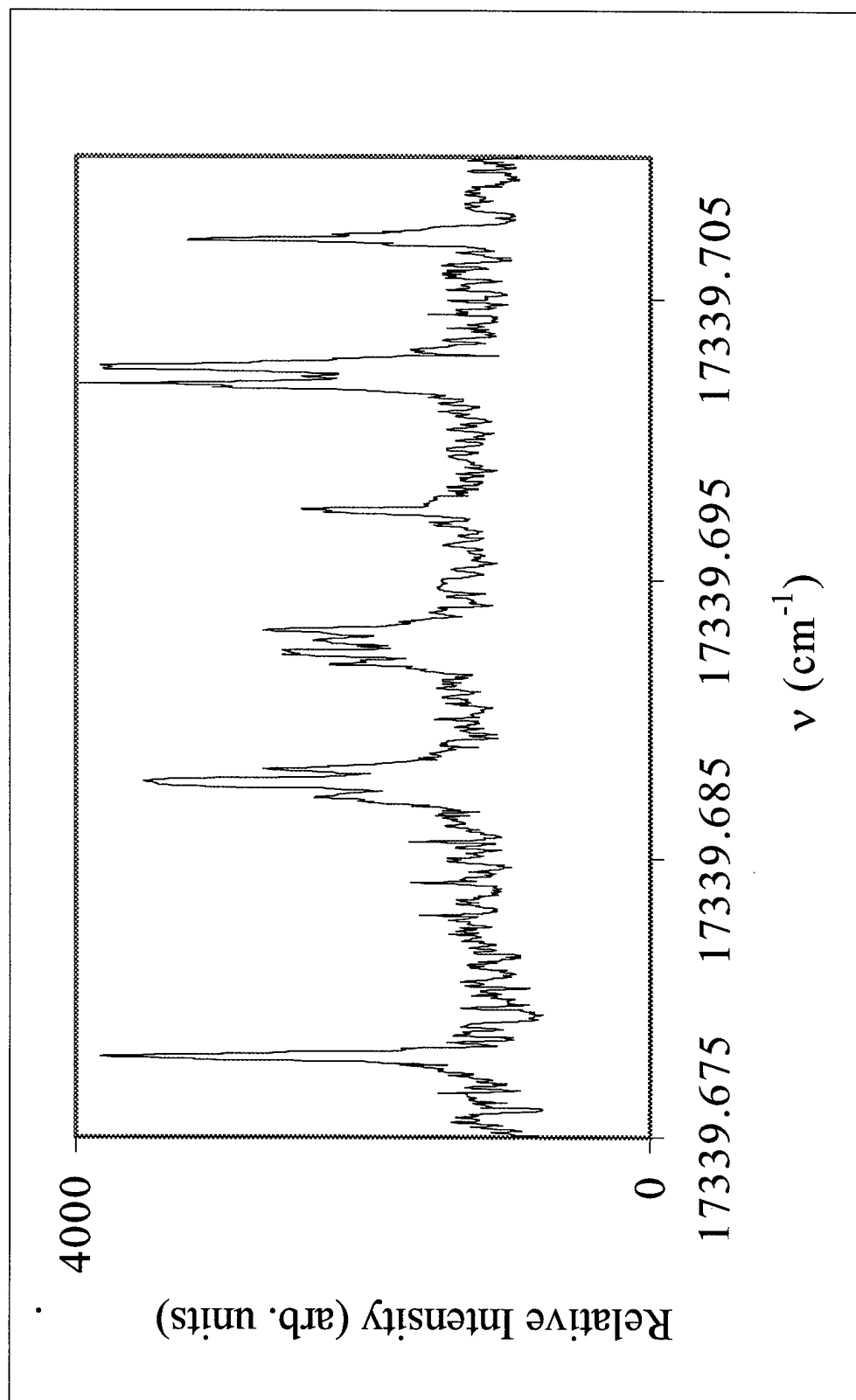


Figure 27. Hyperfine spectrum for P(70) 17-1. There are 15 hyperfine lines that comprise this transition. Peak SNR=18.68, mean baseline = 920.0 +/- 212.5.

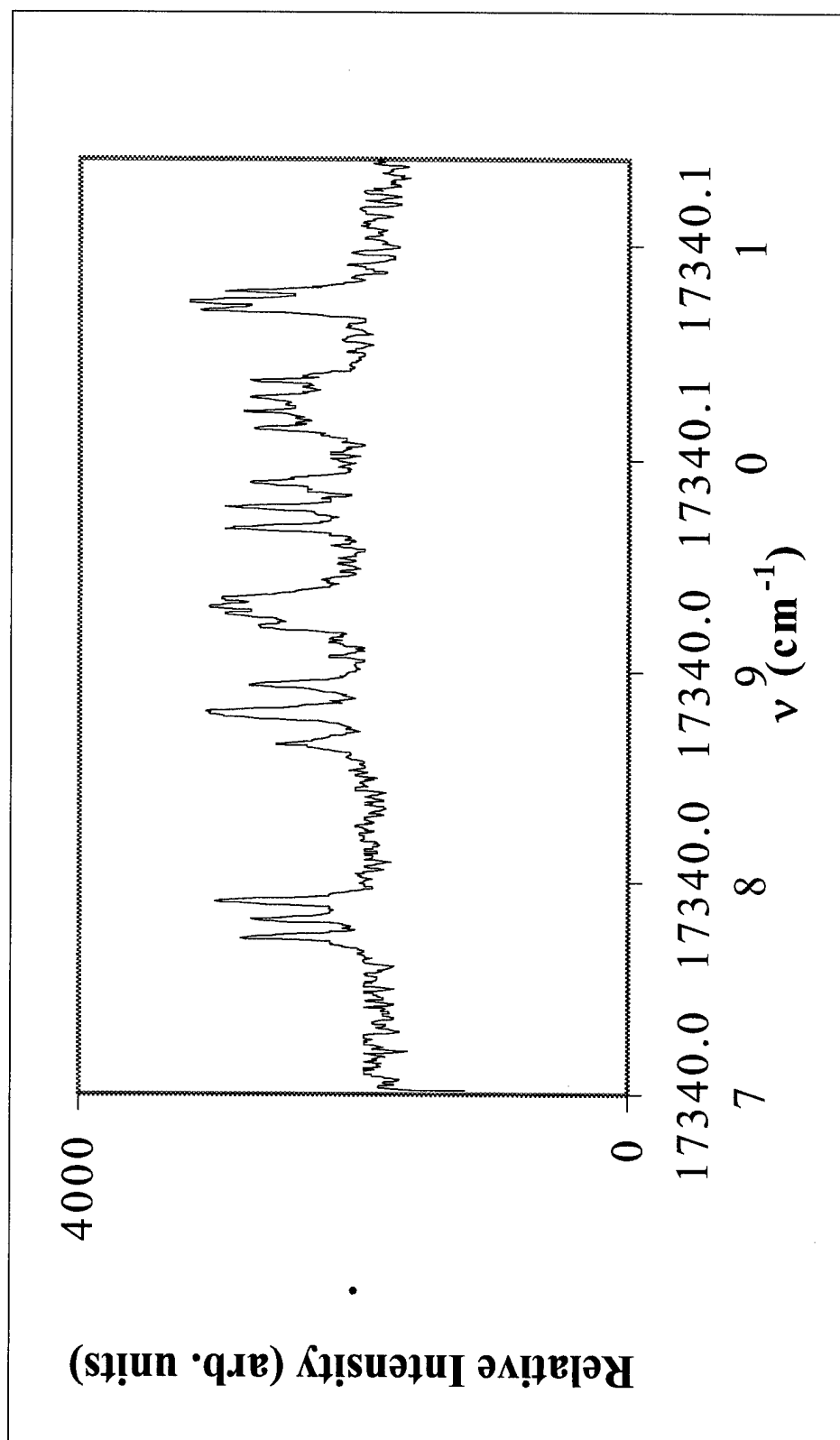


Figure 28. Hyperfine spectrum for P(53) 19-2. There are 21 hyperfine lines that comprise this transition. Peak SNR=69.6, mean baseline = 1986 \pm 46.24.

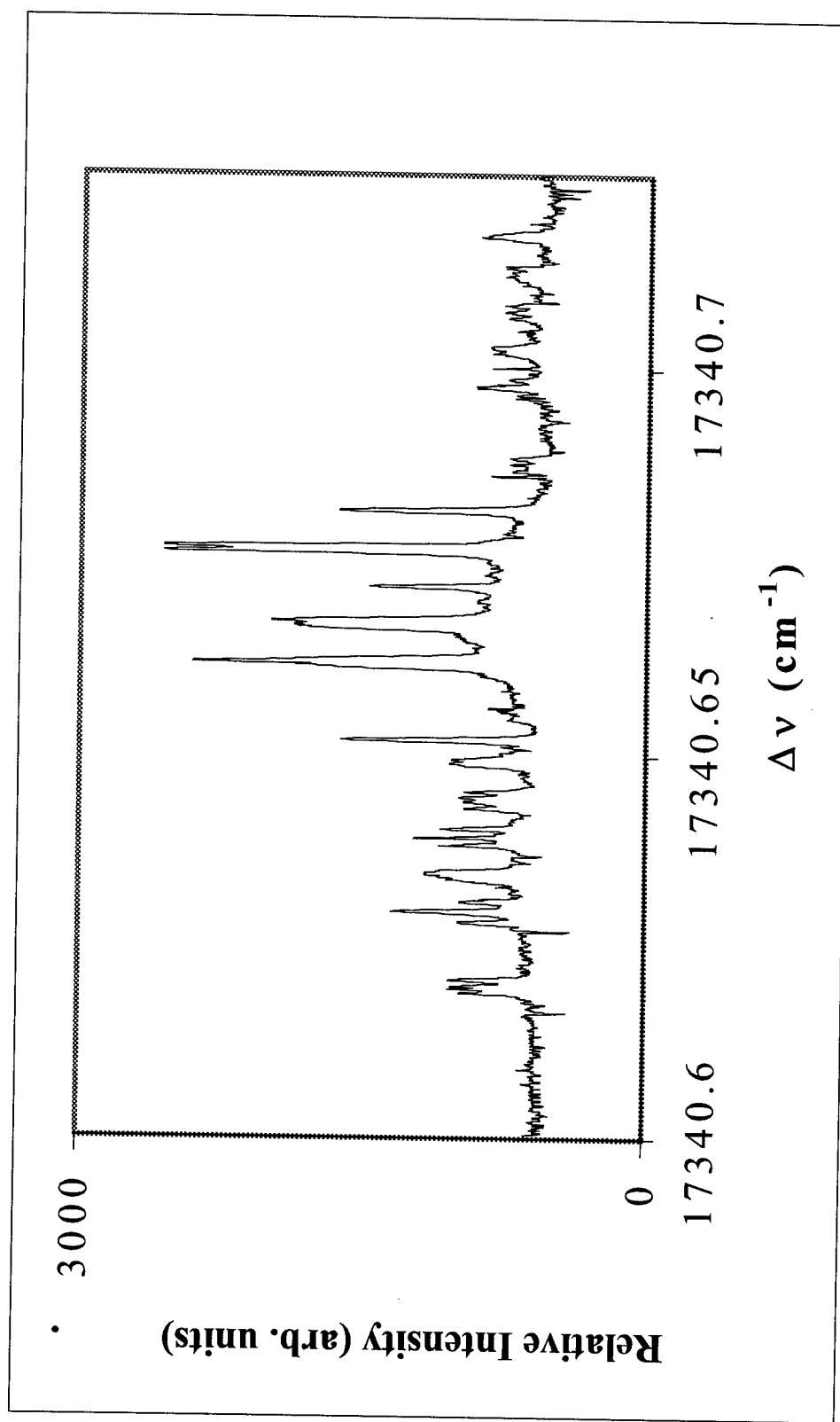


Figure 29. Hyperfine spectrum for P(122) 16-0, R(74) 17-1, R(57) 19-2. There are 3 overlapping lines that comprise this set; two of the lines have 15 hyperfine components, and one has 21 hyperfine components. Peak SNR=85.4, mean baseline = 575.9 \pm 29.3.

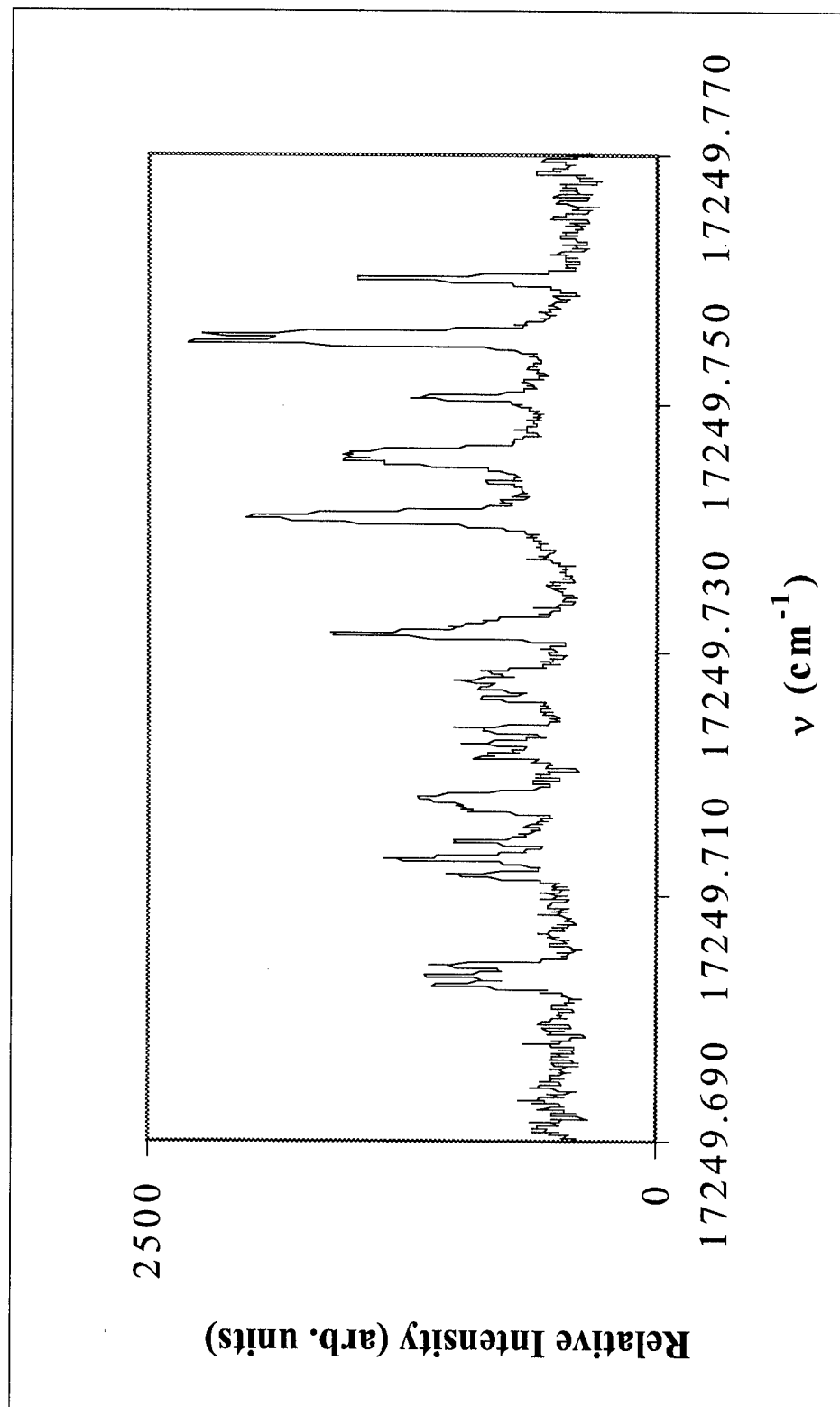


Figure 30. Hyperfine spectrum for P(66) 16-1, P(51) 18-2. There are 2 overlapping lines that comprise this set; one of the lines has 15 hyperfine components, and one has 21 hyperfine components. Peak SNR=36.7, mean baseline = 518 \pm 60.6.

The Doppler-limited spectral data for the four transitions, measured at different points along the non-uniformly heated cell are shown on the following pages. For these measurements the Doppler-limited setup in Figure 21 was followed using the closed glass cell. The absorption curves for the three different temperature points are superimposed on the same plots to illustrate the differences between the three temperature profiles. It was necessary to normalize the curves, since the hot end of the cell had a lower number density of iodine molecules than the cold end, according to the ideal gas law. Pressure and volume in the closed cell were fixed, so there was a tradeoff between temperature and number density, which decreased the absorption at the hot end.

Figures 31-34 are presented here to show that the Doppler-limited saturation spectroscopy technique does satisfy the condition for spatial resolution. The fact that these profiles exist demonstrates that the absorption profiles are spatially resolved. The CW probe beam could not contribute absorption information to the lock-in signal if it were not interacting with the same spatial volume of the gas as the modulated pump beam.

Line-integrated measurements within the same cell configuration have an interaction volume that can be approximated by that of a cylindrical beam with a 1mm radius interacting through the entire cell length. The development in Appendix B provides an approximation for the interaction volume for beams crossing at an angle $\Theta=3.8$ degrees. The line integrated volume was approximately $V_{LI} = 120 \text{ mm}^3$, while the volume for the spatially-resolved Doppler-limited measurements was $V_{SR}=12 \text{ mm}^3$.

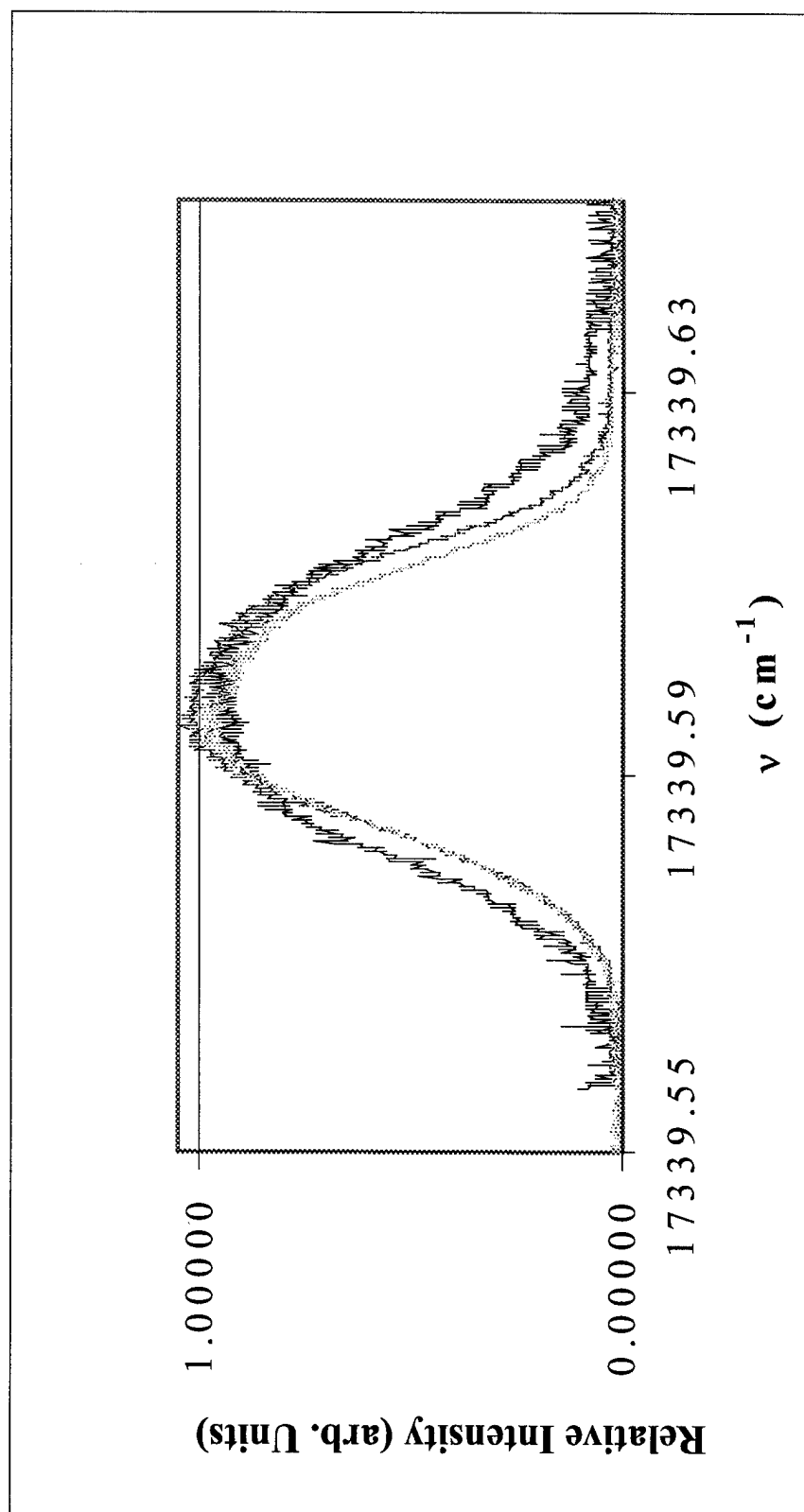


Figure 31. Absorption profile for P(70)17-1 for I₂ at 3 Separate Temperatures. The lightest shade indicates the lowest temperature; increasing darkness means increasing temperature. The highest and widest curve is the hot end measurement.

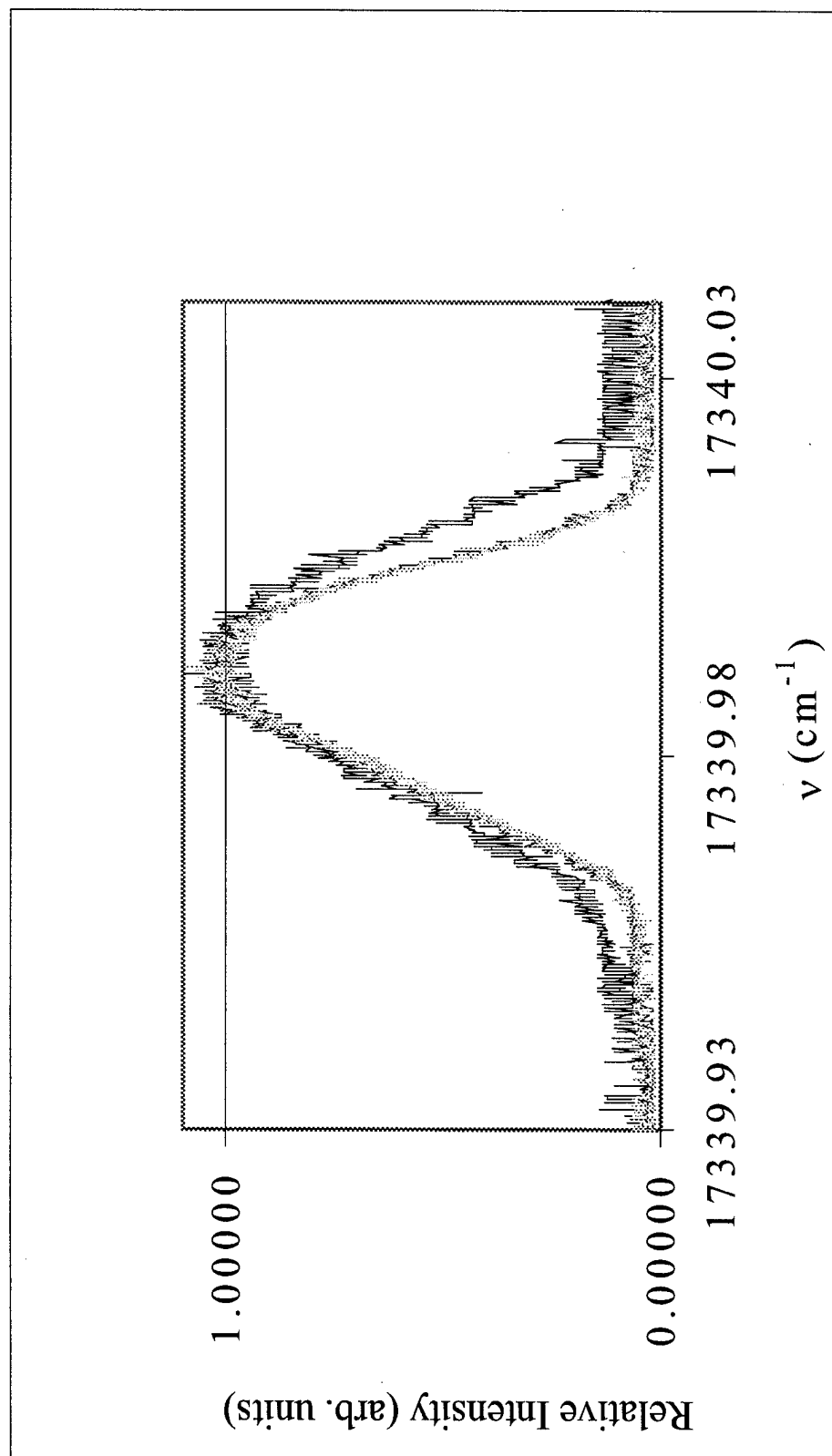


Figure 32. Absorption profile for P(53)19-2 for I₂ at 3 Separate Temperatures. The lightest shade indicates the lowest temperature; increasing darkness means increasing temperature. The highest and widest curve is the hot end measurement.

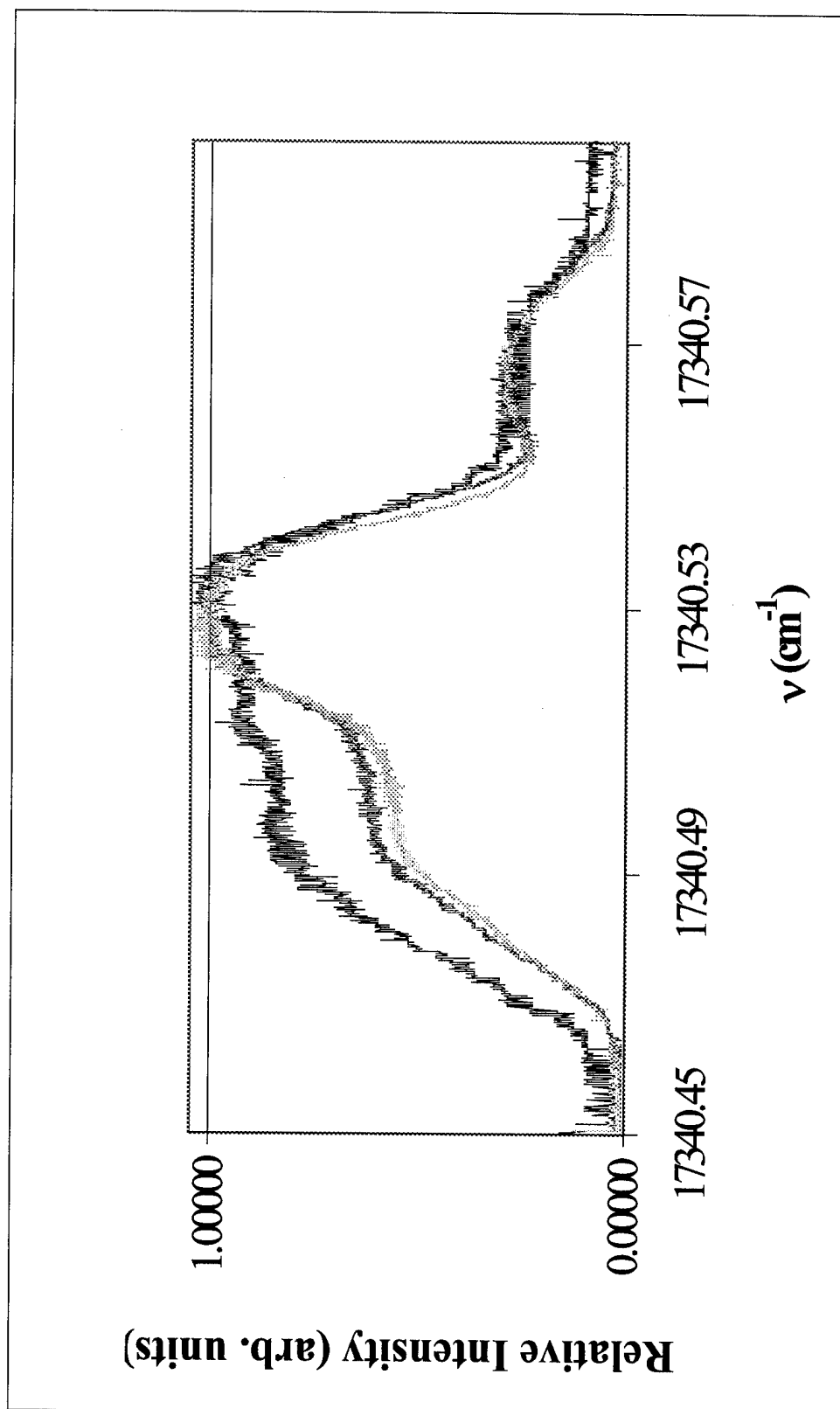


Figure 33. Absorption profile for P(122) 16-0, R(74) 17-1, R(57) 19-2 for I_2 at 3 Separate Temperatures. The lightest shade indicates the lowest temperature; increasing darkness means increasing temperature. The highest and widest curve is the hot end measurement.

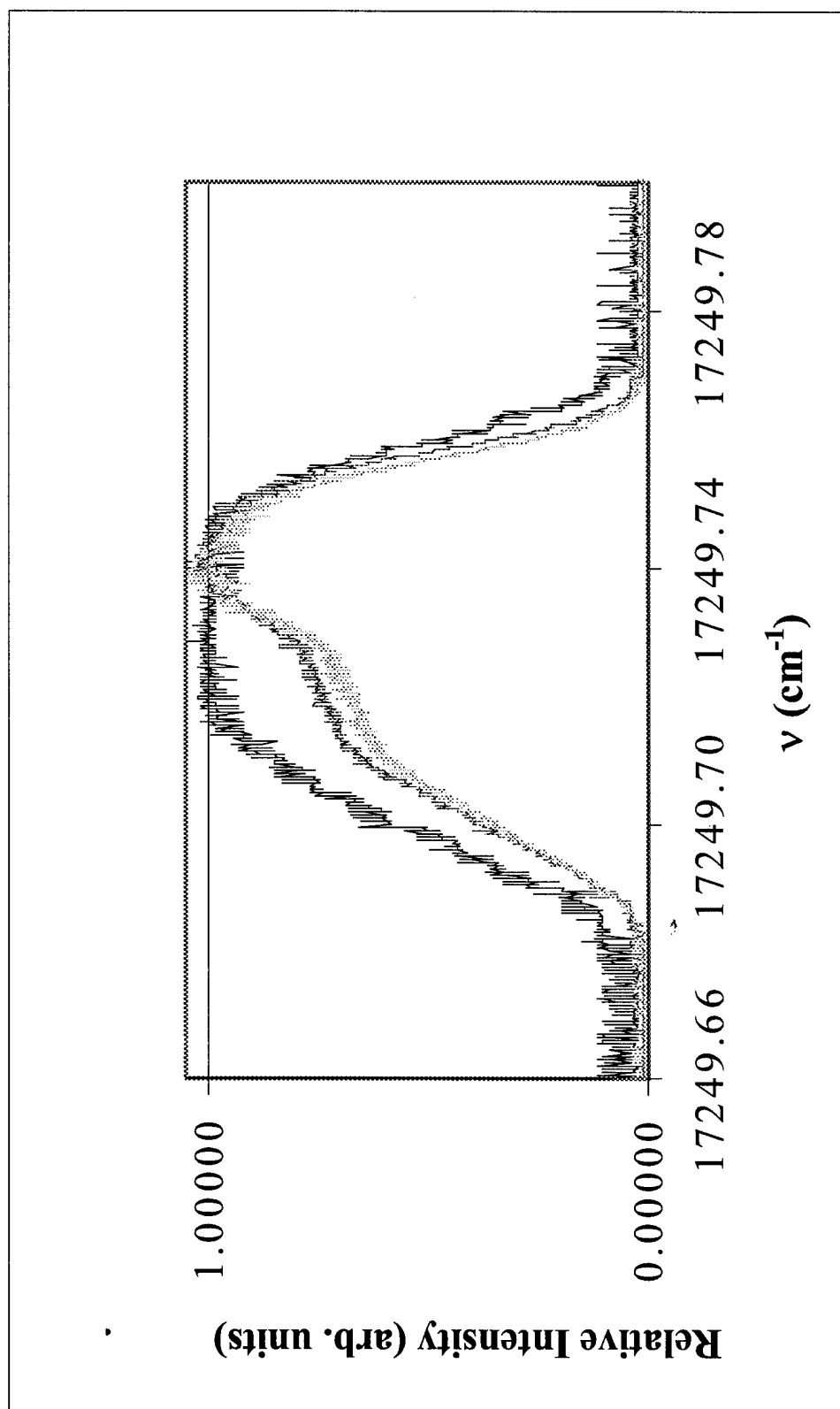


Figure 34. Absorption profile for P(66) 16-1, P(51) 18-2 for I₂ at 3 Separate Temperatures. The lightest shade indicates the lowest temperature; increasing darkness means increasing temperature. The highest and widest curve is the hot end measurement.

Though the main objective for the Phase I experiments was to prove the spatial resolution of the measured absorption transitions, it is encouraging to note the dramatic differences in the profiles due to temperature variation, especially for the overlapping lines. The isolated lines at higher temperatures, as expected from Figure 10, broaden into a more symmetrical Gaussian-type curve. The profiles for overlapping transitions tend to flatten out for the hotter temperatures, giving credence to the notion that these line sets may provide better temperature resolution than the isolates lines.

In reference to the Peakfit functions that are defined in Chapter III, Equations 19, 20, and 21, the relative amplitudes for the hyperfine lines are set and locked to their theoretical values based on the proportion $2F + 1$. This proportionality factor, however, only relates the amplitudes of the hyperfine lines within the same transition. For the overlapping transitions, the relative heights can then be set for each transition individually. The ratio of intensity from one transition to another is a completely different story, and does not involve a simple linear relation.

The relative amplitudes for two different transitions are temperature dependent, as hotter temperatures cause the increased population of higher ro-vibrational states, changing the transition rates²³. In addition, the intensities may have a nonlinear response to incident radiation intensity, such that the amount of incident light energy affects each transition differently. This would mean that the intensities from one transition to the next would not be proportional to the theoretical intensities, as they would depend upon the laser intensity. Being a nonlinear phenomenon, the prediction of overlapping line intensities for a given experimental setup would be a nontrivial task. This nonlinear

response could possibly be temperature dependent, as well, further complicating the issue of accurate temperature extraction using hyperfine structure for overlapping lines.

The overlapping transitions therefore comprise a very complicated system for temperature extraction purposes. Though not satisfying, the overlapping transitions are presented in the previous figures merely as a qualitative illustration. The two lines which will be analyzed for the quantitative extraction of temperature information are those which are isolated in frequency space: P(70) 17-1 and P(53) 19-2. As previously stated, these two transitions are representative of all possible I_2 transitions.

The hyperfine fit for the P(70) 17-1 transition is shown in Figure 35, with the corresponding fit parameters given in Tables 4 and 5.

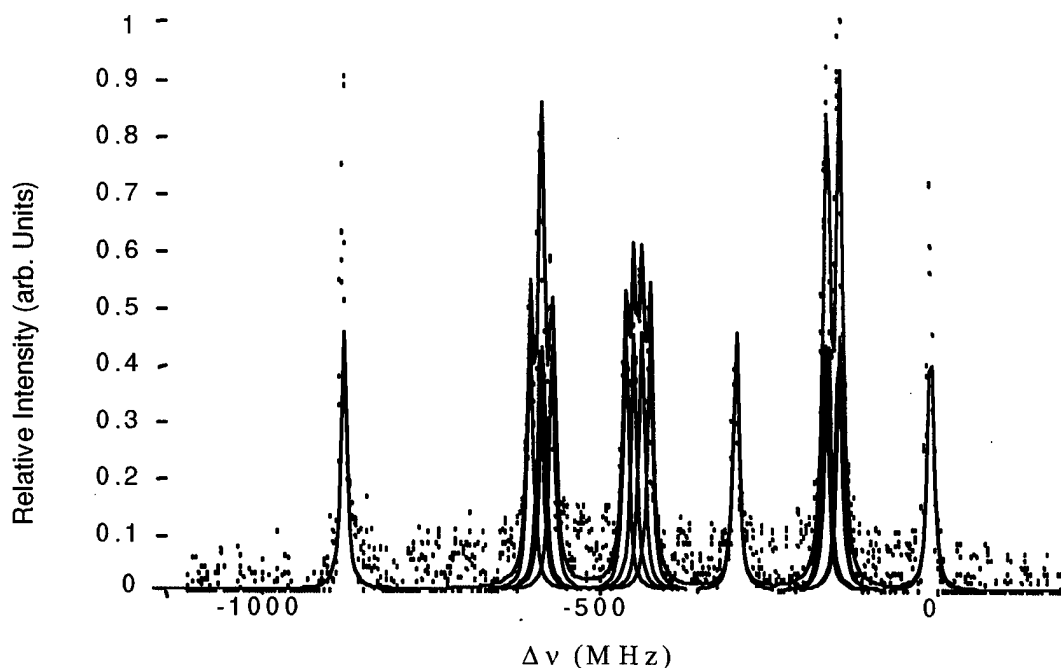


Figure 35. Hyperfine fit plot for P(70) 17-1. This is the same spectrum in Figure 27.

Table 4. P(70) 17-1 hyperfine fit parameters

Peak	Center (MHz)	FWHM (MHz)
1	-883.39	9.94
2	-606.23	
3	-591.76	SNR
4	-587.78	18.68
5	-573.63	
6	-463.83	r-squared
7	-451.97	0.876
8	-440.24	
9	-427.84	
10	-299.75	
11	-167.79	
12	-163.80	
13	-147.57	
14	-145.28	
15	-11.26	

The resultant value for the hyperfine linewidth, 9.94 MHz, is on the order of the expected natural linewidth. A signal to noise ratio of 18.64 is adequate to differentiate the hyperfine lines from the noise floor. The r-squared value should be unity for an ideal fit; the poor value comes from the fact that the addition of the hyperfine lines do not account for the baseline. In the figure, it is also evident that the theoretical intensities do not seem to account for the two hyperfine lines at the ends of the spectrum; this will be discussed further in the next chapter.

The line positions in Table 4 were used to set the centers of the 15 Gaussian components to fit the Doppler-limited data. Figures 36-38 show the Doppler-limited scans and their accompanying fit curves. The hyperfine Gaussian curves are shown at the base of the curves, each with a shared Doppler width chosen by the fit routine. The superposition of these curves accounts for the solid line, which ideally should match the trend in the empirical data points.

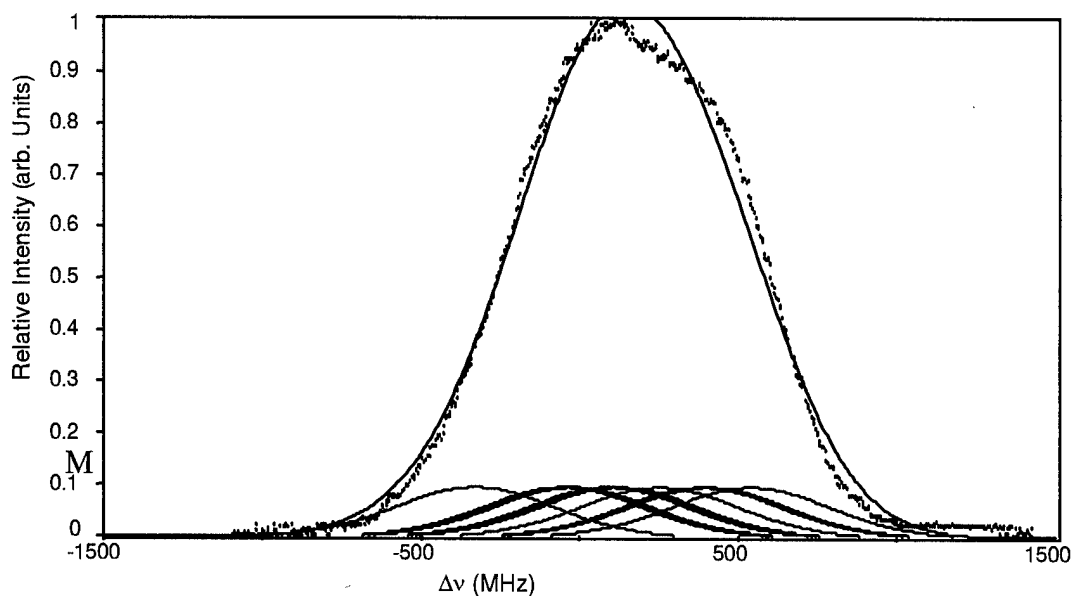


Figure 36. P(70) 17-1 Doppler-broadened transition at the cold end of the Phase I cell, measured by Doppler-limited saturation spectroscopy. SNR=122.5, mean baseline=18.5 \pm 13.6, $R^2=0.993$, FWHM=581 MHz, Extracted Temperature=615 K

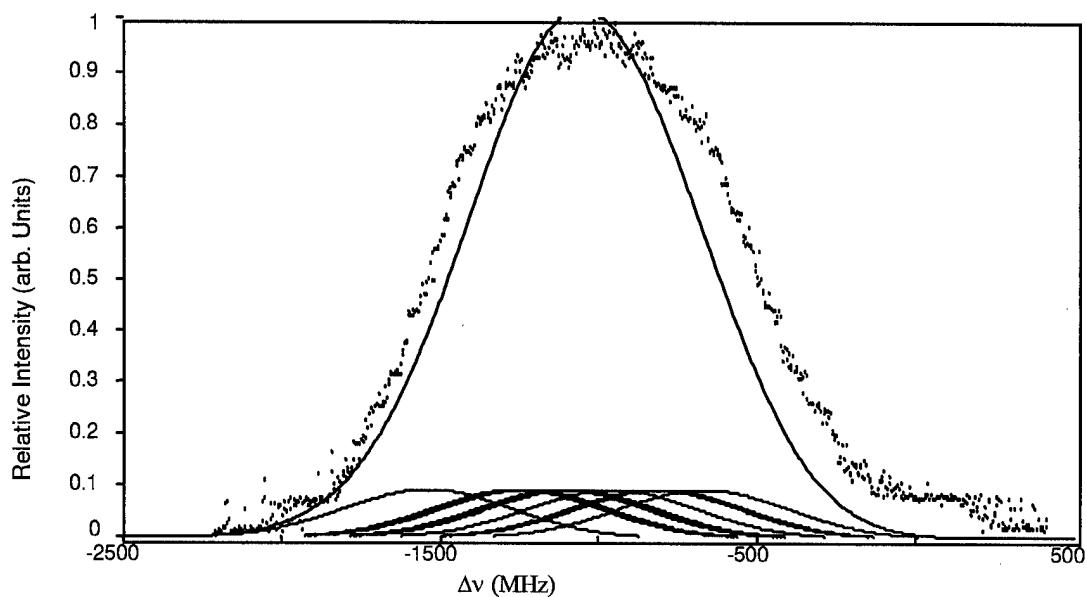


Figure 37. P(70) 17-1 Doppler-broadened transition at the warm center of the Phase I cell, measured using Doppler-limited saturation spectroscopy. SNR=102.8, mean baseline=24.0 \pm 13.8, $R^2=0.986$, FWHM =621 MHz, Extracted Temperature=707 K

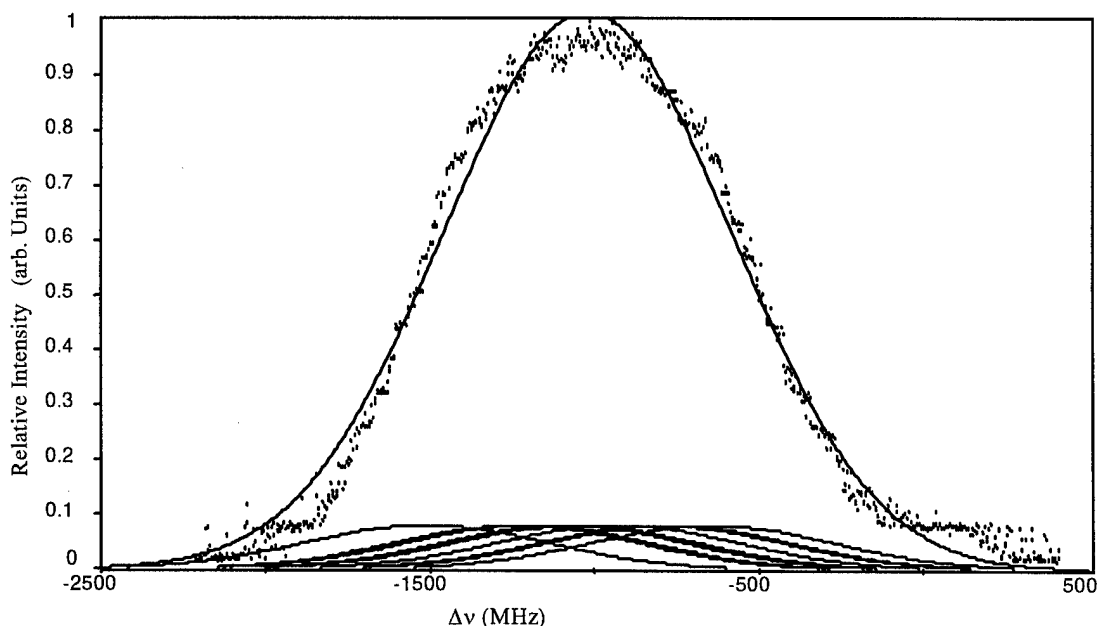


Figure 38. P(70) 17-1 Doppler-broadened transition at the hot end of the Phase I cell, measured using Doppler-limited saturation spectroscopy. SNR=37.5, mean baseline=22.4 +/- 13.7, $R^2=0.987$, FWHM=867 MHz, Extracted Temperature=1377 K

Table 5. P(70) 17-1 data summary table

<i>Temperature Position</i>	<i>SNR</i>	<i>R^2</i>	<i>FWHM (MHz)</i>	<i>Extracted Temperature (K)</i>
Cold End	122.5	0.993	581	615
Warm Center	102.8	0.916	621	707
Hot End	37.5	0.987	867	1377

These temperatures are much higher than what one would expect. The heater tape itself did not exceed 523 K, as measured on the cell surface, so the lowest optically-extracted temperature is higher than the heat source. Looking at Figures 36-38, it seems that the fit curves do not adequately represent the data. In all three measurements, the

parameterized fit tried to make the curve wider and higher than the data suggests, resulting in higher temperatures.

Because the cause of the obvious error in the optical measurement was unknown, the first step in diagnosing the problem was to make sure this anomaly was not transition dependent. The same procedures were completed, and the same data collected, for the P(53) 19-2 transition. Figure 39 shows the Lorentzian fit to the hyperfine spectrum for this transition, and Table 6 summarizes the main fit parameters.

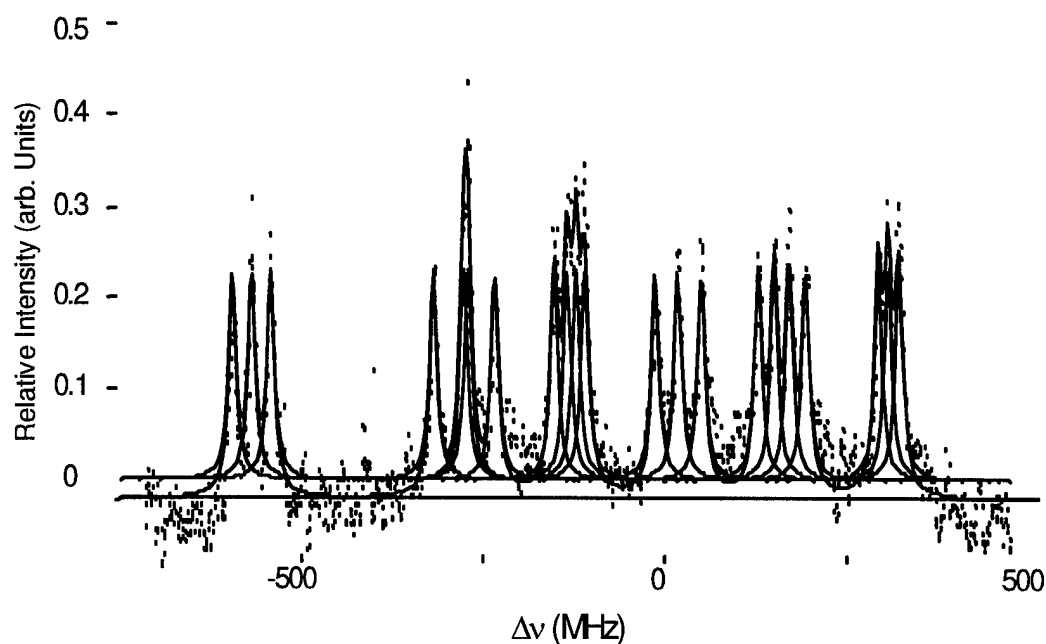


Figure 39. Hyperfine fit plot for P(53) 19-2. This is the same spectrum shown in Figure 28.

Table 6. P(53) 19-2 Hyperfine Fit Parameters

Peak	Center (MHz)	FWHM (MHz)
1	-604.25616	12.28
2	-577.94301	
3	-551.50746	SNR
4	-327.7671	69.6
5	-286.06186	
6	-280.08122	r-squared
7	-243.2564	0.895
8	-161.52815	
9	-143.76219	
10	-131.69411	
11	-119.66207	
12	-23.136483	
13	8.0834123	
14	40.313806	
15	118.02845	
16	140.06365	
17	160.64754	
18	182.87031	
19	281.94833	
20	295.39243	
21	310.31341	

The FWHM, though slightly higher than that of the P(17)17-1 transition, is still on the same order of magnitude for naturally broadened lines. Again, the poor r-squared value stems from the fact that the addition of the hyperfine lines does not account for the baseline, even though SNR is greater than in the last case. The details of the Doppler limited analysis for P(53) 19-2 are provided in Appendix C. Table 7 gives the summary of the data for this transition.

Table 7. P(53) 19-2 data summary table

<i>Temperature Position</i>	<i>SNR</i>	<i>R²</i>	<i>FWHM (MHz)</i>	<i>Extracted Temperature (K)</i>
Cold End	53	0.997	422	326
Warm Center	51.2	0.998	441	356
Hot End	34.0	0.989	775	1102

In this case, the warm center and cold end measurements are more reasonable, but the hot end temperature is still a nonphysical result. No conclusions can be drawn at this point as to what is causing the discrepancy. It also does not make sense at this point to discuss the standard deviation calculated from the fit. The Phase II measurements were meant to eliminate obvious systematic errors in order to narrow the possible sources for the erroneous temperature measurement. Phase II experiments allowed:

- 1) Pressure control and measurement in the cell
- 2) Identical conditions for the Doppler-free and -limited measurement configurations
- 3) Knowledge of the gas temperature at the measurement points along the cell
- 4) Use of a Voigt Profile to fit the broadened lines

In essence, the systematic errors had to be eliminated to ensure that the discrepancy in the temperature was not due to an obvious experimental flaw.

B. Phase II

The first data collected in Phase II was the temperature distribution for a known pressure of gas at the measurement positions in the new cell. The thermocouple was moved to each new position and was allowed to equilibrate at pressure for twenty minutes before the next measurement was taken. The resulting temperature profile within the cell is shown in Figure 43, and is presented in Table 8.

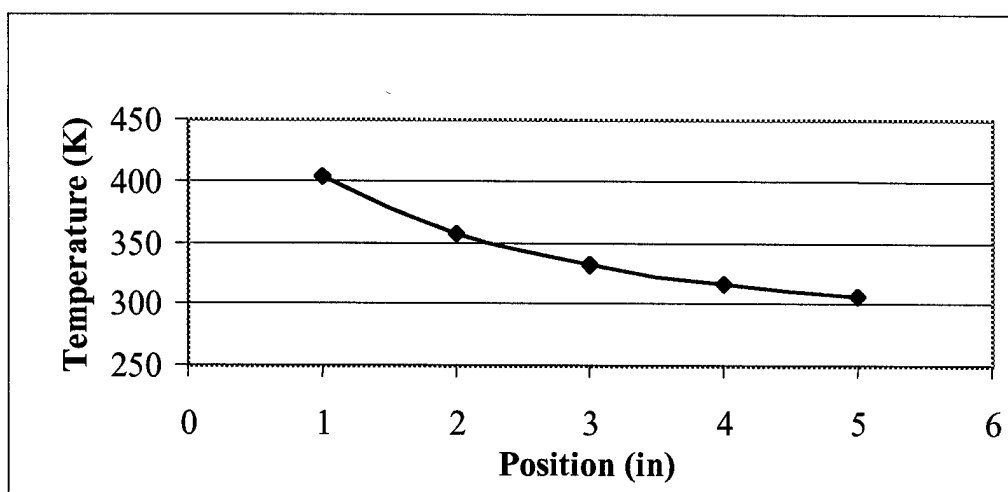


Figure 40. Spatial temperature profile for the cell

Table 8. Reference temperature values at each measurement point

Position (In)	Temp (C)	Temp (K)
5	33.3	306.3
4	43.4	316.4
3	57.8	330.8
2	84.2	357.2
1	130.3	403.3

The figures and tables that follow summarize the data analysis for Phase II. The analysis was the same as for Phase I measurements, except that measurements were taken at four temperature points. The hyperfine spectra were measured using the setup diagram from Figure 25 and are presented below in Figures 41 and 42.

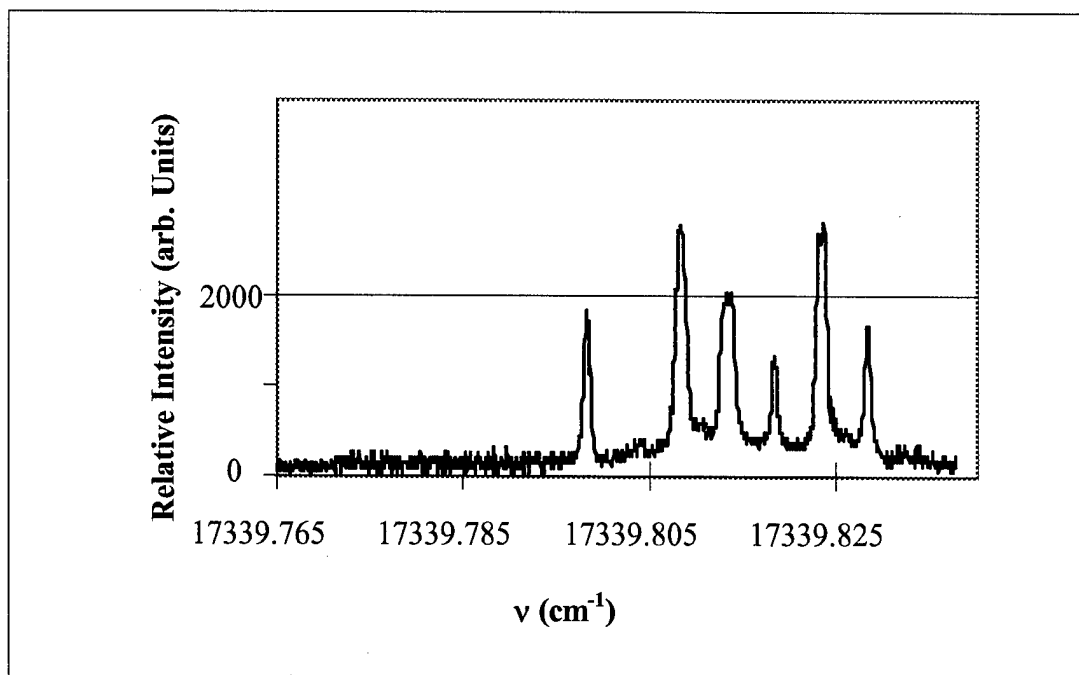


Figure 41. P(70) 17-1 hyperfine structure. Doppler-free measurement taken with the following parameters: ND=0.3 in the probe beam; Pressure=0.2 mm Hg; Lock-in sensitivity=500 μ V; Lock-in time constant=30 ms; SNR=55.24; mean baseline=169.7 \pm 50.7

This is a larger scan in frequency than was completed in Phase I. The longer scan shows that the hyperfine lines have widths that add to produce a residual broadened lineshape at the base of the hyperfine scan. This trend is noticed in other published documents concerning the employment of Doppler-free techniques to measure hyperfine interactions.^{10,25} The partitioning of data for Phase I partially masked this trend, which may account for the fact that the natural linewidths that were fit in Phase I were smaller than those in Phase II.

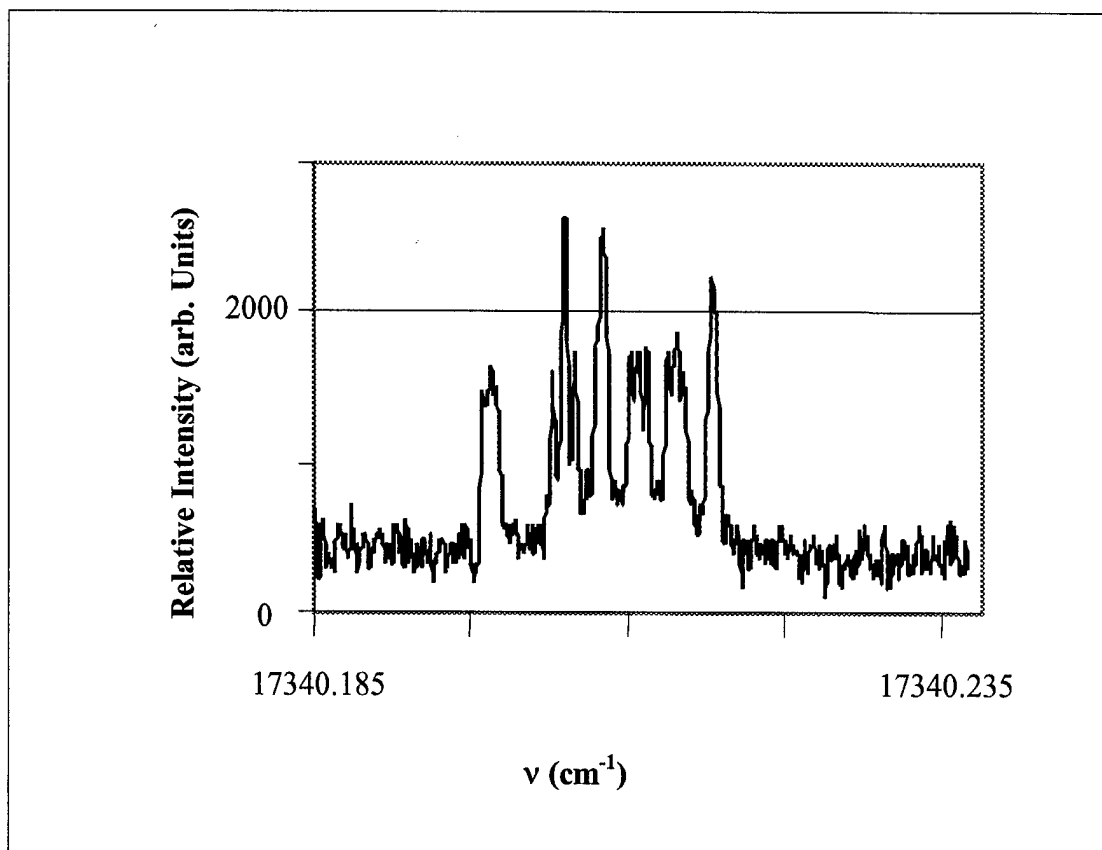


Figure 42. P(53) 19-2 hyperfine structure. Doppler-free measurement taken with the following parameters: ND=0.3 in the probe beam; Pressure=0.2 mm Hg; Lock-in sensitivity=100 μ V; Lock-in time constant=100 ms; SNR=13.9; mean baseline=471 \pm 179.9

The same trend is noted in this spectrum, where the higher energy lines all tend to have base widths that add to form a residual broadened lineshape. It is not clear what could be causing this trend. It could be simply that the natural linewidths are broad enough to add together at the base, or that some other broadening mechanism is acting on the transition; some of these issues will be addressed in the next chapter. Figure 43 shows the hyperfine fit for P(70) 17-1, with relevant parameters listed in Table 9.

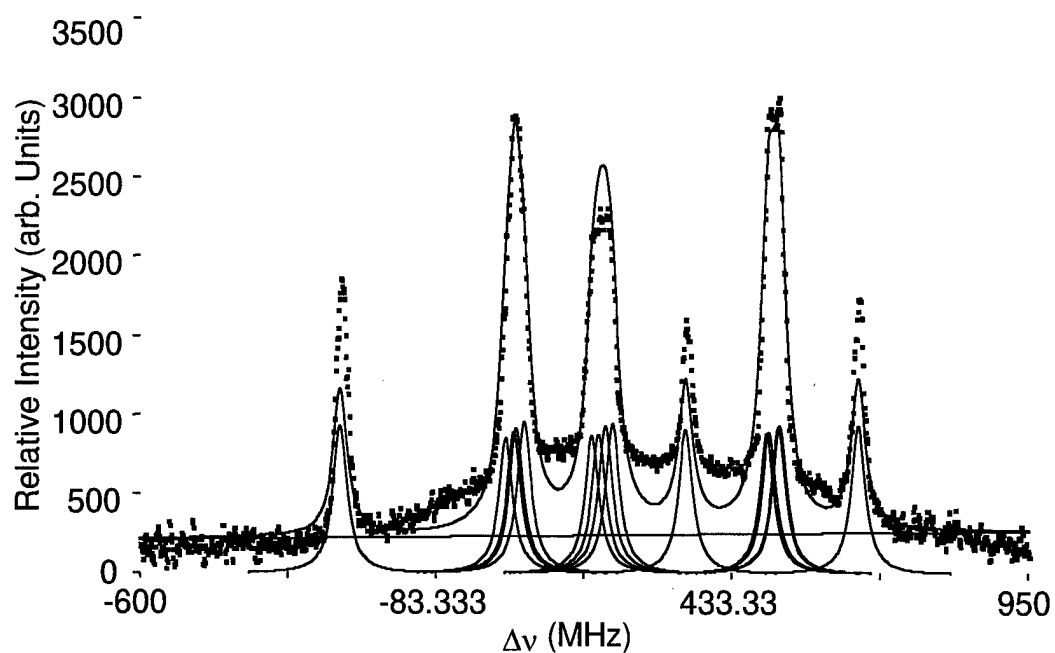


Figure 43. Phase II hyperfine fit plot for P(70) 17-1. This is the same spectrum shown in Figure 41.

Table 9. Phase II hyperfine fit parameters for P(70)17-1

Peak	Center (MHz)	FWHM (MHz)
1	-251.2	29.3
2	38.5	
3	52.9	SNR
4	56.9	55.24
5	71.1	
6	189.3	r-squared
7	201.1	0.937
8	212.9	
9	225.3	
10	353.3	
12	494.5	
13	498.4	
14	514.7	
15	517.0	

The resultant hyperfine linewidths, 29.3 MHz, are greater than those found in Phase I, as stated previously. As before, the two end lines are not well-represented by the theoretical intensities. Appendix C contains the details for the temperature extraction, the summary of which is presented in Table 10. Figure 51 shows the comparison between the thermocouple reference measurements with the optical measurements for this transition.

Table 10. Data summary for P(70)17-1 Phase II temperature measurements.

<i>Position</i>	<i>SNR</i>	<i>R2</i>	<i>FWHM (MHz)</i>	<i>FWHM Uncertainty (MHz)</i>	<i>Extracted Temp (K)</i>	<i>Actual Temp (K)</i>
4 "	143.8	0.978	774.3	4.7	1099	316.4
3 "	139.3	0.981	792.6	4.2	1151	330.8
2 "	100.3	0.981	817.1	4.2	1224	357.2
1 "	64.4	0.98	827.2	3.4	1254	403.3

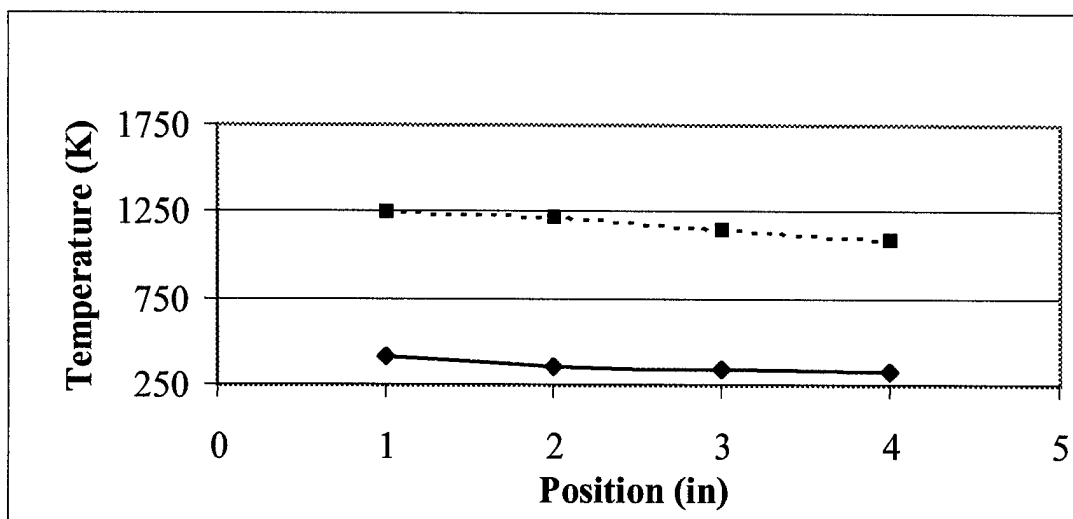


Figure 44. Temperature comparison for P(70)17-1 transition. Dotted Line=optical measurements; Solid Line=thermocouple measurements.

Table 10 also incorporates the statistical standard error in FWHM from the fit, simply to indicate that it is small when compared to the FWHM value. The temperatures for this

transition are again elevated, when measured using Doppler-limited saturation spectroscopy. Though clearly incorrect, the declining trend in temperature as the measurement position changes is gradual and seemingly continuous, whereas in Phase I there were disproportionate jumps.

Appendix C also includes a study of the fit residuals, which are remarkably similar for all the positions. There are three negative peaks and two positive peaks, at about the same relative position in frequency space. This most likely points to incorrect relative line intensities, since there is no way to attribute a sinusoidal residual variation with a baseline subtraction problem.

Figure 45 shows the hyperfine fit for P(70) 17-1, with relevant parameters listed in Table 11. This hyperfine scan is a closer view of the profile in Figure 42, with 21 Lorentzian peaks.

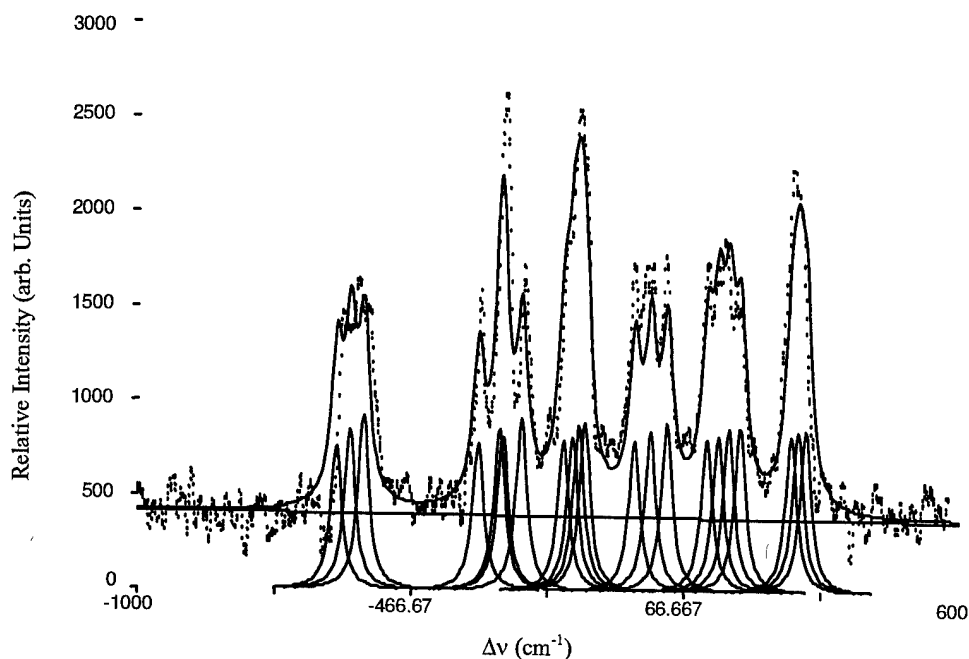


Figure 45. Phase II hyperfine fit plot for P(53) 19-2. This is the same spectrum shown in Figure 42.

Table 11. Phase II hyperfine fit Parameters for P(53)19-2

Peak	Center (MHz)	FWHM (MHz)
1	-610.8	26.2
2	-584.5	
3	-558.1	SNR
4	-334.4	13.9
5	-292.7	
6	-286.7	r-squared
7	-249.8	0.903
8	-168.1	
9	-150.3	
10	-138.3	
11	-126.3	
12	-29.7	
13	1.5	
14	33.7	
15	111.4	
16	133.5	
17	154.1	
18	176.3	
19	275.4	
20	288.8	
21	303.7	

The 26.2 MHz natural linewidths are again greater than those found in Phase I, but are very similar for both transitions in Phase II. It is likely that the true natural linewidths are closer to 30 MHz than it is to 10 MHz, since the sectioning of data for Phase I precluded the residual broadened lineshape at the base of the hyperfine profiles. Pressure broadening was not influencing hyperfine lineshapes, since the pressure in the cell was only 0.2 mm Hg, which is less than the room temperature vapor pressure of I_2 , which is 0.31 mm Hg. Generally, pressure broadening does not show significant impact until a diatomic gas reaches pressures of about 1 mm Hg.²³

Appendix C contains the details for the temperature extraction, the summary of which is presented in Table 12. Figure 46 shows the comparison between the thermocouple reference measurements with the optical measurements for this transition.

Table 12. Data summary for P(53)19-2 Phase II temperature measurements.

<i>Position</i>	<i>SNR</i>	<i>R2</i>	<i>FWHM (MHz)</i>	<i>FWHM Uncertainty (MHz)</i>	<i>Extracted Temp (K)</i>	<i>Actual Temp (K)</i>
4 "	99.2	0.990	555.8	3.4	566	316.4
3 "	68	0.990	643.4	3.1	759	330.8
2 "	57.3	0.993	656.1	2.6	789	357.2
1 "	49.6	0.995	672.2	2.2	828	403.3

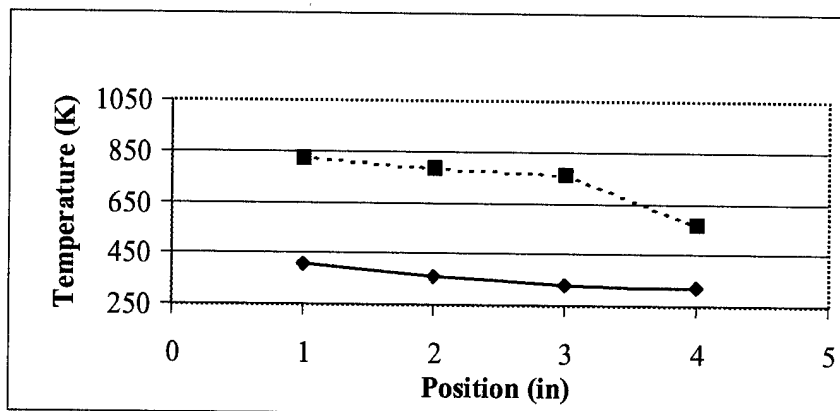


Figure 46. Temperature comparison for P(53) 19-2 transition. Dotted Line=optical measurements; Solid Line=thermocouple measurements.

Table 12 also gives the statistical standard FWHM error from the fit; again, this error is far too minor to account for the poor temperature determination. Appendix C has the accompanying residual study for all four measurements, to show that there is no overwhelmingly obvious trend which can account for the error. There are many interesting factors about these results. First, the more careful experimental procedures in Phase II did not change the erroneous fit values. Though a systematic error is still possible, the steps in Phase II should have eliminated the majority of the unknowns in this area. Second, not only are the extracted temperatures wrong, but they do not match one another between the two transitions. This also points to the possibility that the error may not be systematic, but may be due to an omission in the theoretical understanding of this technique.

The residual trends all seem to take on the same character. The two-positive-peak, three-negative-peak residual after the fit is complete is consistent for both transitions for all temperature measurements. This in itself is encouraging, for it suggests a possible solution to the temperature error problem; however, this solution is not clear at this point.

V. Discussion and Recommendations

The ability of Doppler-limited saturation spectroscopy to measure absorption spectra that are spatially resolved has been demonstrated. The nature of the technique ensures that the measured interaction occurs only at the spatial location where both beams are present. The chopping of the pump beam, and its presence in the medium modulate the CW probe beam to produce the measurable result. At the points where the beams do not overlap the probe beam is not modulated; therefore, the resulting lock-in signal is zero. This technique offers unique capabilities, as it can be used in any Doppler-broadened medium. The spatial resolution of such measurements is a marked improvement over line-integrated optical procedures, allowing for measurements in a $1 \times 1 \times 12$ mm volume of gas. It is possible to improve this spatial resolution by increasing the beam crossing angle, but this was the finest resolution that could be achieved within the physical limitations of the sample cell that was used in the present experiment.

The overall trends and lineshape changes are encouraging, for they indicate that different temperature profiles do have unique characteristics. Unfortunately, the temperatures extracted from these spatially resolved profiles did not return realistic values. There appears to be an omission of a detail, probably simple, which is not allowing the procedure as designed to return an accurate measurement of temperature. The omission can be either in the experiment or in the theory.

It is possible that the discrepancy is still due to some systematic error with the experiment. Perhaps the number of parameters allowed to float in the Peakfit overextended the capabilities of the package. There may even be another broadening

mechanism which was unaccounted for by the experimenter in the theoretical development. Though there are many such possibilities, the careful design of the Phase II experiments should have eliminated the majority of sources that could have caused a 400% reading error.

Perhaps there is an omission in the theory, as it stands, which does not account for the temperature-dependent broadening of the fine structure lines in molecular iodine. The theoretical intensities that are related to the factor $2F + 1$ did not really match the hyperfine data in this experiment, especially for the two end lines in P(53) 19-2. The single lines at either end of the spectrum were much higher than some of the doublet or triplet overlaps. The residual broadened lineshape, too, may not be completely attributable to the natural linewidth. This residual shape, if it changes with temperature, could drastically affect the extracted Gaussian widths.

The foundationary theoretical development for hyperfine interactions, including the intensity proportionality, was formulated for microwave frequencies.¹⁸ For optical wavelengths, it is possible that nonlinear, frequency-dependent effects are influencing line intensities. If there is such a nonlinear effect occurring with relation to the hyperfine intensities, it could drastically change the theoretical understanding that is the foundation for this technique. Unfortunately, the literature that exists at the time of this writing only deals with the positions of hyperfine lines, and does not contain empirical data which lead to an understanding of the intensities.

In addition, if saturation effects, which were not considered, are occurring, then some line intensities could be suppressed in the absorption profile. Such effects might also explain the residual lineshape, due to the high absorption within the medium, and

possible reemission at the pump beam's chopped frequency. This reemission would see a medium that is optically transparent because it is saturated, and the result would be the Doppler-broadened profile.

Because of the high utility of this spatially-resolved temperature measurement technique, this work should be continued in order to narrow down the field of possibilities for producing inaccurate temperature extraction. A prioritized list of possible future experiments is offered in Table 15.

Table 13. Future Experimentation.

<i>Experiment</i>	<i>Justification</i>
Doppler-free vs. Temperature	If hyperfine widths are temperature dependent, then this may point to another broadening mechanism affecting the lines. If the intensities are temperature dependent, then possible theoretical explanations should be sought.
Doppler-free and Doppler-limited vs. Crossing Angle	The angle at which the beams cross affects the interaction volume, and so may point to a saturation phenomenon. Also, off-angle vector elements of the pump beam's wave propagation vector might be reaching the detector, causing the residual lineshape.
Doppler-free and Doppler-limited vs. Pressure	Ensures that pressure broadening is not significant
Doppler-free and Doppler-limited vs. Beam Intensity and Beam Intensity Ratio	May uncover some nonlinear affects. Also may show that the ratio of power between the probe and pump beams significantly affects the resulting spectra.
Perform Experiment for other Transitions	May uncover some nonlinear affects. Look at relative intensities of the hyperfine lines and compare to both theory and to those of other transitions.
Perform Symmetry Analysis on Doppler-Limited Profiles	May increase temperature sensitivity and accuracy.
Perform Temperature Measurements on Overlapping Line Sets	Requires reconciliation of relative line intensities, but should increase temperature sensitivity.

This project has demonstrated that the technique shows some merit, as variations in spatially-resolved Doppler-profiles have been detected. Now that the spatial resolution and the temperature differentiation of the technique have been demonstrated, refinement of procedures and theory to allow an accurate extraction of temperature will complete the picture. There is not as of yet sufficient data to offer a diagnostic tool; however, this work lays the foundation for future endeavors.

VI. References

1. Verdeyen, Joseph T. Laser Electronics (Third Edition). New Jersey: Prentice-Hall, 1995.
2. Demtröder, Wolfgang. Laser Spectroscopy Basic Concepts and Instrumentation (Chemical Physics 5). Heidelberg: Springer-Verlag, 1981.
3. Webster, John G. "Chemical Lasers," Encyclopedia of Electronics and Electronics Engineering, vol. 3. New York: John Wiley and Sons
4. Bloomberg and Patel. "APS Study," Review of Modern Physics 593, Part II (1987)
5. Gerstenkorn, S. And Luc, P. Atlas du Spectre d'Absorption de la Molecule de l'iode. Paris: Editions du CNRS, 1978
6. Mulliken, Robert S. "Iodine Revisited," The Journal of Chemical Physics, 33 #1:288-309 (July 1972).
7. Herzberg, Gerhard. The Spectra and Structures of Simple Free Radicals, An Introduction to Molecular Spectroscopy. New York: Dover Publications, 1971.
8. Brown, John M. Molecular Spectroscopy, Oxford Chemistry Primer Series #55. Oxford: Oxford University Press, 1998.
9. Eisberg, R. And Resnick, R. Quantum Physics of Atoms, Molecules, Solids, Nuclei, and Particles. New York: John Wiley and Sons, 1985.
10. Levenson, Marc D. Hyperfine Interactions in Molecular Iodine. Stanford University PhD Dissertation, 1972.

11. Struve, Walter S. Fundamentals of Molecular Spectroscopy. New York: John Wiley and Sons, 1989.
12. Steinfeld, Jeffrey I. An Introduction to Modern Molecular Spectroscopy. Cambridge: MIT Press, 1978.
13. Herzberg, Gerhard. Spectra of Diatomic Molecules. New York: Van Nostrand Reinhold Company, 1950.
14. Luc, P. "Molecular Constants and Dunham Expansion Parameters Describing the B-X System of the Iodine Molecule," Journal of Molecular Spectroscopy, 80:41-55 (1980).
15. Tellingheusen, Joel, McKeever, Mark R., and Sur, Abha. "Reanalysis of the D-X Fluorescence Spectrum," Journal of Molecular Spectroscopy, 82: 225-245 (1980).
16. Glessner, John W. Amplified Spontaneous Emission of the Iodine $B^3\Pi(0^+_u)$ - $X^1\Sigma(0^+_g)$ System. PhD Dissertation, Air Force Institute of Technology (AU), Wright Patterson AFB OH, 1987.
17. Kroll, M., and Innes, K. K. "Molecular Electronic Spectroscopy by Fabry-Perot Interferometry. Effect of Nuclear Quadrupole Interactions on the Line Widths of the $B^3\Pi(0^+_u)$ - $X^1\Sigma(0^+_g)$ Transition of the I_2 Molecule," Journal of Molecular Spectroscopy 36: 295-309 (1970).
18. Townes, C. H. And Schawlow, A. L. Microwave Spectroscopy. New York: McGraw-Hill, 1955.
19. Davis, Kendall B. The Hyperfine Structure of Molecular Iodine. B. A. Thesis, Middlebury College, Middlebury, VT, May 1980.

20. Kroll, M. "Hyperfine Structure in the Visible Molecular Iodine Absorption Spectrum," Physical Review Letters 23 #12: 631-633 (September 1969).
21. Robinson, G. W. And Cornwell, C. D. "The Interaction with Molecular Rotation of the Nuclear Electric Quadrupole Moments of Two Nuclei Having Spins $3/2$," The Journal of Chemical Physics 21 #9: 1436-1442 (1951).
22. Shimoda, K. "Line Broadening and Narrowing Effects," in High Resolution Laser Spectroscopy (Topics in Applied Physics Vol. 13). Ed. K. Shimoda. New York: Springer-Verlag, 1976.
23. Demtröder, Wolfgang. Laser Spectroscopy Basic Concepts and Instrumentation (Chemical Physics 5). Heidelberg: Springer-Verlag, 1981.
24. Letokhov, V. S. And Chebotayev, V. P. Nonlinear Laser Spectroscopy. Berlin: Springer-Verlag, 1977.
25. Velchev, I., van Dierendonck, R., Hogervorst, W., and Ubachs, W. "A Dense Grid of Reference Lines for Optical Frequency Calibration in the Range 571-596 nm," Journal of Molecular Spectroscopy 187: 21-27 (1998).

APPENDIX A

Wavemeter Calibration Procedure

This procedure is meant to provide guidance for making very fine wavemeter calibrations (\pm a few MHz) using a Ring Dye Laser operating in the 570-610 nm range. The procedure employs Doppler-free saturation spectroscopy to measure the hyperfine spectra for several transitions in molecular iodine, and involves comparison of specific lines to those in a catalog provided by Velchev et. al.²⁵ Figure A-1 shows the optical table setup diagram that accompanies the following procedures:

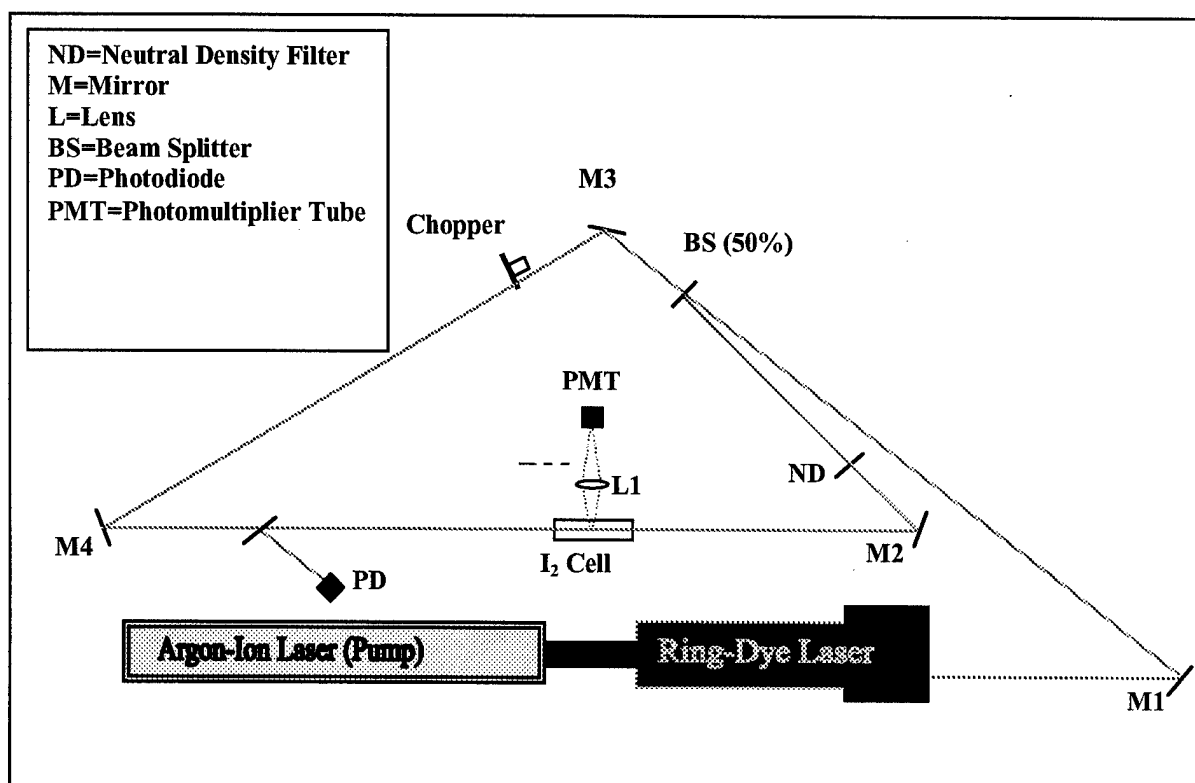


Figure A-1. Table setup for ring dye laser wavemeter calibration

1. Setup the optical Table as shown in Figure A-1, using a glass I₂ cell:
 - a) Ensure the beams are counterpropagating and completely overlap through the cell.
 - b) Ensure L1 focuses the emitted light from the cell to the PMT.
 - c) Set the chopper frequency very high (~3000 Hz).
 - d) Run a line from the chopper to use as the reference for two lock-in amplifiers.
 - e) Run a line from the PD to use as the signal input for lock-in #1
 - f) Run a line from the PMT to use as the signal input for lock-in #2
 - g) The ring dye laser's output should be at least 350 mW at the peak of the dye curve in single frequency mode.

Note: lenses may or may not be necessary to focus the beams through the cell. Overlapping with lenses is tricky and will take some time. Adjustable apertures are better for the limiting of the beam diameter going through the cell.

2. Set autoscan for a 100 GHz Doppler-limited emission measurement. The results of this scan will be compared to published I₂ reference lines. The specific center frequencies are given in the atlas by Gerstenkorn and Luc.⁵
 - a) Transfer control of the laser to the autoscan program.
 - b) Set wavelength = 17334 wavenumbers.
 - c) Change Data Interval to 50 MHz.
 - d) Change Segment Scan Time to 10s/10 GHz.
 - e) Change Scan Distance to 100 GHz.
 - f) Edit Sensor List to only read from lock-in #2 (emission measurements)
 - g) Execute Scan

3. Compare resultant spectrum to the I2 atlas. The lines should agree with some degree of reasonability (at least 0.1 K. If not, then there is likely a misalignment in the wavemeter. This determines a rough estimate of the wavemeter error.

4. Setup autoscan for a 3.5 GHz 0-Doppler hyperfine absorption measurement.
 - a) Set wavelength = one of the start scan values in Table A-1.
 - b) Change Data Interval to 1 MHz.
 - c) Change Segment Scan Time to 500s/10 GHz.
 - d) Change Scan Distance to 3.5GHz.
 - e) Edit Sensor List to only read from lock-in #1 and 2 (This will allow you to display both the hyperfine components and the Doppler-broadened line)
 - f) Execute Scan

Table A-1. Reference positions for "t" hyperfine components²⁵

Transition	"t" component (Hz)	"t" component (K)	Start Scan (K)	Scan Width (GHz)
P(65) 16-1	5.171856956E+14	1.725145786E+04	17251.25	3.5
P(119) 18-1	5.197223960E+14	1.733607308E+04	17335.85	3.5
P(116) 18-1	5.199643760E+14	1.734414466E+04	17343.94	3.5
R(124) 18-1	5.193047619E+14	1.732214230E+04	17321.93	3.5

5. Compare "t" component positions to obtain a refined value for the wavemeter offset necessary to correct the error. For the odd-J lines (P(65) and P(119)), there are 21 hyperfine lines, while for the even-J lines (P(116) and R(124)), there are 15 hyperfine lines. For even J-lines, the "t" component is defined to be the lowest energy line,

while for odd J-lines, it is the second lowest energy line.²⁵ Figure A-2 Clarifies this definition.

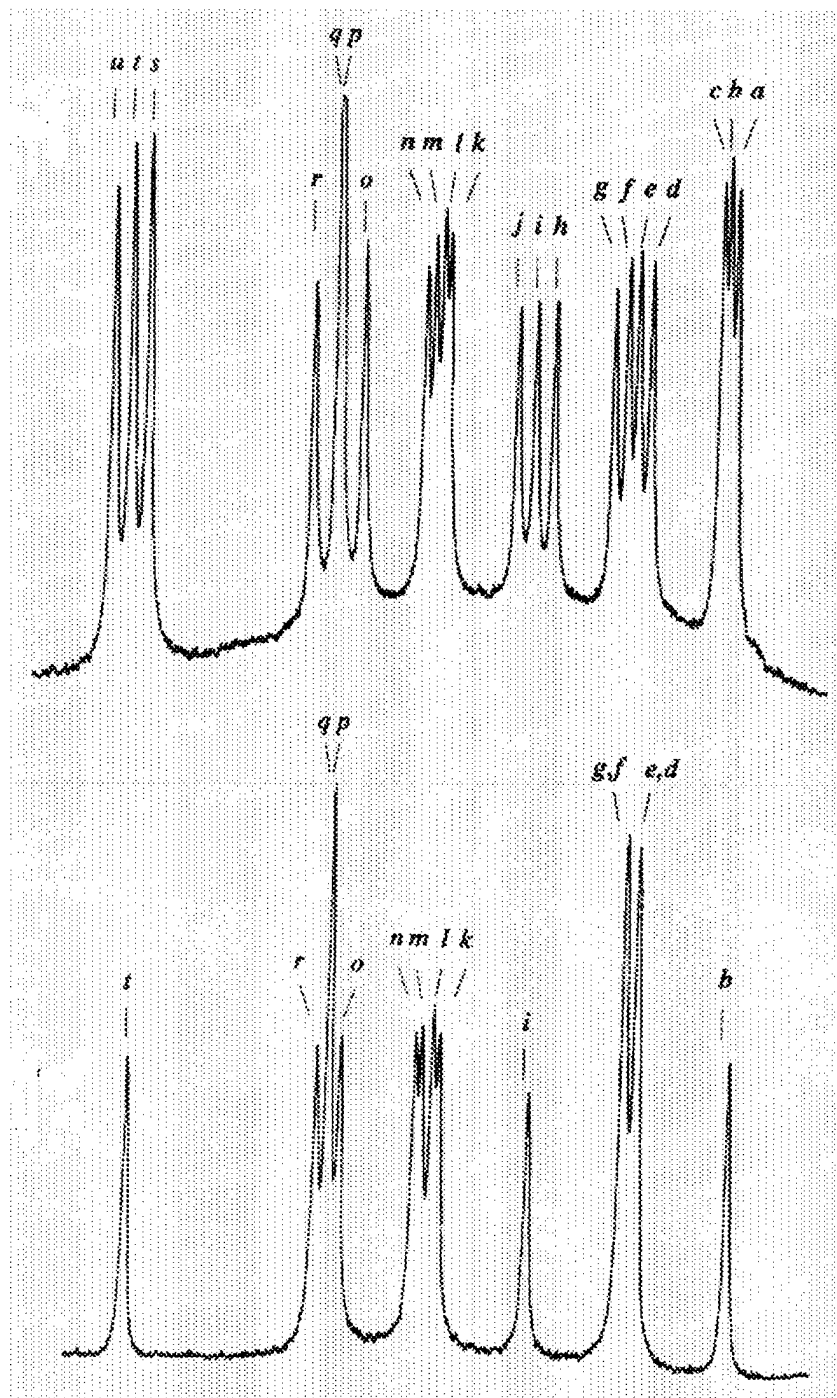


Figure A-2. Definition of the "t" component²⁵

APPENDIX B

Estimating the Interaction Volume of Two Crossing Cylindrical Beams

This is a development which allows for the approximation of the volume enclosed by two cylinders intersecting at some angle Θ . This is an approximation for two reasons: 1) $\text{TEM}_{0,0}$ laser beams have a Gaussian profile, and are not cylindrical; 2) It uses simple geometrical averages to provide an estimate of the intersection. As a first approach, we can estimate the volume inside a cylinder by averaging the volumes of two rectangular beams. One of the rectangles is inscribed within the cylinder, while the other circumscribes it, as in Figure B-1.

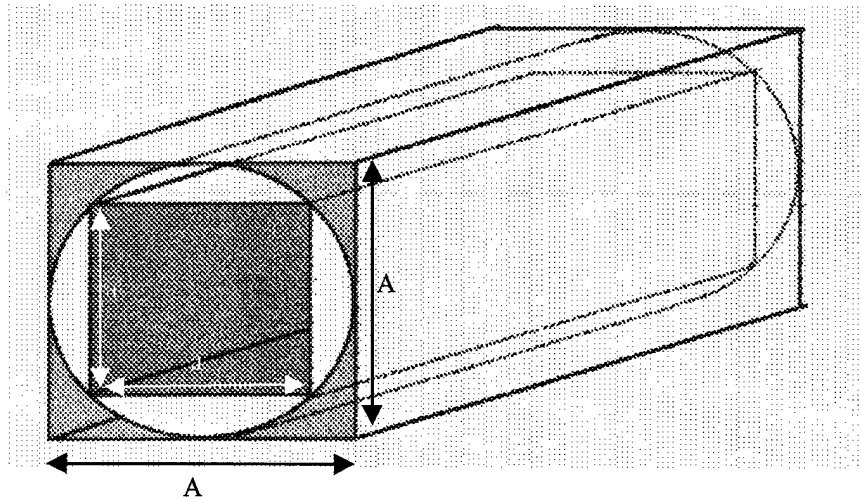


Figure B-1. Approximating the volume of a cylindrical beam as the average of an inscribed rectangular beam and a circumscribed rectangular beam. The circumscribed rectangle has a cross sectional area A^2 , and the inscribed rectangle has a cross sectional area a^2 .

Knowing the radius of the cylinder (R), we know the lengths of the sides of these rectangular beams:

$$A = 2 \cdot R \quad (B.1)$$

$$a = \sqrt{\left(\frac{A}{2}\right)^2 + \left(\frac{A}{2}\right)^2} = \sqrt{2 \cdot R^2} = \sqrt{2} \cdot R \quad (B.2)$$

If there are two rectangles crossing at an angle, the area of intersection is a polygon, which is shown in Figure B-2, with sides α , β .

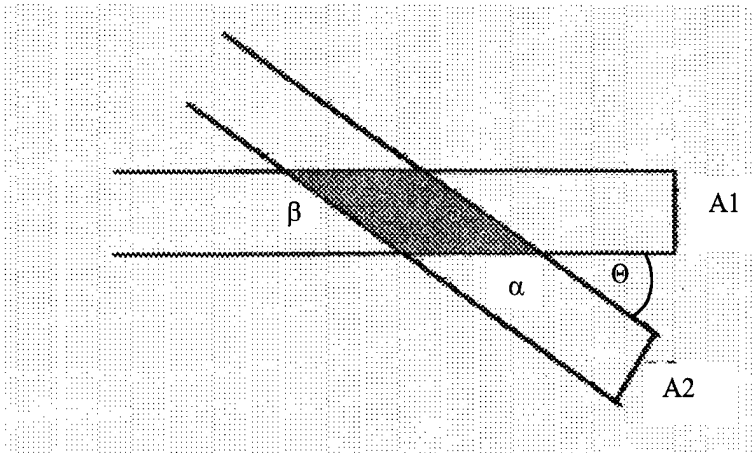


Figure B-2. Polygon created by the intersection of two rectangles. A1 and A2 are the lengths of the sides of the square cross section for beams 1 and 2, respectively.

If we then add the third dimension, the volume of interaction for these intersecting beams is then the area of this polygon multiplied by either A1 or A2, whichever is smaller. We now have a way to describe the interaction volume of two independent rectangular beams:

$$V = \alpha \cdot \beta \cdot \sin(\Theta) \cdot A_{\text{small}} \quad (B.3)$$

where

$$\alpha = A_2 / \sin(\Theta) \quad \beta = A_1 / \sin(\Theta)$$

To approximate the volume of the cylinder, we take the average between the volume of interaction for the circumscribed rectangles and the inscribed rectangles.

$$V_a = (V + v) / 2 \quad (B.4)$$

where

V, v = the interaction volumes for the circumscribed rectangles and the inscribed rectangles, respectively

This approach has an error constant associated with it, which is simply the ratio of the approximate volume of a simple cylinder of length L to the real volume of the same cylinder. Any volume resulting from this approximate average would need to be multiplied by this error constant in order to provide a close estimate.

For a generic cylinder, radius = 0.5 mm and length = 10 mm, the approximate volume is:

$$A = 1 \text{ mm} \quad a = 0.707 \text{ mm} \quad V = 10 \text{ mm}^3 \quad v = 5 \text{ mm}^3$$

$$V_a = 15/2 = 7.5 \text{ mm}^3$$

And the actual volume is:

$$\pi r^2 L = 7.854 \text{ mm}^3$$

The ratio between the two is therefore 0.955. This ratio is true regardless of which dimensions one is to pick. So, the approximate interaction volume must be multiplied by this factor in order to return a volume close to that of two intersecting cylinders.

For this thesis, the two beams were measured at equal radii=0.5 mm. The beams crossed at an angle=3.8 degrees. From these parameters, the interaction volume is found to be 11.8 mm³.

APPENDIX C

Presentation of Additional Data

Phase I. P(53) 19-2 Temperature Determination

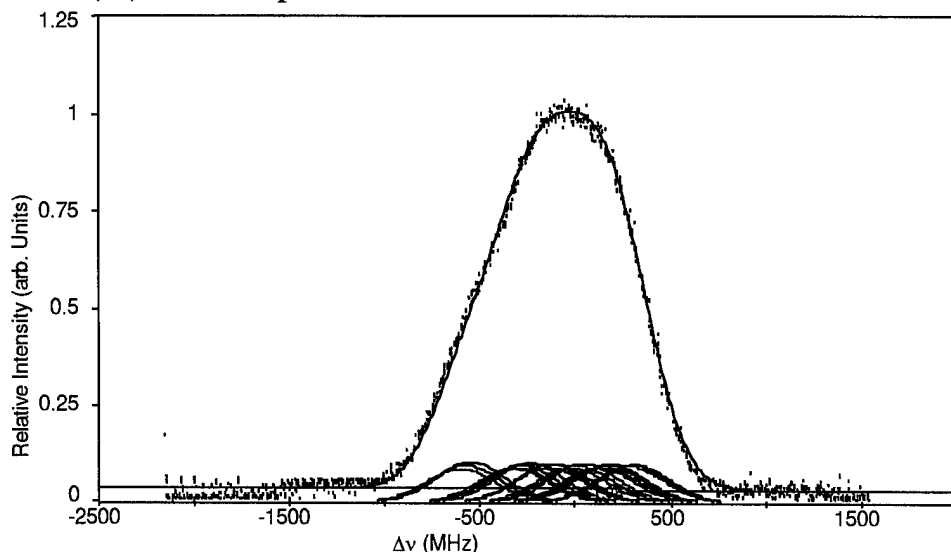


Figure C-1. P(53) 19-2 Doppler-broadened transition at the cold end of the Phase I cell, measured using Doppler-limited saturation spectroscopy. SNR=53.0, mean baseline=0.02 \pm 0.02, $R^2=0.997$, FWHM =422 MHz, Extracted Temperature=326 K

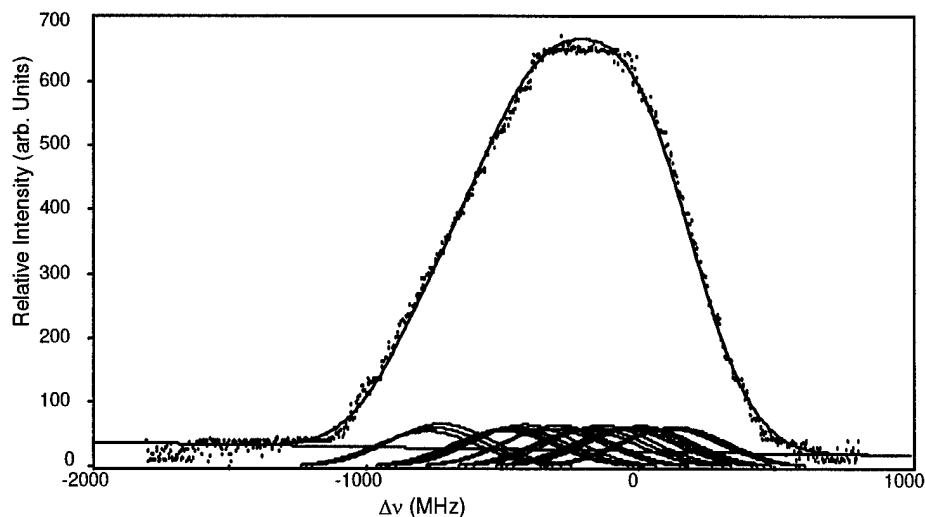


Figure C-2. P(53) 19-2 Doppler-broadened transition at the warm center of the Phase I cell, measured using Doppler-limited saturation spectroscopy. SNR=51.2, mean baseline=13.7 \pm 12.7, $R^2=0.998$, FWHM =441 MHz, Extracted Temperature=356 K

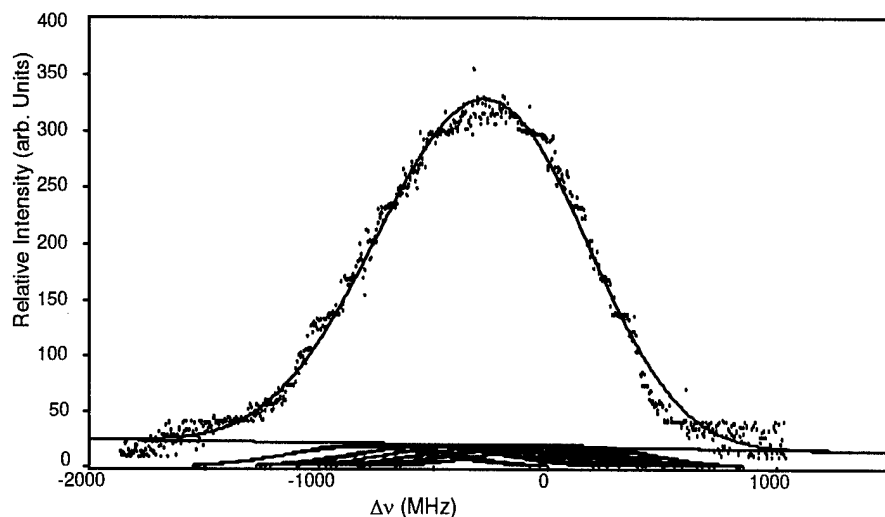


Figure C-3. P(53) 19-2 Doppler-broadened transition at the cot end of the Phase I cell, measured using Doppler-limited saturation spectroscopy. SNR=34.0, mean baseline=14.4 \pm 9.7, $R^2=0.989$, FWHM =775 MHz, Extracted Temperature=1102 K

The residuals for Phase I measurements were not considered in order to focus on the elimination of systematic errors in the experimental apparatus. Phase II measurements will include a fit residual analysis to determine whether or not there might be a predictable trend in the data error between the measurements and the fit parameters.

Phase II. P(70) 17-1 Temperature Determination and Residual Study

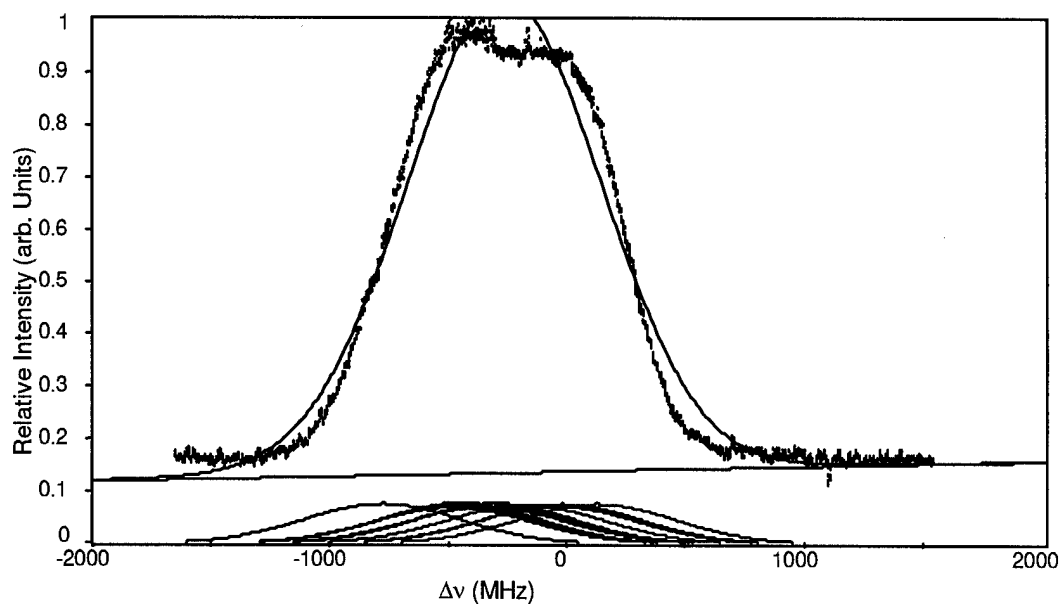


Figure C-4. P(70) 17-1 Doppler-broadened transition at the 4 '' position of the Phase II cell, measured using Doppler-limited saturation spectroscopy. SNR=143.8, mean baseline=0.0169 +/- 0.00696, $R^2=0.978$, FWHM = 774.3 MHz, Extracted Temperature=1099 K

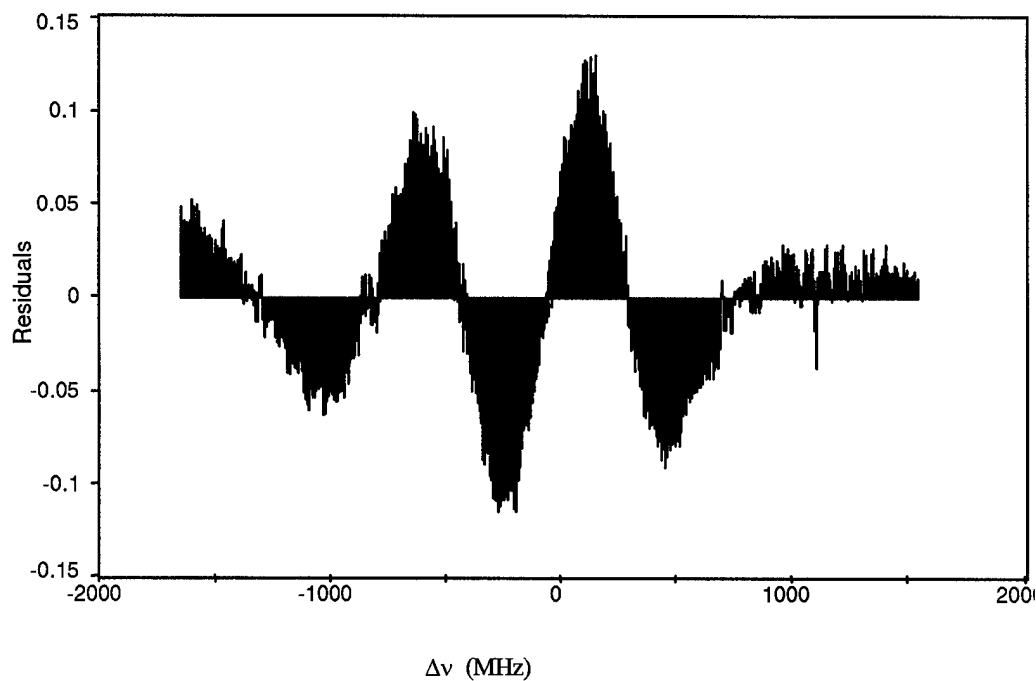


Figure C-5. P(70) 17-1 residual trend for the 4 '' Doppler-limited fit.

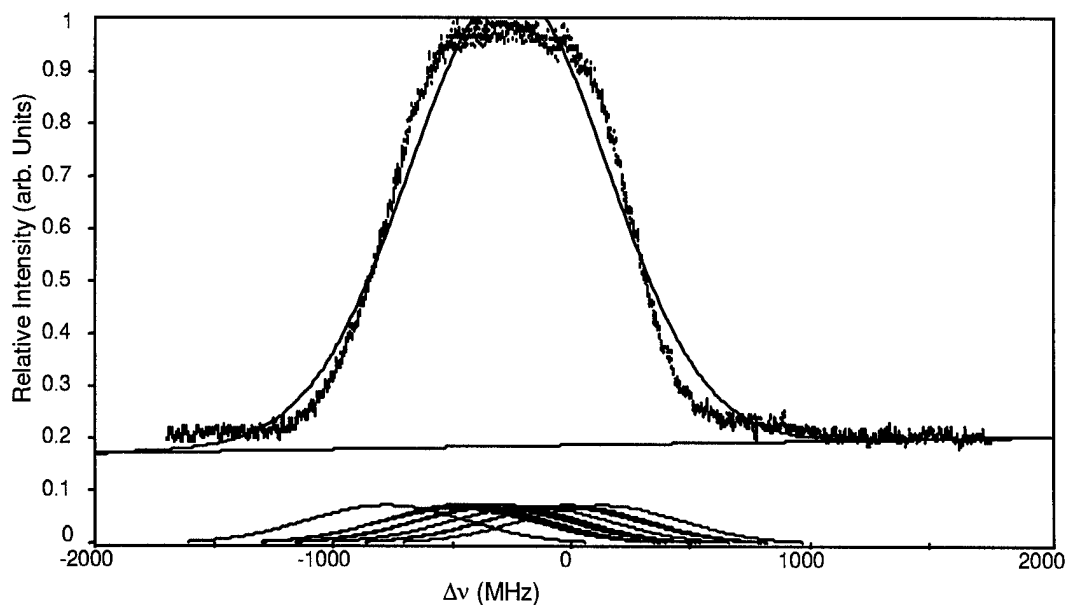


Figure C-6. P(70) 17-1 Doppler-broadened transition at the 3 " position of the Phase II cell, measured using Doppler-limited saturation spectroscopy. SNR=139.3, mean baseline=0.208 +/- 0.00718, $R^2=0.981$, FWHM = 792.6 MHz, Extracted Temperature=1151 K

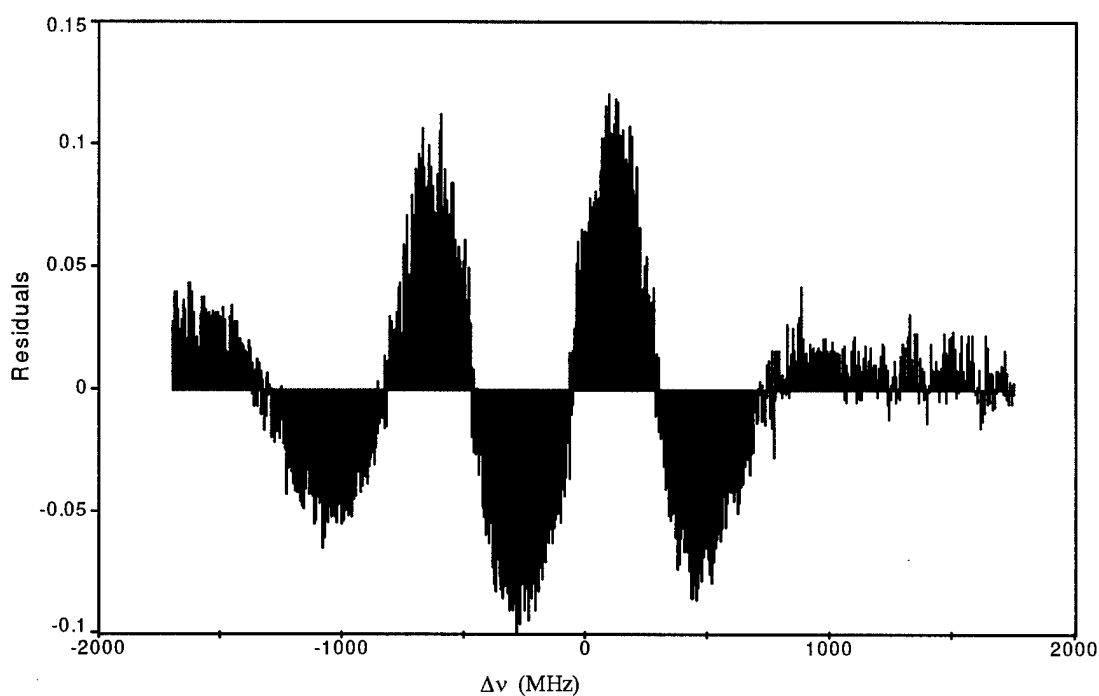


Figure C-7. P(70) 17-1 residual trend for the 3 " Doppler-limited fit.

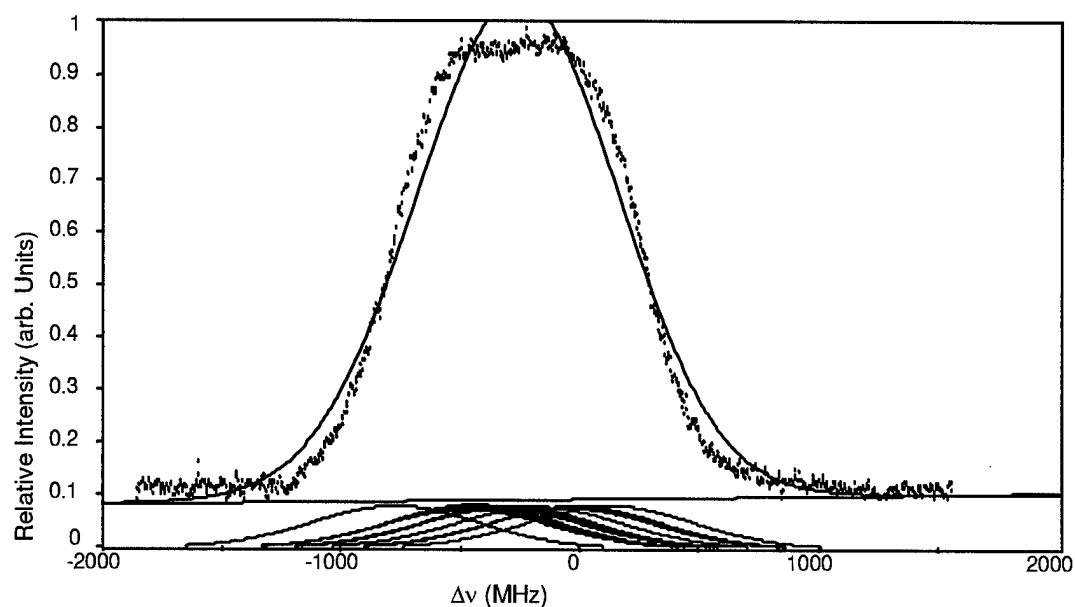


Figure C-8. P(70) 17-1 Doppler-broadened transition at the 2 " position of the Phase II cell, measured using Doppler-limited saturation spectroscopy. SNR=100.3, mean baseline= ± 0.00996 , $R^2=0.981$, FWHM = 817.7 MHz, Extracted Temperature=1224 K

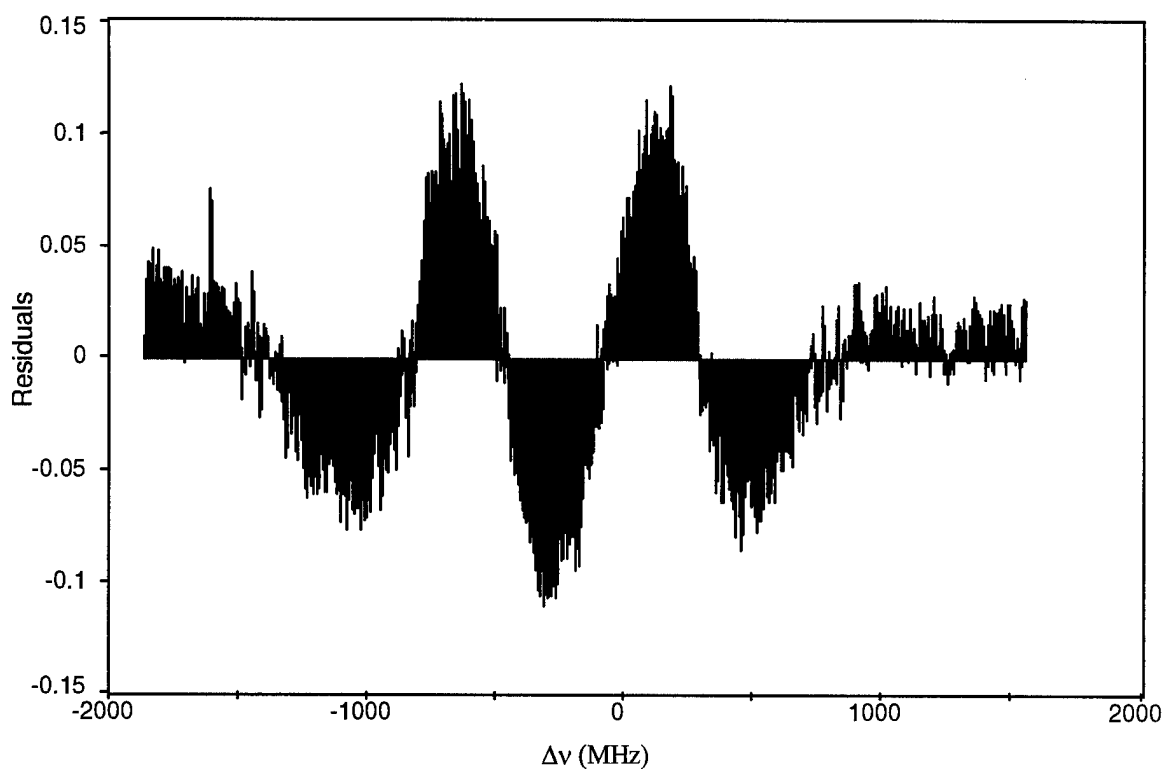


Figure C-9. P(70) 17-1 residual trend for the 2 " Doppler-limited fit.

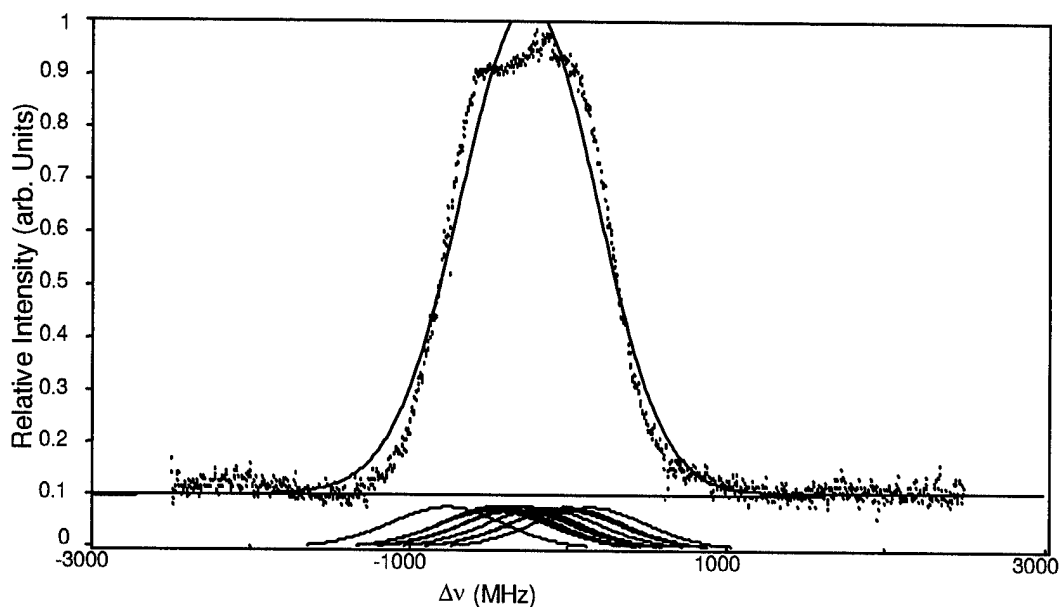


Figure C-10. P(70) 17-1 Doppler-broadened transition at the 1 " position of the Phase II cell, measured using Doppler-limited saturation spectroscopy. SNR=64.4, mean baseline=0.114 \pm 0.0155, $R^2=0.98$, FWHM = 827.2 MHz, Extracted Temperature=1254 K

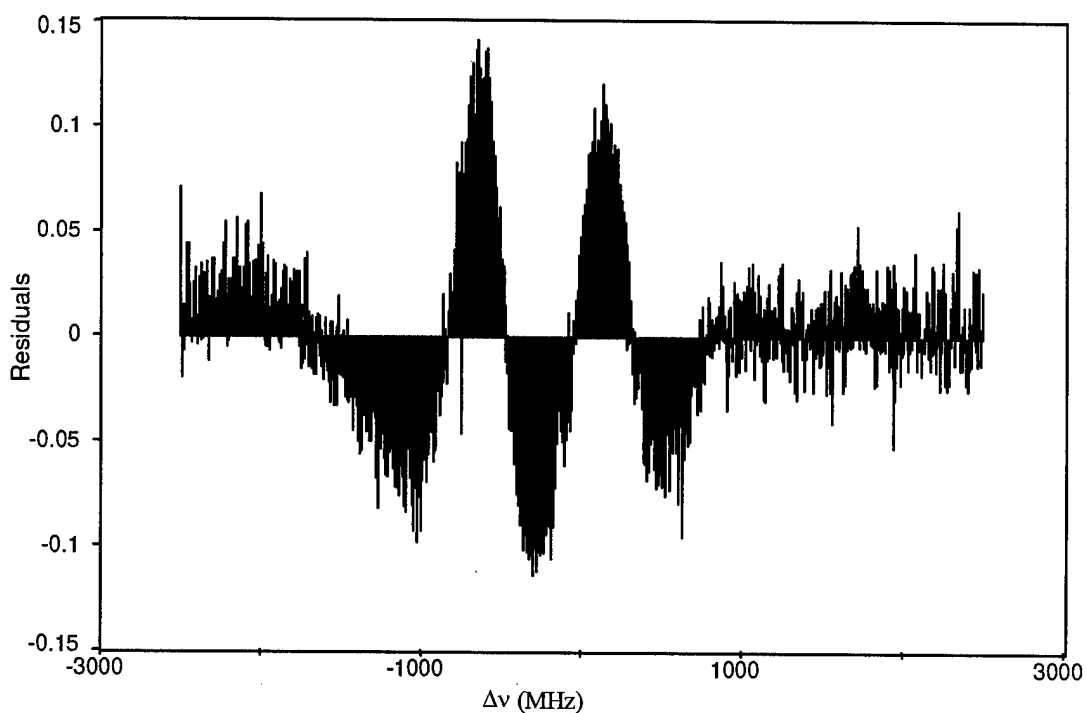


Figure C-11. P(70) 17-1 residual trend for the 1 " Doppler-limited fit.

Phase II. P(70) 17-1 Temperature Determination and Residual Study

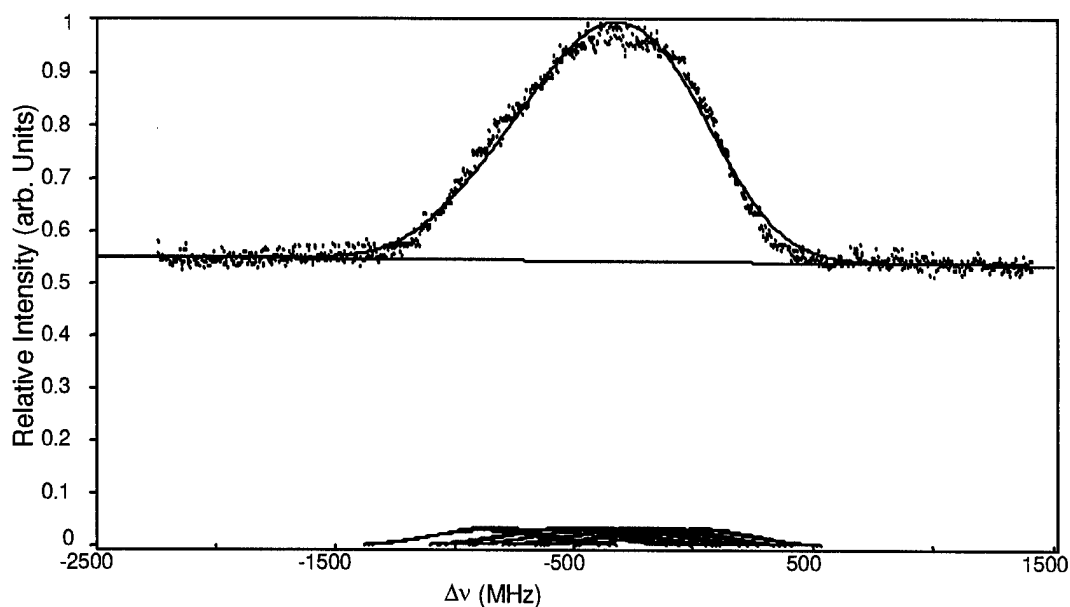


Figure C-12. P(53) 19-2 Doppler-broadened transition at the 4 " position of the Phase II cell, measured using Doppler-limited saturation spectroscopy. SNR=99.2, mean baseline=0.567 \pm 0.101, $R^2=0.99$, FWHM = 555.8 MHz, Extracted Temperature=566 K

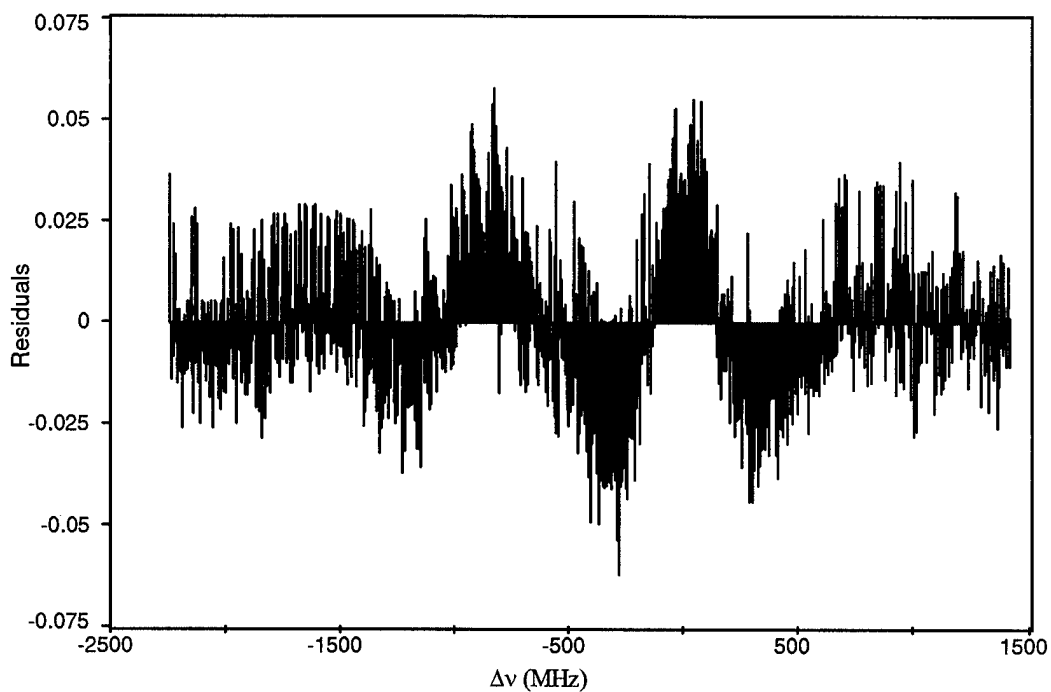


Figure C-13. P(53) 19-2 residual trend for the 4 " Doppler-limited fit.

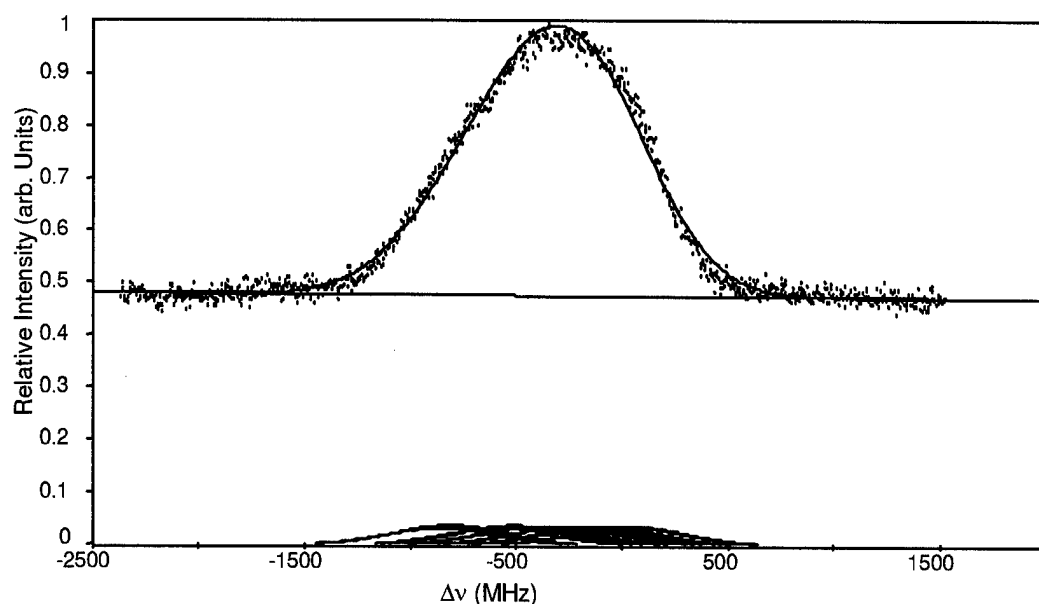


Figure C-14. P(53) 19-2 Doppler-broadened transition at the 3 " position of the Phase II cell, measured using Doppler-limited saturation spectroscopy. SNR=68.0, mean baseline=0.517 \pm 0.0147, $R^2=0.99$, FWHM = 643.4 MHz, Extracted Temperature=759 K

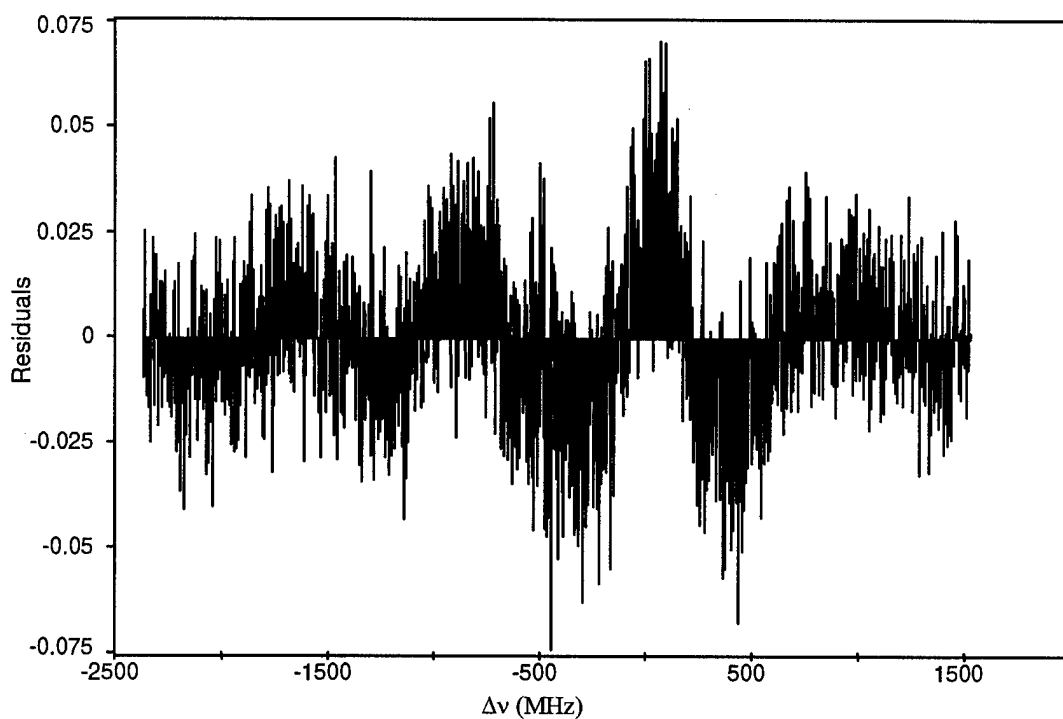


Figure C-15. P(53) 19-2 residual trend for the 3 " Doppler-limited fit.

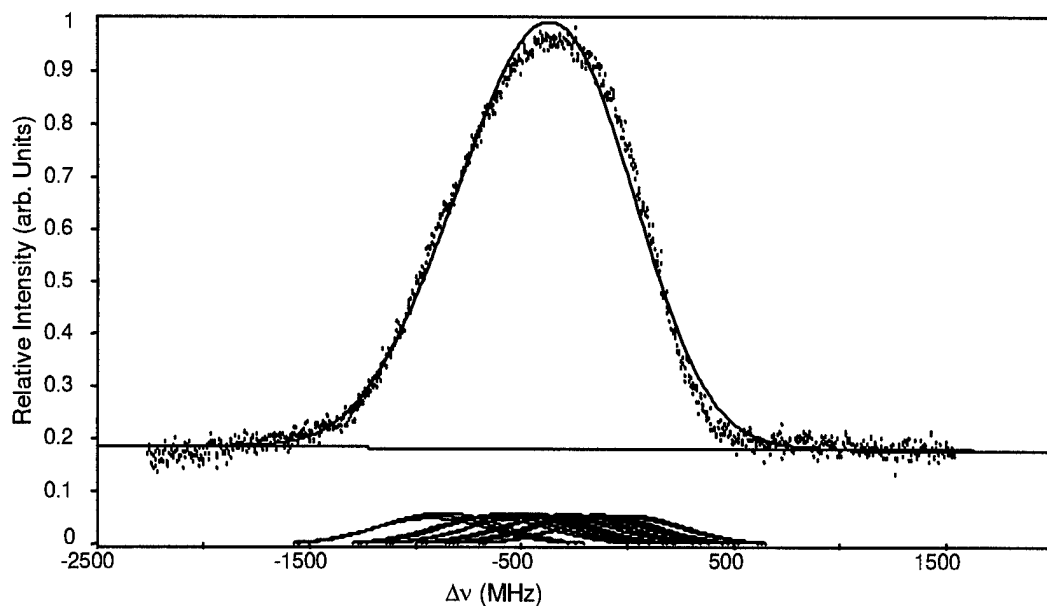


Figure C-16. P(53) 19-2 Doppler-broadened transition at the 2 " position of the Phase II cell, measured using Doppler-limited saturation spectroscopy. SNR=57.3, mean baseline=0.205 \pm 0.0174, $R^2=0.993$, FWHM = 656.1 MHz, Extracted Temperature=789 K

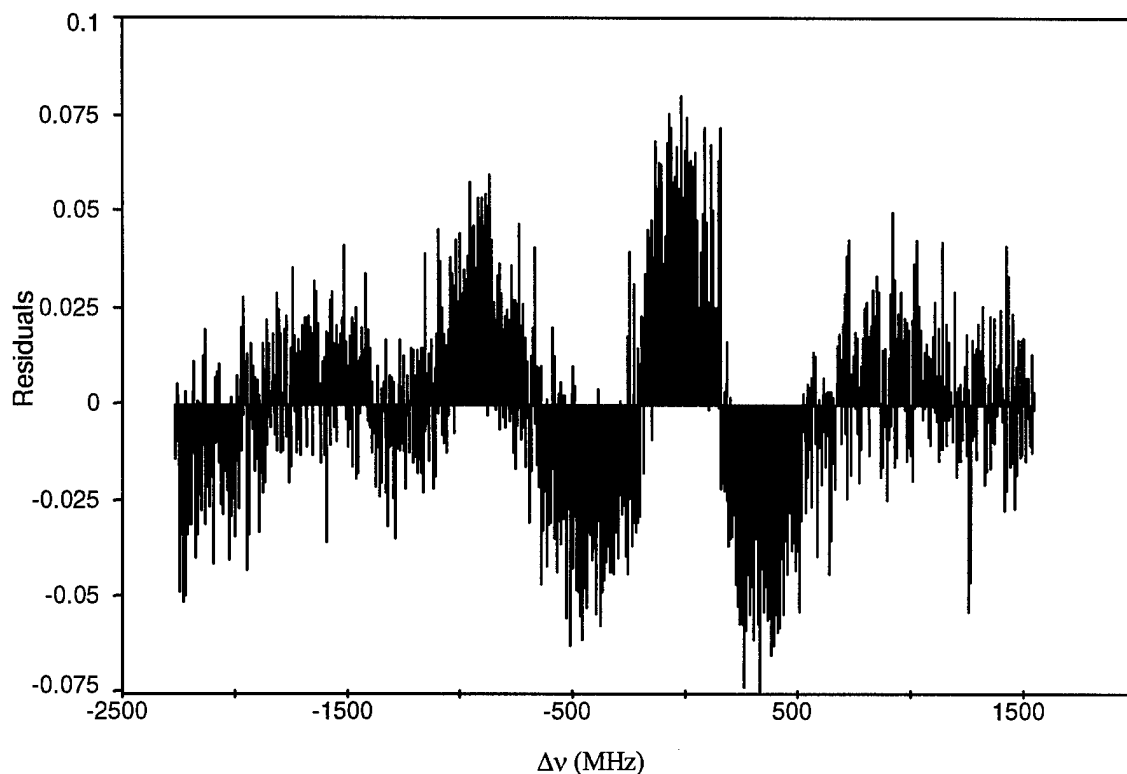


Figure C-17. P(53) 19-2 residual trend for the 2" Doppler-limited fit.

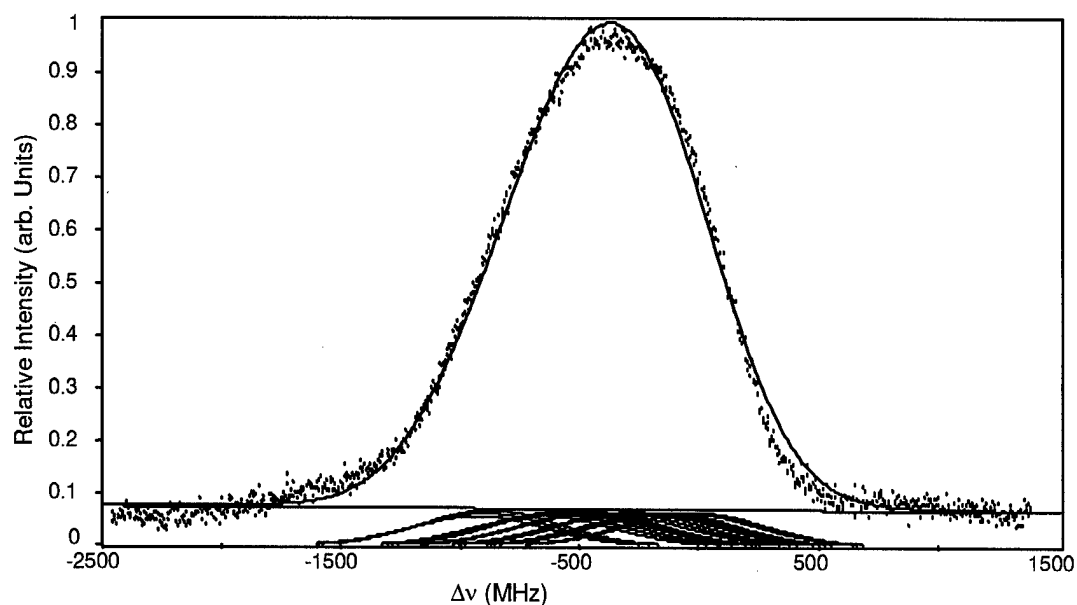


Figure C-16. P(53) 19-2 Doppler-broadened transition at the 1 " position of the Phase II cell, measured using Doppler-limited saturation spectroscopy. SNR=49.6, mean baseline=0.0919 +/- 0.0202, $R^2=0.995$, FWHM = 672.2 MHz, Extracted Temperature=828 K

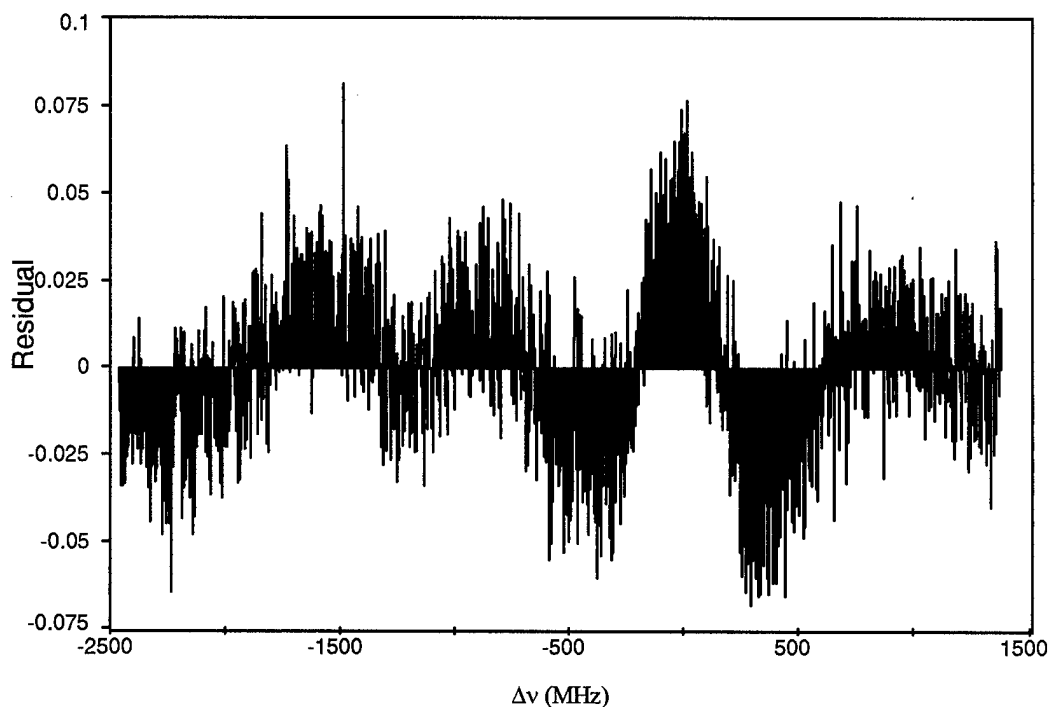


Figure C-19. P(53) 19-2 residual trend for the 1" Doppler-limited fit.

VITA

James Ward Myers, Jr. was born on 11 November, 1972 in Los Angeles, California. He graduated in 1990 as salutatorian of his senior class at Liberty Hill High School in Liberty Hill, Texas. He attended New Mexico Military Institute during the 1990-91 school year in preparation for the United States Air Force Academy under a Falcon Foundation Scholarship. In 1991 he was accepted to the Academy, and graduated with a Bachelor of Science degree in Physics and a regular commission as a Second Lieutenant in the Air Force in 1995.

His first duty station was at Phillips Laboratory (now Air Force Research Laboratory, Phillips Site) at Kirtland Air Force Base, New Mexico. For one year he worked in the Plasma Physics lab as a pulse power experimentalist. The next two years he worked as a Deputy Program Manager in the Directed Energy Directorate in the High Power Microwave division. While there he assisted the transition of mission-critical HPM technologies to Air Force user commands and participated in several high priority field demonstrations.

In 1998 he applied to the Air Force Institute of Technology (AFIT), at Wright-Patterson Air Force Base, Ohio, and was accepted to continue his education in the field of Physics. He completed all the necessary coursework and thesis to fulfill the requirements for a Master of Science Degree. His next duty station will be at Wright Patterson, in the AFRL Sensors directorate.